Needs, Trends, and Advances in Scintillators for Radiographic Imaging and Tomography

Zhehui Wang, *Senior Member, IEEE*, Christophe Dujardin, Matthew S. Freeman, Amanda E. Gehring, James F. Hunter, Paul Lecoq, *Fellow, IEEE*, Wei Liu, *Member, IEEE*, Charles L. Melcher, *Life Fellow, IEEE*, C. L. Morris, *Member, IEEE*, Martin Nikl, Ghanshyam Pilania, Reeju Pokharel, Daniel G. Robertson, Daniel J. Rutstrom, *Graduate Student Member, IEEE*, Sky K. Sjue, Anton S. Tremsin, S. A. Watson, Brenden W. Wiggins, Nicola M. Winch, and Mariya Zhuravleva, *Member, IEEE*

***Abstract*— Radiographic imaging and tomography (RadIT), which started with Röntgen's seminal X-ray work in 1895, now includes an increasing number of IT modalities. In addition to the original absorption-based X-ray radiography, others include phase contrast X-ray imaging, coherent X-ray diffractive imaging, MeV X- and γ-ray radiography, X-ray computed tomography, proton IT, neutron IT, positron emission tomography (PET), high-energy electron radiography, and cosmic-ray muon tomography. Scintillators are widely used in RadIT as the detector frontend that converts ionizing radiation into signals and data. We give an overview of the status and needs of scintillator applications in RadIT. More than 160 kinds of scintillators were presented during the SCINT22 conference and offered ample options for novel RadIT applications. New trends in scintillators for RadIT applications include inorganic and organic scintillator composites or heterostructures, liquid-phase synthesized perovskites and single-crystal micrometer-thick films, use of multiphysics models and data science to guide scintillator and RadIT optimization, structural innovations, such as photonic crystals, nanoscintillators enhanced by the Purcell effect, heterostructural scintillating fibers, and multilayer configurations. RadIT has also been recognized as a powerful tool for scintillator discovery and development.**

***Index Terms*— Data-driven discovery, dose, fast timing, high energy physics (HEP), inorganic scintillator, ionizing radiation, multimodal imaging, nanomaterial, photodetectors, photonic crystal (PhC), Purcell effect, radiographic imaging, radiographic tomography, radiography, scintillation, structured scintillators.**

Manuscript received 19 June 2023; revised 26 June 2023; accepted 27 June 2023. Date of publication 28 June 2023; date of current version 18 July 2023. This work was supported in part by the U.S. Department of Energy (Los Alamos Report Number LA-UR-22-32994) under Contract 89233218CNA000001. The work of Ghanshyam Pilania was supported by the Laboratory Directed Research and Development (LDRD) Program, Los Alamos National Laboratory, under Award 20190043DR. The work of Reeju Pokharel was supported by the Dynamic Materials Properties Campaign, Department of Energy National Nuclear Security Administration, under Grant DOE-NNSA. The work of Daniel J. Rutstrom was supported in part by the DOE-NNSA through the Nuclear Science and Security Consortium under Award DE-NA-0003 180 and Award DE-NA-0003996 and in part by the DOE, Office of Nuclear Energy, Integrated University Program Graduate Fellowship. The work of C. L. Morris and Mariya Zhuravleva was supported by the DOE-NNSA through the Nuclear Science and Security Consortium, University of Tennessee, under Award DE-NA-0003 180 and Award DE-NA-0003996. The work of Anton S. Tremsin was supported in part by the U.S. Department of Energy/NNSA/DNN Research and Development and in part by the Lawrence Berkeley National Laboratory under Contract AC02-05CH11231. An earlier version of this paper was presented in part at the special issue for the 16th International Conference on Scintillating Materials & Their Applications (SCINT22), September 19–23, 2022, Santa Fe, NM, USA [DOI: 10.48550/arXiv.2212.10322]. *(Corresponding author: Zhehui Wang.)*

Zhehui Wang, Matthew S. Freeman, Amanda E. Gehring, James F. Hunter, C. L. Morris, Ghanshyam Pilania, Reeju Pokharel, Sky K. Sjue, S. A. Watson, Brenden W. Wiggins, and Nicola M. Winch are with the Los Alamos National Laboratory, Los Alamos, NM 87545 USA (e-mail: zwang@lanl.gov; msf@lanl.gov; gehring@lanl.gov; jhunter@lanl.gov; cmorris@lanl.gov; gpilania@lanl.gov; reeju@lanl.gov; sjue@lanl.gov; scottw@lanl.gov; bww@lanl.gov; nwinch@lanl.gov).

Christophe Dujardin is with the Institut Lumière Matière, UMR5306, CNRS, Université Claude Bernard Lyon1, 69622 Villeurbanne, France (e-mail: christophe.dujardin@univ-lyon1.fr).

Paul Lecoq is with the European Organization for Nuclear Research, CH-1211 Geneva, Switzerland (e-mail: paul.lecoq@cern.ch).

Wei Liu and Daniel G. Robertson are with Mayo Clinic, Phoenix, AZ 85054 USA (e-mail: liu.wei@mayo.edu; robertson.daniel@mayo.edu).

Charles L. Melcher, Daniel J. Rutstrom, and Mariya Zhuravleva are with the Department of Materials Science and Engineering, University of Tennessee, Knoxville, TN 37996 USA (e-mail: cmelcher@utk.edu; drutstro@vols.utk.edu; mzhuravl@utk.edu).

Martin Nikl is with the Institute of Physics, Czech Academy of Sciences, 16200 Prague, Czech Republic (e-mail: nikl@fzu.cz).

Anton S. Tremsin is with the Space Sciences Laboratory, University of California at Berkeley, Berkeley, CA 94720 USA (e-mail: astr@berkeley.edu).

Color versions of one or more figures in this article are available at https://doi.org/10.1109/TNS.2023.3290826.

Digital Object Identifier 10.1109/TNS.2023.3290826

I. Introduction

SCINTILLATORS are important materials for radiographic imaging and tomography (RadIT) when ionizing radiations, such as X-rays, energetic charged particles (e.g., electrons, positrons, protons, and α-[^{4}He] particles), neutrons, and others are used to penetrate through optically opaque objects to reveal their internal material structures. RadIT started with Röntgen's discovery of X-rays and the invention of X-ray radiography in 1895 [1], which predated the discoveries of electrons and atomic nuclei as the elementary building blocks of matter. By the 1930s, quantum mechanical interpretation of atomic structures and fundamental forces paved the way toward understanding material properties, such as crystal or periodic lattice structures, polycrystalline structures, high-entropy materials, defects, and phase transition [2], and also provided the theoretical framework to interpret X-ray radiographs resulting from X-ray interactions with the electronic structures of materials. Nuclear interactions with X-rays, except for X-ray energies above 1 MeV, are usually ignored.

Since their initial use by Röntgen, Crookes, and other pioneers, there is now an enormous number of scintillators to choose from for X-ray detection, RadIT, and other

applications. It is no exaggeration to say that a scintillator can be found in each phase and form of matter. More than 160 kinds of scintillators and their applications were reported in the 16th International Conference on Scintillating Materials & Their Applications, Santa Fe, NM, USA, September 19–23, 2022 (SCINT22) Conference. It is clear from Table III that the majority of the scintillators are inorganic chemicals. The SCINT conference series, which dates back to 1992, has accordingly addressed inorganic scintillator science and technology predominantly [3]. Some additional reviews on scintillators relevant to ionizing radiation detection, high energy physics (HEP), and medical imaging can be found, for example, in [4], [5], [6], [7], and [8].

One may find scintillators in all four common phases of matter: solid scintillators, liquid scintillators, gas scintillators, and plasma scintillators [9]. Standalone, chemically stable, and solid-state scintillators are by far the most convenient to use. Scintillators have also been classified according to their elemental composition, namely organic scintillators, inorganic scintillators, oxides, garnets, halids, rare-earth scintillators, and so on. In addition to doped halides, such as NaI:Tl, CsI:Tl, rare-earth inorganic scintillators, such as cerium-doped lutetium–yttrium oxyorthosilicate (LYSO), and garnets, such as cerium-doped lutetium aluminum garnet (LuAG), are among the popular scintillator choices in X-ray and RadIT applications today. New formulations of rare-earth doping of inorganic scintillators using europium (Eu), praseodymium (Pr), ytterbium (Yb), and others remain an exciting discovery frontier for faster scintillation decay time, minimal afterglow, higher light yield (LY) in the desired wavelengths, more flexible emission wavelength tuning, and other performance improvements.

Scintillators may still be classified according to their material structures, such as single-crystal scintillators, polycrystal scintillators, perovskite scintillators, glass scintillators, ceramic scintillators, plastic scintillators, heterostructured or composite scintillators, nanoscintillators, and so on. In addition to new scintillator discoveries, a new trend is to combine existing organic and inorganic scintillators in the same system, driven by "higher information yield" from a radiation field, such as particle identification (e.g., neutron/γ-ray discrimination), higher energy resolution, finer spatial resolution in imaging and particle tracking, picosecond (ps) time and/or timing resolution in time-of-flight (TOF), up to 4π detection solid angle, larger detection volume, and lower cost. With the emergence of liquid- or solution-based synthesis of scintillators, and additive manufacturing (AM) technology, scintillators may also be classified according to their synthesis and manufacturing methods. Liquid-phase synthesis of perovskites has enjoyed phenomenal success in recent years [10]. For example, lead-free low-dimensional perovskite-like metal halides, such as ternary copper (I) halides, were found to have very high photoluminescence yields, ~90 k photons/MeV (kph/MeV), and large Stokes shift, in addition to their photophysical properties and stability [11]. $CsPbBr_3$ reported an LY of 50 kph/MeV and 1-ns decay time at 7 K [12]. AM technology for scintillator fabrication remains in its infancy. Advances are still needed to 3-D print some of the most common polymer bases, such as polystyrene and polyvinyltoluene (PVT).

Scintillator LY and X-ray stopping power (or X-ray attenuation mean free path equivalently) are the first two material properties to be considered when selecting a scintillator for X-ray detection, including X-ray IT. LY is a measure of the number of optical photons per unit of X-ray energy (1 MeV or 1 keV, for example) deposited in the scintillator. Stopping power is a measure of scintillator thickness for effective attenuation of X-rays. Both the LY and stopping power affect the X-ray detection efficiency. Meanwhile, the growing adoption of and continuous advances in X-ray radiography technology and its variants, such as X-ray microscopy, X-ray phase contrast imaging (PCI), X-ray diffractive imaging, X-ray tomography, X-ray ptychography, motivated new scintillator discoveries and development [13], [14], [15], [16], [17], [18], [19]. In Section II, we expand upon the discussion of different aspects of X-ray IT, such as spatial and temporal resolutions, that require consideration of other scintillator properties besides LY and attenuation length.

An overview of scintillator applications in RadIT is given in Section III. Besides X-rays, particle IT, such as proton IT, neutron IT, electron IT, and positron emission tomography (PET), have also been invented, which have not only greatly enriched the field of RadIT but also motivated scintillator development and new scintillator properties due to the different particle interaction physics. Some highlights of the recent scintillator development are given in Section IV.

Scintillator-based RadIT modalities are also closely correlated with advances in modern light and particle sources, such as particle accelerators [20], [21], detector technologies, especially, 2-D photodetectors and more recently data science [22]. Besides topics, such as scintillators for space applications, scintillator development, and discovery, are poised to enter a new phase through big data mining, multiphysics models, new experimental information derived from automated, high throughput, and in situ RadIT, including multimodal RadIT, as discussed in Section III-J. It is clear that the interdisciplinary marriage between scintillator science and technology and RadIT offers many exciting opportunities for innovation in the coming decade, as summarized at the end in Section V.

II. RadIT and Scintillator Metrics

The most common setup of X-ray radiography has essentially remained the same as in Röntgen's original work [1], as illustrated in Fig. 1, which consists of an X-ray source, the object to be radiographed, and a detector that captures the 2-D projection of the object. Scintillators, together with the optics and optical array detectors, such as a CCD camera, are often used for radiography using high-energy X-rays. X-ray image size may be estimated with geometric or ray optics. The magnification, for example, is given by $(z_1 + z_2)/z_2$ for a point source, where z_1 is the distance between the point source and the object, z_2 the distance between the object and the detector. Image blurs usually occur due to the finite source size, X-ray scattering, finite scintillator thickness, optical blur, and finite detector pixel size.

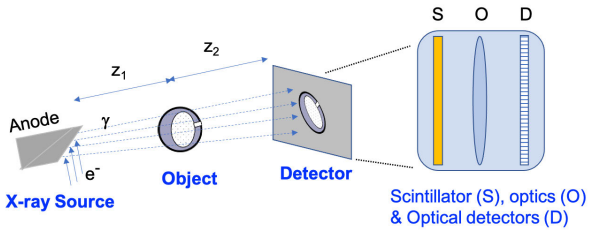

Fig. 1. Basic setup of X-ray radiography consists of an X-ray source, the object, and a detector.

In X-ray radiography, X-ray attenuation is commonly used to generate images and contrast in objects. The transmitted X-ray intensity through an object (I) that reaches a scintillator is attenuated from the source intensity (I_0) by the line integrated density or areal density, see [23]

$$I = I_0 \exp\left(-\sum_i \int_0^L dl \rho w_i \sigma_i / A_i M_0\right). \tag{1}$$

Here, the object thickness that the X-ray traverses is L. The object is a material compound of multiple elements represented by i. ρ is the mass density of the compound. $w_i = g_i A_i / \sum_j g_j A_j$ is the fraction by weight of the ith atom in the compound molecule. g_i is the number of ith atoms in the compound molecule. A_i is the corresponding atomic mass number. M_0 is the atomic mass unit. σ_i the total X-ray attenuation cross section corresponds to the ith element. $\sigma_i / A_i M_0 \equiv \mu_i$ is also called the mass attenuation coefficient, which varies with the type of element in the periodic table but does not depend on the density. The integral formula (1) is also applicable to materials with a mixture of compounds or position-dependent mass density $\rho = \rho(l)$, which we shall not elaborate further for algebraic simplicity. For materials with a uniform density ρ, (1) reduces to $I = I_0 \exp(-\sum_i L \rho w_i \sigma_i / A_i M_0)$.

Neglecting smaller probability events, such as photonuclear processes, the total X-ray attenuation cross section in most IT settings can be approximated by a sum of four cross sections

$$\sigma_i = \sigma_i^{pe} + \sigma_i^{\text{coh}} + \sigma_i^{\text{inc}} + \sigma_i^{\text{pair}}. \tag{2}$$

Here, σ_i^{pe}, σ_i^{coh}, σ_i^{inc}, and σ_i^{pair} are photoelectric (PE) absorption, coherent or Rayleigh scattering, incoherent or Compton scattering, and electron–positron pair production cross section, respectively. For each element Z_i in the periodic table, the PE cross section dominates at low X-ray energies up to a threshold ($\lesssim$0.1 MeV, lower thresholds for low-Z atoms, such as hydrogen and carbon), $\sigma_i^{pe} \propto (1/A_i)(Z_i^{\alpha}/E^{\beta}) \propto (Z_i^{\alpha-1}/E^{\beta})$, with $\alpha \sim$ 4–6 and $\beta \sim$ 3–3.5 [2], [24]. The X-ray PE attenuation cross section is a strong function of the atomic number Z_i and decreases rapidly with increasing X-ray energy (E). Above ~0.1 MeV and depending on Z_i, the incoherent scattering cross section becomes dominant until the electron–positron pair production becomes important. The pair production threshold is at twice the electron mass-energy $2m_e c^2 = 1.022$ MeV. The pair-production becomes significant only above ~3 MeV and depends on Z_i linearly [25].

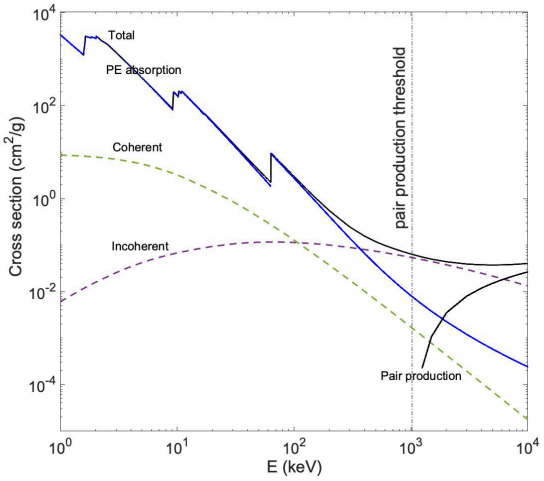

Fig. 2. Energy-dependent X-ray cross sections in LYSO with an atomic number ratio of Lu:Y:Si:O = $2(1-x)$:$2x$:1:5 and $x = 0.075$. The total cross section is a sum of PE absorption, coherent scattering, incoherent scattering, and electron–positron pair production. The data are from the NIST/XCOM database.

In short, X-rays primarily interact with the electrons in materials except for energies above a few megaelectron volt, see Fig. 2 for an example of energy-dependent X-ray cross sections in LYSO. The total X-ray attenuation cross section is a sum of PE absorption, coherent scattering, incoherent scattering, and electron–positron pair production.

The above-mentioned ray-tracing or "particle" model for X-ray attenuation in the matter, (1), are complicated by wave' properties of X-rays, such as refraction and diffraction [26]. Coherent scattering leads to X-ray diffraction and tends to redistribute the X-ray flux and intensities in the forward and backward direction with respect to the X-ray beam propagation. Incoherent scattering spreads X-rays into the 4π solid angle according to the well-known Klein–Nishina formula. Diffraction and scattering, therefore, can complicate the interpretation of absorption-based X-ray radiography through reduced image contrast [27]. Another limitation in absorption-based X-ray IT methods is the low contrast for low-Z materials, such as biological objects, when X-rays with energies above 20 keV are used [14].

Meanwhile, X-ray diffraction and interference can also be used for X-ray imaging when a sufficiently high-intensity monochromatic X-ray source, such as the third-generation synchrotrons, is available [13], [16]. While the modern X-ray tubes using rotating anodes can deliver 10^5 times the X-ray flux available to Röntgen, the third-generation synchrotron X-ray sources can deliver 10^{18} times the X-ray flux and keep improving. The high X-ray fluxes and associated X-ray doses are now causing significant scintillator heating and potentially reducing the lifetime of the scintillator due to radiation damage. X-ray PCI has seen great success using synchrotrons, see Fig. 3. Hard X-ray PCI is also effective for low-Z materials, in part due to the fact that X-ray phase shift cross section can be a thousand times larger than the X-ray absorption cross section for light elements, such as hydrogen, carbon, nitrogen, and oxygen [15]. In X-ray PCI, the distance between the object and detector satisfies $z \sim a^2/\lambda$ [13], which corresponds to a distance $z \sim 2$ m for an object resolution $a \sim 10$ μm at the

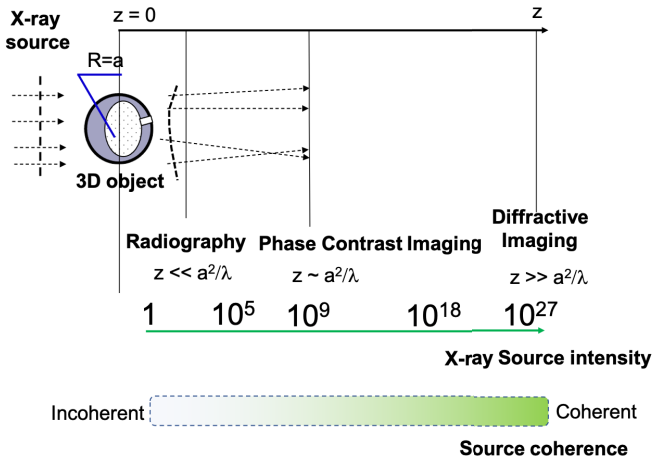

Fig. 3. Several lensless X-ray radiography and imaging modalities, depending on the X-ray source properties (coherent and incoherent), X-ray interactions (absorption, scattering) with the object, postinteraction X-ray propagation (interference and diffraction), and the X-ray detector distance to the object.

X-ray energy of 25 keV ($\lambda = 0.0496$ nm). Dynamic X-ray PCI, or movies of X-ray PCI images, are also possible due to the repetitive X-ray pulses at 10 s of nanosecond intervals. X-ray free electron lasers (XFELs) are currently the most intense, coherent laboratory X-ray sources for coherent imaging and related applications [21]. X-ray coherent diffractive imaging [19], X-ray Bragg projection ptychography [18] from XFELs are used to image nonperiodic material structures and lattice dynamics with nanometer-resolution. X-ray computed tomography (CT), introduced as a method to reconstruct 3-D models from 2-D radiographs of many different angles, was introduced in the 1970s. X-ray diffraction CT was introduced based on the coherent scattering [28]. In addition to continuous improvements in resolution, another trend in X-ray IT is to improve temporal resolution and reduce the number of 2-D projections toward time-resolved CT.

It should be mentioned that table-top microfocus X-ray sources with a spot size less than 100 μm, which have high spatial coherence at the object location but are not necessarily monochromatic in energies, have also been successfully used for X-ray PCI [14]. This is made possible in part by the use of high-performance detectors, including the use of scintillators in conjunction with high-resolution pixelated cameras [29]. Further advances in X-ray IT critically depend on advances in scintillators LY and other metrics, which we elaborate on in Section II-A.

A. RadIT Metrics

1) Spatial Resolution: Spatial resolution measures the ability to differentiate *the smallest* spatial variations in density and other physical quantities, such as the temperature, velocity, lattice structure, or phase, of an object [30]. Similar to optical imaging, a point-spread function (PSF) can be used to describe the finite resolution or the image blur in X-ray IT and RadIT. A PSF may be interpreted mathematically as a 2-D (in imaging) or 3-D (in tomography) intensity distribution as the result of the blurring of a pointed intensity, which is described by a 2-D or 3-D Dirac delta function [31]. PSF is most useful for the analysis of a linear information system like an image, which may be treated mathematically as a linear superposition of intensities, or the convolution of PSF with the unblurred image.

Image blur occurs due to a number of reasons: the finite X-ray source size or equivalent in particle-based IT, dispersion of the optics or propagation in lensless imaging, diffraction, and scattering of the X-rays by the object and the scintillator, motion of the object in a dynamic experiment such as material compression and deformation due to implosion, vibration of the scintillator and the instrument, and different mechanisms of instrumentation broadening, such as the isotropic emission of scintillating light in a bulk scintillator or the charge sharing among neighboring pixels, in CCD or CMOS cameras. Assuming that each source of blurring is a mutually independent Gaussian process, the overall resolution (δ) may be estimated as a sum of blurring widths (δ_k)

$$\delta = \sqrt{\sum\nolimits_k \delta_k^2} \tag{3}$$

for each of the blurring mechanisms k. Micrometer spatial resolution has now been routinely obtained for small ($\sim$1 mm^3) objects by using synchrotrons and scintillator cameras [32]. The resolution also depends on the object size, the wavelength of the X-ray, or the energy of the particle in a particle IT, such as neutron or proton radiography, and the magnification. Submicrometer resolution down to atomic dimension is possible in X-ray microscopy, coherent diffractive imaging for small objects less than 10^6 μm^3 in volume. In medical and industrial X-ray CT, nondestructive IT of thicker objects ($>10^3$ cm^3 in volume) is achieved with a compromised resolution at $\delta > 100$ μm.

A comparative summary of the spatial resolution (δ), or voxel resolution in tomography for different forms of RadIT is given in Fig. 4. A previous consideration was given to single-photon emission CT (SPECT) [33]. Depending on the interaction cross sections, the radiation dose $\mathcal{D}$ scales with the spatial resolution δ as $\mathcal{D} \propto 1/\delta^k$. For X-ray radiation-damage-limited dose, k was found to be 4 [34]. A similar consideration may be used for protons, neutrons, muons, and others. The X-ray dose has to increase by a factor of 10^4 to maintain a constant signal-to-noise ratio (SNR) for a factor of 10 improvements in resolution; for example, imaging at 50-μm resolution requires 10^4 higher dose than at 500-μm resolution [35]. Therefore, the dose constraint poses a significant limitation to the achievable spatial resolution in practice in X-ray IT, especially in in vivo and in situ medical IT. For neutron, proton, and muon IT, as well as time-resolved X-ray IT, the spatial resolution is typically limited by the radiation source intensity.

Scintillators become a significant contributor to image blur and PSF in high-energy photon IT and neutron IT. In MeV photon radiography, tens of millimeter thick scintillator, such as LSO:Ce, are needed for efficient detection of the high-energy photons. In fast neutron imaging, millimeter and thicker scintillators are also needed. Modulation transfer functions (MTF) is a frequency space representation or Fourier transform of the line spread function (LSF). LSF is related to a 2-D PSF through an integration that reduces the dimension by one [31].

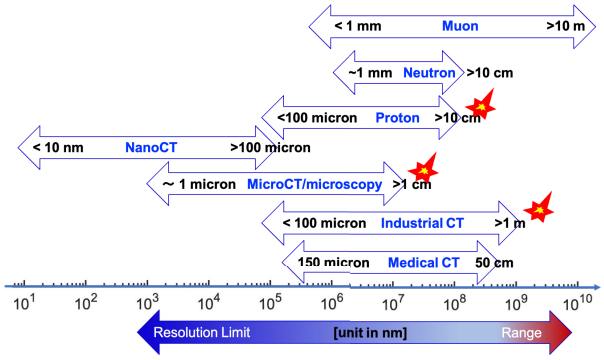

Fig. 4. Comparison of spatial resolution and range (of the interrogating radiation in the target) or the size of the field-of-view (FOV) for different RadIT modalities. ✸ symbolizes flash or single-pulse (or a very few pulses) time-resolved radiographic capabilities.

Due to the complex interplay among different mechanisms for PSF, Monte Carlo (MC) simulations are often used for image analysis, including PSF, LSF, and MTF [31], [36], [37]. Some factors, such as visible light transport in scintillators and electronics in digital cameras, which are usually ignored in the MC calculations, require experimental data inputs due to the lack of accurate models.

Several methods are used to improve the spatial resolution when thick scintillators are used. Traditionally, columnar scintillators and segmented scintillators are used to confine the optical emissions along the direction of X-ray and particle beams [38]. Alternatively, the multilayer thin-scintillator configuration is also useful to improve the efficiency without compromising the spatial resolution by minimizing the optical photon pathlength before reaching the photodetectors [39]. Some recent work on using micrometer-thick scintillators is summarized in Section IV-C. More recently, photonic crystal (PhC) scintillators or structured scintillators, with features comparable to and less than optical wavelengths are showing promising results to guide optical emissions to the detectors with minimal loss and spatial spread [40].

2) Field of View: Centimeters and larger objects are frequently encountered in RadIT, which require commensurately large FoV and depth of field. As shown in Fig. 4, medical CTs are designed for a human body (>1 cm). Industrial CTs are used for quick (seconds to minutes on many occasions) and noninvasive inspection of cargo containers (>1 m) [41], airport security (>1 cm), nondestructive testing in the industry (>1 cm), and lately AM (>1 cm). Cosmic-ray muon tomography was used to look for hidden chambers in a pyramid (>10 m) [42] and has recently been used to inspect damaged nuclear reactors (>1 m) [43].

There are a number of practical limitations to cover the full FoV, which ideally should intercept all the detectable signals in the 4π solid angle. Compton scattering of X-rays, nuclear scattering of neutrons, and multiple-Coulomb scattering of charged particle beams can spread the primary ionizing beams and secondary particles into the 4π solid angle. For a 100 × 100 cm FoV, a spatial resolution of $\delta = 1$ mm would require a pixelated detector with $N_p = 10^6$ pixels (N_p symbolizes the number of pixels of a pixelated sensor, such as a CMOS or CCD camera). To resolve the PSF with smaller pixels, for example, a factor of 3 decrease in pixel size would increase the number of pixels by a factor of 9. The spatial dynamic range, which is equivalent to $(N_p)^{1/2}$, is traditionally limited by the availability of large-format imaging sensors and image sensor cost. Recent advances in CMOS sensors at lower cost provide opportunities for billion-pixel and large format RadIT camera designs [44]. Monolithic inorganic scintillators of 1 m in size are rare due to, for example, the crystal growth cost. Segmented scintillators (see Section III-B) and tiled scintillators (see Section III-D) are, therefore, often used for large FoV. Due to the refractive index mismatch, scintillator light spread at the tile boundaries can lead to undesirable artifacts.

3) Time or Temporal Resolution: Röntgen's first X-ray radiograph was static, but nature is fundamentally dynamic and in perpetual motion according to Heisenberg's uncertainty principle. Time-resolved RadIT methods have been increasingly used to examine the changes or dynamics of materials since Röntgen's pioneer work. In high-speed imaging, such as GHz X-ray imaging [45], [46], it is known empirically that the time or temporal resolution (δ_τ) is correlated with the spatial resolution (δ) as $\delta/\delta_\tau \sim 1-100$ km/s [47], limited by the achievable speed of motion in the laboratory. To image the motion requires a sufficient number of X-rays and other particles (10^7 or greater per Mpixel image for low noise detectors, see the discussions in Section II-A4) for at least two images separated by δ_τ, which usually require a sufficiently bright source of X-rays or particles, and an efficient scintillator converter and photodetector. When a scintillator is used, the scintillator decay time needs to be a fraction (~1/3) of δ_τ for consecutive frames of images, which results in a scintillator light decay by a factor of e^{-3}, sufficient to avoid significant image latency from one image frame to the next as in high-speed synchrotron X-ray imaging [48].

4) Feature Detectability and Noise: One of the central questions in RadIT, similar to other forms of IT, such as optical IT, ultrasound IT, MRI, and so on, is what tiny features may be resolved in the ubiquitous presence of noise. This is sometimes known as the *detectability problem*. A theoretical framework for feature identification in a noisy environment, which is intrinsically statistical, now exists, following the pioneering work of Rose et al. [31], [49]. Many useful concepts, such as contrast, contrast transfer function, contrast threshold [50], noise-equivalent power, contrast-to-noise ratio, SNR, and so on, are applicable to normal vision, as well as RadIT. For example, contrast (C) is intuitively defined as the difference between observed intensity for feature A (I_A) and a reference feature B (I_B), $C = 2|I_A - I_B|/(I_A + I_B)$. In the absence of reference feature intensity, a "dark field" (with illumination, such as the X-ray source off) and a "white field" (with illumination on but without the object) may be taken as references for images with an object of interest. In another example, detective quantum efficiency (DQE) as a function of spatial frequency (f, in lp/mm) may be defined as

$$\mathrm{DQE}(f) = \frac{\mathrm{SNR}_{\mathrm{out}}(f)}{\mathrm{SNR}_{\mathrm{in}}(f)} \propto \frac{\mathrm{MTF}(f)^2}{\mathrm{NPS}(f)} \tag{4}$$

where the input SNR, $\mathrm{SNR}_{\mathrm{in}}(f) = (\Phi_i)^{1/2}$, is for an incident Poisson distributed flux Φ_i (per mm^2), and $\mathrm{SNR}_{\mathrm{out}}(f)$ is the

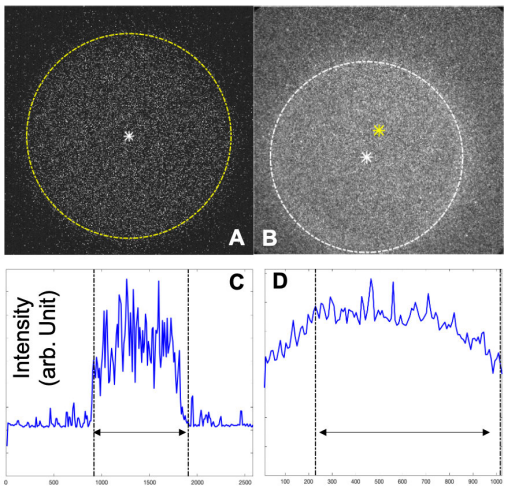

Fig. 5. Comparative study of X-ray (Ba K_α and K_β lines) source images with (B) and without (A) an LYSO scintillator. An image intensifier was used to enhance the sensitivity of scintillator detection in (B). (C) and (D) are the corresponding vertical lineouts of intensities through the centers of the two images above. The arrowed lines in (C) and (D) indicate the regions within the X-ray emission circles in (A) and (B).

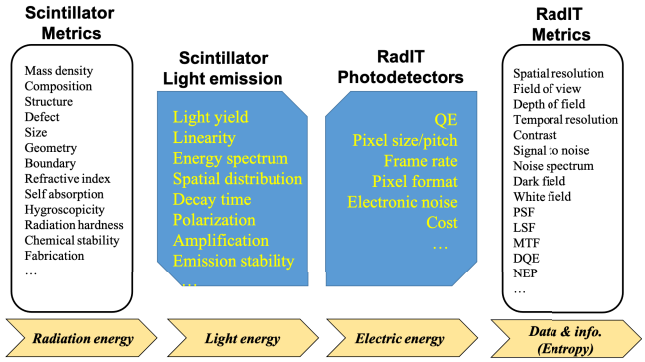

Fig. 6. RadIT metrics and scintillator metrics are correlated through the energy and data (information) flows. Material properties, such as density, composition, and so on, determine how the information encoded in radiation, such as X-rays, are converted to (visible) light emission, then electrical signals in photodetectors, before being recorded as data, such as images, which can be characterized by metrics, such as spatial resolution, FoV, DQE, and so on.

corresponding quantity in the image. DQE was introduced by A. Rose as a measure of "useful quantum efficiency" or noise-equivalent quantum efficiency of a detector [51]. Noise power spectrum (NPS) measures the noise of the imaging system as a function of spatial frequency. NPS can be estimated by, for example, using a method given in [52].

Contrast, feature detectability, and noise are detector and scintillator dependent. One of the oldest detectors with single-visible photon sensitivity is a photomultiplier tube. There is now a growing number of photodetector technologies with single-photon detection sensitivity and high quantum yield in the visible wavelength regime, such as silicon photomultiplier (SiPM), multipixel photon counter (MPPC), CCD cameras, and more recently CMOS pixelated sensor arrays or CMOS cameras [44], [53]. CCD and CMOS cameras ushered in the age of digital and real-time RadIT.

The use of low-cost and high-performance CMOS cameras is now growing in RadIT [44]. Low cost is in part due to the large quantities of CMOS sensors used in both scientific and consumer applications as in cell phones. High performance is a combination of small pixel pitch (<1 μm), high visible-light quantum yield ($>90\%$), low electronic noise (<1 e^-), and large FoV or format exceeding ten million pixels [44]. CMOS sensors are directly sensitive to X-rays, charged particles [54], and neutrons with a layer of neutron absorber, such as ^{10}B, deposited on the sensor surface [55]. An example of direct CMOS (model Vita 5000, see [44] for more information) detection of X-ray (K_α 32.06 and K_β 36.55 keV characteristic lines of barium), in comparison with the use of an LYSO (0.2-mm thick) converter, is shown in Fig. 5.

Fig. 5(A) and (B) both have two main features from the same X-ray source: the center of the X-ray source circle and the source edge. In Fig. 5(A) and (B), the raw data contrast are 0.93 and 0.34 out of the perfect contrast of 2. The relatively lower contrast in (B) also led to a large deviation in identifying the center of the X-ray source using the intensity centroid from the data, as shown in the colored star in Fig. 5(B) (the corrected one is the white star). SNR in Fig. 5(A) and (B) are 15 and 8, respectively.

B. Scintillator Metrics

The complex correlations between RadIT metrics and scintillator metrics are summarized in Fig. 6 through the energy and data (information) flows. In addition to LY, other metrics for radioluminescence may include the emission spectrum, spatial distribution of the light, decay time, polarization, amplification (in active scintillator medium, which is relatively rare for now), and emission stability or degradation due to radiation damage of scintillator. Light emission depends on a number of scintillator metrics, which include scintillator mass density, material composition, material structure, impurity and defects, scintillator size, scintillator geometry, scintillator boundary conditions, and scintillator responses, to the environment, such as temperature, moisture, coupling to the photodetectors, refractive index, and self-absorption. The light emission also depends on the type of radiation, as discussed in more detail in Section III for X-rays of different energies, neutrons, and charged particles.

Due to the complex interplay among different metrics and material properties, quantitative mappings between scintillator metrics and RadIT metrics usually require multiphysics codes as Geant4 [56], [57] and MC N-particle (MCNP) [58]. First-principles simulations of full RadIT systems are still beyond the current scope of Geant4 and MCNP due to the lack of sufficient accuracy for data interpretation and object reconstruction from images and tomographic measurements. In addition to improvements in RadIT system-specific modeling and simulations, laboratory experiments to characterize scintillators, and scintillator-photodetector prototypes (see Sections III and IV) remain essential in scintillator selection for RadIT applications and system optimization. Recently, data science and the use of RadIT, such as neutron imaging for in situ scintillator development and characterization are highlighted as examples of emerging topics in Section III-H. Table III in the Appendix lists metrics requirements for specific applications.

It is obviously impossible to meet all the scintillator requirements simultaneously in most applications. A tradeoff between different metrics is often necessary, as briefly summarized here.

1) Stopping Power: The stopping power or linear attenuation coefficient depends on density, material composition (effective atomic number), and cross sections. A thicker scintillator corresponds to high stopping power. However, the spatial resolution usually degrades due to a larger volume of scintillator light emission and increases in scattering and straggling. Therefore, a tradeoff between stopping power and resolution is often necessary.

2) Light Yield: LY can differ for the same X-ray, charged particle, and neutron energy deposited. For X-rays, there is an additional complication due to the different X-ray-electron interactions. All the X-ray energy transfers to an electron in the scintillator in PE absorption. No energy transfer happens in the coherent scattering by the scintillator. Only a fraction of X-ray energy is absorbed by the scintillator for an incoherent scattering event, and there can be multiple such scattering events, thereby complicating image interpretation. For the pair-production process, the positron may carry a fraction of energy to a different location before reabsorption through electron–positron annihilation, and the possible detection of 511-keV photons at points remote from the annihilation event.

Many scintillators emit a relatively broad spectrum of wavelengths, and therefore, LY is wavelength dependent. Other factors, such as self-absorption and refractive index matching, count as well. It is known empirically that many scintillator emissions have multiple decay time constants for different wavelengths. A tradeoff between LY and the decay time is often necessary.

3) Decay Time: The scintillator decay times are determined by the spontaneous emission rate at the luminescence centers, which is an intrinsic property of the scintillator. Luminescence efficiency can be compromised by quenching/ionization processes affecting the excited state of luminescence centers which affects also its timing characteristics [59]. Furthermore, since the spontaneous emission in a bulk material is isotropic, some of the emitted photons may not reach the photodetector due to, for example, internal reflection at the boundary of the scintillator. PhC structures have been proposed or recently demonstrated to modify spontaneous emissions so that it is possible to obtain anisotropic emissions [60], higher efficiency of the scintillator light collection [61], as well as reduction of the intrinsic spontaneous emission rate, all in the visible range of wavelengths [62]. The last one is known as the Purcell effect, which was initially proposed for radio waves [63]. By locally enhancing the electric field, a higher emission rate may be obtained even if the probability of the electronic transition is weak [64].

4) Radiation Hardness (RH): RH is a passive characteristic. Radiation-induced charge carriers are relocated to material (point) defects and color centers arise, the absorption of which overlaps with the luminescence spectrum. Rising reabsorption decreases the externally measured LY. So-called radiation damage can be bleached, even spontaneously, by the release of charge carriers from traps so that the radiation-induced absorption shows distinct time and temperature dependence. RH of scintillators is an important consideration for RadIT as X-ray and particle sources continue to become brighter [8]. RH requirement can sometimes rule out scintillators with high LY or fast decay time. Furthermore, radiation-hardened scintillator materials can potentially activate when irradiated. This is especially important when imaging with neutrons, as activation of the scintillator materials can result in a persistent afterglow due to the decay products of the activation.

5) Size and Scalability: Large volumes of scintillators are needed in RadIT, e.g., for high-energy (MeV) X-/γ-ray and neutron detection. Large-size scintillators are needed to fully stop and capture high-energy particles/neutrons to measure the particle energy. A tradeoff between the scintillator size and the cost to buy or grow them and a tradeoff between the volume and fabrication time are often necessary.

6) Cost and Fabrication: Raw materials, fabrication processes, and crystal quality affect scintillator cost and availability. Some of the highest LY or fastest scintillators may require single-crystalline structures with minimal self-absorption, and fabrication cost is a key factor in scaling up some promising scintillators to the industrial scale. If they cannot be scaled up, a tradeoff between cost, LY, and decay time may be necessary for certain applications.

7) Stability and Ruggedness: Some scintillators are hygroscopic. Many organic liquids are degraded by dissolved oxygen and must be stored and operated under inert gas. There can be issues of scintillator dopants diffusing out or concentrating in the material due to for example mechanical and "thermal" shocks (sudden transition from indoor temperatures to outdoor temperatures). Low temperatures including cryogenic temperatures can reduce the thermal quenching of excited states in a scintillator, and therefore, increase the LY and reduce the radiative decay time for some fast scintillators. However, the use of cryogens can complicate the measurements. Therefore, a tradeoff between the operating scintillator environment and performance may be necessary.

III. Current Scintillator Applications in RadIT

While there is a growing number of semiconductor technologies, including high-Z semiconductors, such as GaAs and CdTe, CdZnTe (CZT) for X-ray IT [65], [66], [67], [68], scintillators, remain a favorite and sometimes the only option in RadIT applications, as summarized in Tables I and III in the Appendix.

Based upon the metrics discussed earlier, some advantages of scintillator-based detectors include but are not limited to a large number of scintillators and photodetectors to choose from, the flexibility in different combinations of scintillator with photodetectors, lower cost, and radiation hardness [69]. Some disadvantages of the scintillator detection scheme may include more complex data interpretation in order to model the scintillator light propagation with high fidelity, lower intrinsic spatial resolution due to the light propagation and spread, and edge effects due to the mismatch in refractive indices of different materials at the boundaries. There is no fundamental reason not to overcome these disadvantages, which motivate efforts

TABLE I
DIFFERENT RADIT MODALITIES, CONTRAST MECHANISMS, AND SCINTILLATOR CHOICES (EXAMPLES)

Modality	Contrast Mechanism	Scintillator
X-ray radiography[a]	Absorption	LuAG:Ce
MeV X-ray/γ-ray radiography	Incoherent scattering	BGO, L(Y)SO, GLO
X-ray PCI[a]	Coherent scattering, interference	LuAG:Ce
X-ray CT[a]	Absorption	
X-ray CDI[a]	Coherent scattering, interference	
proton radiography	Electron scattering, *or* Coulomb scattering	L(Y)SO
neutron radiography	elastic scattering	
relativistic electron radiography	electron scattering, *or* Coulomb scattering	CsI
PET[a]	e-e$^+$ annihilation	BGO, L(Y)SO
P2T [70]	e-e$^+$ annihilation	

[a] PCI: Phase Contrast Imaging. CT: Computed tomography. CDI: coherent diffractive imaging. PET: Positron emission tomography. P2T: Pair-production tomography.

in thin-film scintillators, nanostructured scintillators, meta-scintillators, PhC guiding of scintillator light, data science, and other exciting development, in this growingly interdisciplinary field.

A. X-rays Below 100 keV

Built upon the legacy of Röntgen and other pioneers, a large variety of X-ray sources ranging from compact microfocus sources to modern light sources, such as synchrotrons, and continually improving detectors, including scintillator-enabled ones, X-ray IT with photons below 100 keV is by far the most accessible form of RadIT. PE absorption dominates X-ray-matter interactions in this energy range. Depending on the materials with which X-rays interact, coherent, and incoherent scattering may not be negligible as the source intensity increases. To reduce the X-ray dose, contrast agents can be used to enhance the absorption contrast and allow not only structural imaging or static imaging but also functional imaging of in situ biochemistry and disease pathology [35]. Some of the most important developments for scintillators in this energy regime come from the growing number of synchrotron facilities around the world, e.g., the advanced photon source (APS), CHESS (hosted by Cornell University, Ithaca, NY, USA), diamond light source, The European Synchrotron Radiation Facility (ESRF), Grenoble, France, National Synchrotron Light Source II, Upton, NY, USA, PETRA III Max von Laue Experimental Hall, Hamburg, Germany, Shanghai Synchrotron Radiation Facility (SSRF), Shanghai, China, Super Photon ring-8 GeV, Sayo, Japan, and others, where the X-ray intensities are many orders of magnitude higher than the brightest table-topic X-ray sources, and the X-ray fluxes can be delivered at a repetition rate close to or above 10 MHz.

The bright synchrotron X-ray sources, together with sub-nanosecond short pulses, tunable wavelengths, and tunable bandwidths (from broadband "white beams" to monochromatic X-rays with less than 0.1% BW), allow different modalities of X-ray IT using scintillators, including the ones shown in Figs. 3 and 4. The high repetition rate of the synchrotrons allows time-resolved X-ray movies, with a sub-nanosecond temporal resolution dictated by the individual X-ray pulsewidth. By considering the stopping power, LY, decay time, and limiting scintillating light emission to the visible wavelengths (>400 nm), several commercial scintillators YAG:Ce, LuAG:Ce, and LYSO:Ce have been identified for time-resolved X-ray imaging at a repetition rate approaching 10 MHz [71]. These scintillators are widely used today in synchrotron facilities. A typical scintillator thickness is 100 μm to less than 1 mm, a tradeoff between energy-dependent X-ray detection efficiency and spatial resolution. Since a typical synchrotron beam diameter is only 1 mm or so, monolithic single crystals are readily available commercially for imaging and microtomography. For higher resolution, thin single-crystal films (SCFs), with a thickness in the range of 1–30 μm have been grown for high-resolution hard X-ray microimaging [72]. Monolayer and multilayer (with different dopants for each layer) thin films of LSO:Tb, LYSO:Ce were reported as alternates to YAG:Ce, LAG:Eu, and GGG:Eu for micrometer and sub-micrometer resolution. The search for brighter and heavier scintillator films, such as $CsPbX_3$ (X = Cl, Br, and I) is also ongoing [73]. Some additional discussions on SCF are given in Section IV-C.

In addition to multilayer thin films, one trend in scintillators that can potentially improve X-ray detection efficiency without sacrificing the resolution is structured scintillators. In one example, high aspect ratio pores were filled by melting of powered CsI (Tl) [74], a different approach from earlier work on CsI needles [75]. In another example, PhC cavities (1-D) were added to bulk scintillators BGO, $CdWO_4$, CsI:Tl, NaI:Tl, $(PEA)_2PbBr_4$, and YAG:Ce to tailor the emission spectrum for higher detection efficiency [76]. A broader "structure engineering" strategy was recently discussed in [77]. Practical structured scintillators that can meet the growing demand for synchrotron and other X-ray IT applications remain limited. In the following, we discuss some additional limitations and needs for scintillators.

Synchrotrons are now routinely used to examine polycrystalline nonperiodic structures, and to retrieve 3-D structural information through diffraction, extending X-ray crystallography pioneered by Laue, Bragg, and others. High-energy X-ray diffraction microscopy (HEDM) or 3-D X-ray diffraction microscopy (3DXRD) is such an implementation [78], [79], [80], [81]. Currently available sources and detectors lead to a spatial resolution of $\sim$1 μm and an orientation resolution of $<0.1^\circ$. With energies above 50 keV, sample cross section dimensions of $\sim$1 mm can be studied in materials containing elements across much of the periodic table. Using commercially available inorganic scintillators like doped LuAG, LY $\sim$20 ph/keV [82], 7% absorption efficiency, and a spatial resolution of around 2 μm was achieved by using a 20–30-μm-thick LuAG scintillator for the X-ray energy at 50 keV [83]. Fig. 7 shows an example of the 3-D microstructure of UO_2 characterized before and after heat-treatment using HEDM with 90-keV X-rays. It is only recently that such measurements have been possible [84]. However, the need for a long acquisition time to collect sufficiently high SNR

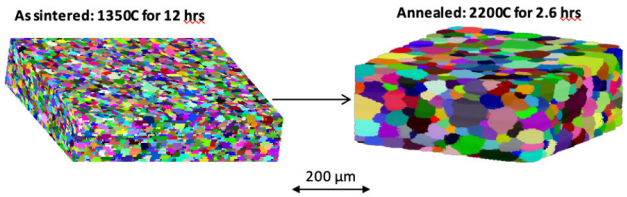

Fig. 7. Three-dimensional microstructure of UO_2 characterized before and after heat-treatment using HEDM.

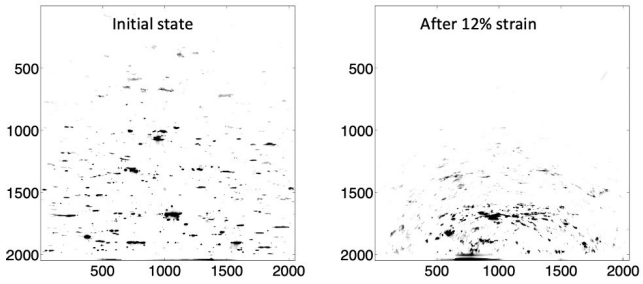

Fig. 8. Two-dimensional detector image showing diffraction from multiple grains satisfying the Bragg condition before and after 12% deformation of polycrystalline copper. Unit in 1.5 μm.

diffraction images prevented the collection of the kinetics information of grain growth.

To achieve submicrometer spatial resolutions in HEDM experiments, it is desirable to have thinner scintillators with higher LY, the theoretical limits of which are known for many materials [85]. A thinner scintillator improves spatial resolution but decreases detection efficiency and SNR, and vice versa. Moreover, the scintillator's LY is a critical factor in HEDM experiments, particularly when imaging high-Z materials at high energies (>80 keV) with high spatial resolution imaging (~1 μm or better) that require penetration of bulk specimens (e.g., >500 μm of uranium) [84].

The quality of diffraction signals deteriorates significantly when the crystallinity of an as-received sample starts to break due to defects and deformation. This results in diminished information extraction capabilities at large strains, severely limiting the effectiveness of HEDM [86]. Fig. 8 (LuAG scintillator) demonstrates the diffraction image recorded at the initial, recrystallized state, and after 12% tensile deformation of a polycrystalline copper specimen. The limitations imposed by large strain deformation on diffraction images are evident, including the loss of high-order scattering intensity and the streaking of diffraction spots. To address these challenges and enhance the quality of diffraction patterns for deformed specimens, it is crucial to develop and employ scintillators with higher LY and efficiency, enabling more accurate and detailed microstructural characterization.

As synchrotrons, such as APS-U, become brighter and deliver higher pulse rates, faster and brighter scintillators than L(Y)SO with no afterglow (image latency) will be needed. The marriage of several imaging and diffraction techniques together is another trend in synchrotrons. X-ray ptychography is a combination of conventional scanning transmission X-ray microscopy and coherent diffractive imaging (CDI) [87]. Integration of far-field HEDM with Bragg CDI was described recently [88], which requires single-X-ray photon counting together with a large dynamic range. Other emerging scintillator metrics in intense X-rays are also note worthy. In addition to heating and radiation damage due to higher X-ray doses, scintillator screens can become electrostatically charged due to X-ray ionization of the air, and ambient dust particles could be attracted to the scintillator screens [89]. Nonproportional response of $LaBr_3$ and $LaCl_3$:Ce to synchrotron X-rays in the range of 9–100 keV were reported [90], which could complicate data interpretation.

B. X-rays Above 100 keV

The large mean-free-path of X-ray photons above 100-keV energies makes them an effective nondestructive tool to radiograph thick and/or dense objects. Applications include weld inspection, parts inspection (including AM), portal monitoring, and hydrotesting.

The major limiting factors in high-energy radiography are the resolution loss due to Compton scattering in the detector and the low DQE of common scintillator–photodetector pairs. High detection efficiency for MeV photons is particularly important for flash radiography applications where fast data acquisitions are required to obtain high-fidelity images and the source flux is limited [91]. Quantum efficiency can be traded for: time in emergency response applications, patient dose in medical radiography, and the number of views in tomography. Therefore, maximizing the DQE is of paramount importance in these applications.

Some high-density crystals have been developed which are suitable for high-energy radiography and tomography, namely, bismuth germanate (BGO) [92], cerium doped lutetium oxyorthosilicate (LSO), and LYSO [93]. The properties of these scintillators are shown in Table II. LYSO and LSO suffer in some applications due to the intrinsic radioactivity of lutetium [94]. These single crystals cannot be grown in large sizes (>10 cm in diameter), and therefore, need to be pixelated or segmented for radiography purposes.

Segmented scintillators are composed of individual pixel light pipes, which produce a planar image suitable for fast optics [37], [38], [97]. The light pipe aspect is extremely important for multiple reasons. First, it allows low-f-number, planar optics to be used, and second, it eliminates veiling glare from inclusions, seams, and other defects in the scintillator. Using high-density material also reduces the spread of the Compton scattered photons thereby reducing the blur and improving the resolution. Additionally, when the pixels are optically isolated by means of a metal grid or similar the optical scatter is eliminated. Fig. 9 shows two segmented scintillators, a 40-cm-diameter LSO grid with 1 × 1 × 40 mm scintillator pixels [98] and a 10 × 20 cm BGO grid with 1 × 1 × 40 mm pixels. In both, the pixels are separated by a thin metal septum.

Recent developments in transparent sintered ceramics have produced a new bixbyite transparent ceramic scintillator, GLO [99], [100]. GLO has a very high density and high LY, but a relatively long decay time (properties shown in Table II). The largest scintillator fabricated thus far is roughly 30 × 30 cm in dimensions [101].

TABLE II

PROPERTIES OF SCINTILLATORS USED FOR HIGH ENERGY RADIOGRAPHY (DATA FROM [95] AND [96])

Scintillator	Formula	Density (g/cm^3)	LY (10^3 photons/MeV)	Decay time (ns)	Scintillator radioctivity
BGO	$Bi_4Ge_3O_{12}$	7.13	9	300	No
LSO	Lu_2SiO_5:Ce	7.4	26	40	Yes
LYSO	$Lu_{2(1-x)}Y_{2x}SiO_5$:Ce [a]	7.1	33	36	Yes
GLO	$Gd_{3y}Lu_{2(1-2y)}Eu_yO_3$ [b]	9.1	70	10^6 (1 ms)	Yes

[a] $x \sim 0.2$, [b] $y \sim 0.1$

Fig. 9. Segmented BGO and LSO [98] scintillators. Both have $1 \times 1 \times 40$ mm scintillator pixels and are separated by a metal septum.

Another technique available to take advantage of a large number of commercially available powdered or needle scintillators [of NaI, CsI, or Gadox (Gd_2O_2S)] is to use intensifying screens of high-Z metals [102], [103], [104], [105]. These screens convert energetic photons into Compton scattered electrons which are more readily captured by the scintillator. However, because of scintillator self-absorption, the quantum efficiency of these is still very low with a maximum of 1%. Intensifying screens and imaging plates can be stacked (at 1% per layer) with as many as 40 being demonstrated to obtain 20% DQE [106], as defined in (4). The downside is each plate must be read out individually and the radiographs aligned and averaged (suited more for storage phosphor imaging plates).

Fig. 10 shows an example of experimental DQE for various segmented scintillators [38]. These results demonstrated for the first time a 50% DQE system with a segmented BGO scintillator and a room-temperature camera. The glass fiber optic faceplate was shown to have a DQE of 30% and is a good compromise between the expensive segmented scintillators and commercial powdered or needle scintillators.

Fundamental scintillator research into high-density scintillators is ongoing, and breakthrough scintillators are always of interest. However, one of the key scintillator challenges for megaelectron volt photons is to find a way to manufacture existing scintillators into a myriad of forms, with reasonable cost, large format, and shorter timeline. Pixelated or segmented arrays with various thicknesses, dimensions, and even curvatures are examples of taking existing scintillators and modifying them for high-energy photon radiography and CT. Another possibility to explore is bonding pixels of BGO or LSO with an index-matching material to produce a large format scintillator.

C. Neutrons

Neutron IT as a nondestructive testing tool is relatively new when compared with X-ray IT. The International Society for

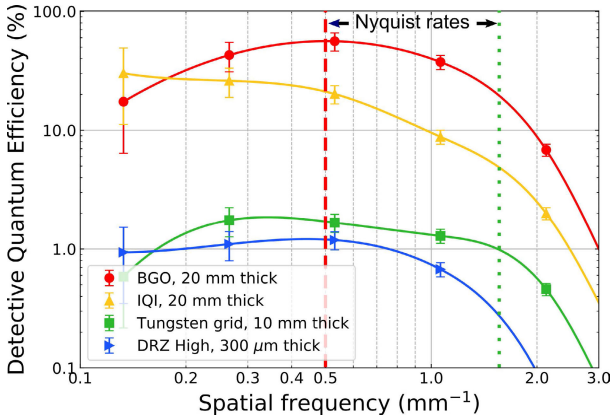

Fig. 10. Measured DQE for segmented BGO, image quality indicator (IQI) fiber optic glass plate, tungsten and glass pixelated array, and DRZ high (Gadox). The vertical dashed lines show the Nyquist rates for the segmented BGO scintillators. From [38] with permission.

Neutron Radiology (ISNR) was created in 1996 [107] to bring the neutron radiography and neutron imaging international communities together. Neutrons, mostly from nuclear fission reactors and spallation sources, have now been successfully used for in situ imaging and 3-D tomography of hydrogen fuel cells, diesel particulate filters, nuclear fuel rods, and fossils. Neutron IT has been extensively explored in the neutron energy range from subthermal to hundreds of megaelectron volt using the Los Alamos Neutron Science Center (LANSCE) 800-MeV accelerator, as summarized in a recent review [108]. The latest breakthroughs in laser-driven inertial confinement fusion may open up new avenues for neutron IT by providing a prompt (<1 ns) intense neutron source.

Neutrons complement X-rays as a unique material probe due to their strong nuclear interaction and relatively weaker interactions with electrons, e.g., through magnetic scattering [109]. The different transmission properties of neutrons and X-rays allow for better segmentation of materials when both of them are used simultaneously as in multimodal RadIT. The transmission of neutrons through a material obeys the same equation as (1) with the corresponding neutron cross sections. Similar to X-rays, neutron nuclear interaction cross section is a sum of absorption, coherent, and incoherent scattering in the nonrelativistic regime. On the other hand, neutron cross sections are highly isotope-sensitive, which makes neutrons more sensitive to ^{1}H than ^{2}H for image contrast, for example. The total ^{1}H thermal neutron scattering cross section is more than ten times that of ^{2}H. The thermal neutron absorption cross section of ^{6}Li is 940 barn, which is orders of magnitude lager than that of ^{7}Li, and makes ^{6}Li a popular element in

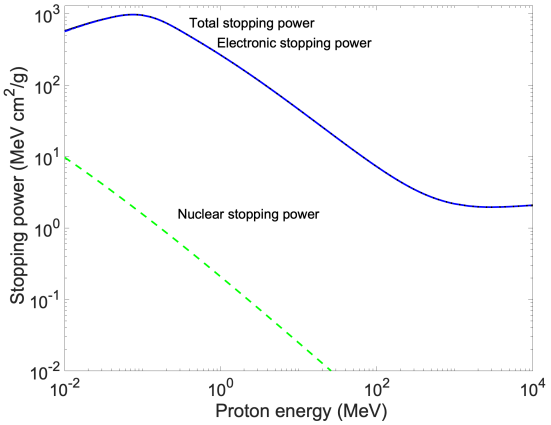

Fig. 11. Energy-dependent proton stopping power in a vinyltoluene ($C_{10}H_9$)-based plastic scintillator. The density is assumed to be 1.032 g/cm^3. The data are from the NIST/PSTAR database.

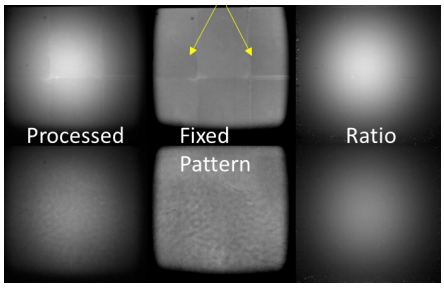

Fig. 12. Images of a proton beam made with the standard tiled monolithic LSO scintillator crystals (top row) and an LYSO granular screen (bottom row). The arrows point to the crystal scintillator tile boundaries. The fixed pattern noise from both detectors is observed to cancel in the ratio of a single image to a fixed pattern correction. However, the data from within ~1 mm of the tile boundary are not reliable.

scintillators for neutron detectors. While ^{6}Li-based scintillators are more sensitive to thermal neutrons, they are also, therefore, more susceptible to noise from energy down-scattered neutron background during fast neutron imaging compared with ^{7}Li-based scintillators, such as with CLYC-7.

Synergies between neutron scintillator detectors and X-ray scintillator detectors have been recognized [107]. An X-ray camera can turn into a neutron camera by switching the scintillators. From Table III in the Appendix, it is clear that in addition to neutron-specific scintillators that contain ^{6}Li, Gd (^{157}Gd and ^{155}Gd in particular), composite scintillators that combine materials with differential neutron sensitivities may also be considered. Further discussions on composite scintillators for fast neutrons are given in Section IV-D. Background reduction in neutron scintillators, especially, γ-ray background reduction, remains an important consideration and motivates new scintillator innovations.

D. Protons and Heavy Ions

Proton [110], [111] and heavy-ion beams, e.g., helium [112], carbon, and others [113], [114], have been used for RadIT since 1960s. Two primary contrast mechanisms of energetic proton and heavy ion IT are energy loss and multiple-Coulomb scattering [111], [115]. Fig. 11 gives an example of energy-dependent proton stopping power, calculated by using continuous slowing down approximation (CSDA), as a function of energy in a vinyltoluene-based [$CH_2CH(C_6H_4CH_3)$ or $C_{10}H_9$] plastic scintillator. Electronic energy loss is the dominant process in the energy range shown. Nuclear collisions and the corresponding energy loss may be neglected.

In addition to a lower dose, the proton and heavy ion IT have better material density resolution (~0.1%) than those of X-ray CT (~1%); however, higher cost and larger footprint have limited proton and heavy ion IT to existing proton and ion accelerator facilities. The energy ranges of such facilities are divided into three bands: low energy or <300 MeV per nucleon (mostly medical facilities for cancer therapy) [116], medium energy ~1 to a few gigaelectron volt per nucleon [117], [118], [119], and high energy >10 GeV per nucleon [120]. A magnetic lens allowed flash proton radiography of thick objects (up to 50 g cm^{-2}) with a time/spatial resolution below 200 ns/200 μm [121]. The spatial resolution was further enhanced by the implementation of a $\times$3 magnetic lens, that effectively shrinks the FoV for a higher spatial resolution to 65 μm [122].

For low-dose (time-integrated flux $<10^8$ particles) low-energy proton and ion IT, NE102 (equivalent to EJ-212) plastic scintillators (3.18 $\pm$ 0.05 mm thick) were used to measure the residual range of individual protons [123]. More recently, new detectors made of scintillator fibers coupled to SiPM arrays [124], and a phoswich detector made of $LaBr_3$(Ce) and $LaCl_3$(Ce) crystals [125] were developed for energy loss measurements.

Dynamic experiments require fast proton imaging at a higher dose rate. This was attained by focusing the light from a scintillator onto multiframe multiplexed CMOS cameras [117], [118]. The scintillator currently used is a 3 $\times$ 2 tiled array of 4 $\times$ 6 cm^2 monolithic LSO crystals 1.9-mm thick [117]. This system suffers from nonlinearities at the tile edges that produce artifacts in the images, and from the background due to totally internally reflected light that escapes due to defects in the crystals. The use of granular screens may address these problems. LYSO screens produce as much as six (black backing) or 12 (reflective backing) times more light per areal density thickness than the tiled crystal scintillator.

Fig. 12 shows 800-MeV-proton-induced images obtained using a tiled LSO scintillator along with a large grain (38–76 μm in size) LYSO screen. The center panel at the top shows clearly visible tile boundaries. Although the tile boundaries cancel when fixed pattern maps are used to correct the image, the data from within 1 mm of the boundary is not reliable because of reflections from the edge of the tile. The screen has a fixed pattern noise that cancels in the ratio.

For X-ray and charged particle radiography, DQE is determined in part by the brightness of the scintillator. However, for flash proton radiography, LYSO granular scintillator screens process sufficient light to give high DQE along with added benefits, which include high specific light output, the absence of tile boundaries, lower backgrounds, and the ability to construct detectors from a wider range of materials that may not be available in large size, similar to megaelectron volt photon radiography.

Scintillator detectors were recently studied for laser-driven proton beam imaging [126]. Further advances in detectors and scintillators can be particularly beneficial to existing proton and ion accelerator facilities [127], [128], [129]. Time-of-flight (TOF) method is an alternative to residual energy measurement [130]. The requirement for picosecond timing resolution in ToF is due to the fact that in a facility, such as LANSCE [127], the flight path (L_0) is limited to about 20 m. The required timing resolution ($\delta\tau$) is related to energy resolution through $\delta\tau/\tau = 0.41(\delta E/E)$. $\delta\tau$ is about 3 ps for $\Delta E/E$ of 10^{-4} and the flight time $\tau = 79$ ns for 800 MeV protons and 20-m proton flight path. Sub-picosecond timing resolution is desirable but difficult in order to achieve energy resolution of 10^{-5} for the same proton energy and real estate.

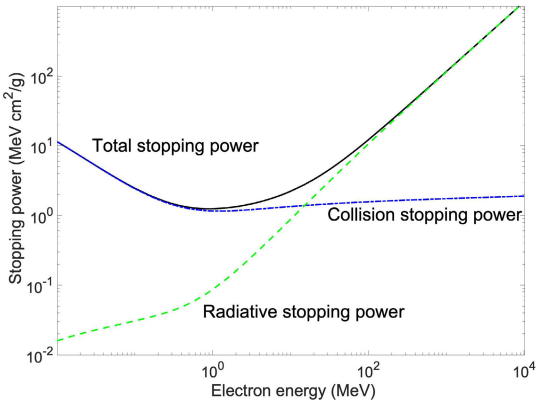

Fig. 13. Energy-dependent electron stopping power in LYSO with an atomic number ratio of Lu:Y:Si:O = $2(1-x)$:$2x$:1:5 and $x = 0.075$. the density is assumed to be 7.2 g/cm^3. The data are from the NIST/ESTAR database.

E. Electrons

Electrons in the energy range of 6–20 MeV have been used in the treatment of cancers of less than 5-cm depth for many years [131]. A portable electron radiography setup at the electron energy of 30 MeV has been reported [132]. Permanent magnet quadrupoles were used to focus electrons to form radiographic images of thin static and dynamic objects at about 2 m away. The objects had a nominal areal density sensitivity range of 10–1000 mg cm^{-2}. The spatial resolution was found to be about 100 μm. Electron radiography was recently extended to 14 GeV at the linac coherent light source (LCLS) [133], and also called transmission high energy electron microscopy (THEEM). In addition to the highly relativistic electrons, an additional feature of the THEEM was the very short electron bunch duration down to 1 ps, which offers a very high resolution of dynamic processes. A 400-μm-thick columnar CsI scintillator was used in conjunction with a CCD camera to collect the focused electrons with a spatial resolution below 10 μm. Recently, the development of higher-charge laser plasma accelerator-driven electron production [134] has enabled ultrafast (sub-picosecond) imaging using electrons [135]. This source generates a broad spectrum of electrons, with a peak energy above 200 MeV, and maximum flux (or current density) around 20 MeV. Using the OMEGA EP lasers as a source, target-on-detector and projection radiography have been demonstrated on inertial confinement fusion (ICF) scale targets [136]. Work is underway now to implement a similar lens-based system within the confines of OMEGA EP to project high-quality electron radiography onto a fast detector system, enabling flash electron radiography for ICF experiments.

Energetic electrons interact with other electrons and nuclei through collisions and long-range Coulomb force and lose energy through radiation of photons and direct energy transfers to other electrons in materials. Fig. 13 shows the energy-dependent stopping power of energetic electrons in LYSO at energies up to 10 GeV. Collisional and Coulombic scattering energy loss dominate over the radiative energy loss at low energies up to 15.2 MeV.

One attractive potential of a THEEM is that the colocation of the electrons and the XFELs using a single (electron) accelerator would allow dual-probe radiography of electrons and X-rays. Such a dual-probe of electron and X-ray could be simpler than dual-probe radiography based on protons and photons, which may require two accelerators, one for the electrons to generate X-rays, the other for the protons [137]. Alternatively, due to the strong bremsstrahlung radiation from a relativistic electron beam, electron radiography is intrinsically a multiple probe technique by itself if the bremsstrahlung information can be decoded. Multi-gigaelectron volt electron radiography or THEEM can potentially deliver 1-μm spatial resolution through objects of 1-mm thickness.

In summary, opportunities for experimental scintillator detector development for electron IT include: 1) experimental study of LYSO for higher LY and 2) scintillator thickness optimization for higher resolution. These studies will likely lead to better results than using columnar CsI. Another opportunity is to search for scintillators for dual-probe IT, such as electron-X-ray IT.

F. Positron-Induced γ-Rays (511 keV)

Inorganic scintillators are used in PET [138]. Recent PET makes use of TOF information to increase the SNR in the reconstructed image and improve the location of the annihilation event. The emergence of new technologies in nanophotonics, microelectronics, artificial intelligence (AI), and so on opens new perspectives for PET scanners to break present performance limits. An ambitious goal has been set in the frame work of the 10-ps TOF-PET challenge [139].

Achieving this ambitious goal would improve the effective PET sensitivity by a factor of 20 over the biograph vision from Siemens, Munich, Germany [140], opening the way to reducing the radiation dose (currently 5–25 mSv for whole-body PET/CT), scan time (currently $>$ 10 min), and costs per patient (currently $>$ 1000 € per scan), all by an order of magnitude. One of the most important components in TOF-PET instrumentation is the scintillation crystal. In spite of many efforts, in particular co-doping strategies, to reduce the delay between the creation of the hot electron–hole pairs and the capture of the resulting slow charge carriers by the luminescent centers after their multiplication and relaxation in the medium [141], [142], [143], standard scintillation mechanisms

in inorganic scintillators are unlikely to produce a scintillation photon rate large enough to break the present barrier of about 200-ps coincidence time resolution (CTR). Several approaches are investigated to boost the timing resolution of scintillator-based X-ray and γ-ray detectors. The first one consists of exploiting a few Cerenkov photons produced by the recoil electron from the PE γ-ray interaction in the medium. The second one is based on metascintillators where the recoil electron is sampled in thin layers of fast organic scintillators or ultrafast nanoscintillators. A third, longer term possibility, is to boost the coupling of the electromagnetic wave associated with particles traversing a medium with the optical states in the medium, increasing, therefore, the scintillation quantum efficiency and exciton radiative recombination rate.

1) Improving TOF With Cerenkov Light: Due to their high densities and refractive indices, the majority of crystals used in PET scanners have a relatively low Cerenkov threshold on the order of 100 keV. As the recoil electron following a PE interaction has an energy of 511 keV minus the binding energy of this electron in the deep core level of the component heavy nucleus or atom [91 keV in BGO and 63 keV in L(Y)SO], it is emitted with an initial energy of 420 keV (BGO) and 448 keV [L(Y)SO], respectively, i.e., well above the Cerenkov threshold. A number of Cerenkov photons (17 on average for BGO and 12 for LYSO) are, therefore, produced and can potentially be used to time tag the γ conversion events. This bunch of Cerenkov photons increases the photon rate in the leading edge of the scintillation pulse, as shown in [144].

The number of detected photoelectrons from Cerenkov emission is generally no more than 5 on average per event and is subject to large fluctuations from event-to-event. This poses severe constraints on the electronics and results in a nonnegligible number of events, where zero Cerenkov photons are detected in at least one (if not both) crystal in coincidence. However, a clever sorting of all the events in several classes associated with different amounts of Cerenkov photons detected in BGO crystals in coincidence, Fig. 14, has led to a significant improvement in CTR, which can provide useful information for improving SNR of the reconstructed image [145]. The value of about 200 ps obtained for 20-mm-long BGO pixels is interesting as it is similar to the state-of-the-art with LYSO crystals in the biograph vision PET scanner but with three times cheaper BGO than LYSO. This can start a new life for BGO, with an objective of 300–500-ps CTR at the system level and a cost-effective total-body PET.

2) Metascintillators: The metascintillator concept, introduced in [146] and first tested in [147], is based on composite scintillator topologies allowing the sampling of the recoil electron produced by the γ-ray conversion in dense scintillator regions in much faster scintillators, such as organic, core-valence luminescent (CVL), or nanoscintillators (see Fig. 1 in [148], for example).

A first generation of metascintillators is now pursued by combining the high stopping power of BGO or LYSO crystals with the fast emission of plastic scintillators [149] or CVL crystals, such as BaF_2 [148], [150]. The stochastic nature of the energy sharing between the metascintillator components poses challenges in energy resolution and event selection

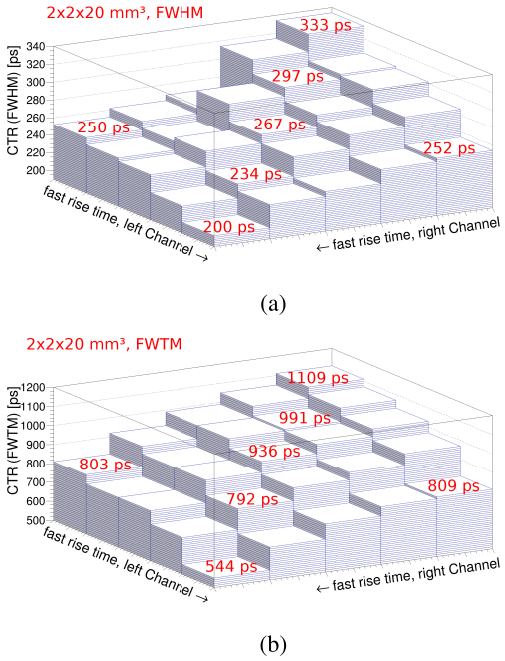

Fig. 14. CTR full width at half maximum (FWHM) (a) and full width at tenth-maximum (FWTM) (b) from the 25 coincidence categories between five classes of events per detector (20% of events each) sorted by their individual timing resolution in 20-mm-long BGO pixels. From [145] with permission.

if the different components have a different LY and in the timing resolution. However, different surrogates, based on the light pulse analysis, allow the estimation of the amount of energy sharing on an event-to-event basis and the necessary corrections [151].

The metascintillator results obtained so far confirm that a CTR of 200 ps at the system level can be reached with BGO-based low-cost metascintillators, equivalent to the state-of-the-art with bulk high-cost LYSO crystals. On the other hand, LYSO-based metascintillators allow CTR to reach 100 ps [152], twice as good as the state-of-the-art. It is worth noticing that the concept of metascintillator has been recently extended to a semimonolithic block geometry [150], benefiting from these excellent timing properties while allowing the determination of the depth of interaction (DOI) of the γ-ray interaction with 2–3-mm precision. From the knowledge of the DOI, a correction on the timing can be applied, allowing a further improvement of 20–30 ps to the CTR.

Decay times of 100–500 ps have been observed in ZnO:Ga quantum dots [153] or CdSe nanoplatelets (NPLs) [154]. This has triggered extensive research toward a second generation of metascintillators, e.g., CdSe NPLs [155], ZnO:Ga nanopowder [156], perovskites [157], mixed inorganic–organic perovskites, such as $CsPbBr_3$ with methylammonium, and GaN/InGaN multiple quantum wells [158].

An interesting attempt has been made to deposit layers of $CsPbBr_3$ nanocrystals on GAGG:Ce plates, resulting in a clearly identified bunch of prompt photons on top of the GAGG scintillation pulse [157]. A number of problems remain to be solved to benefit from the excellent scintillating properties, and in particular, the ultrafast emission of

nanoscintillators. These problems are related to the important self-absorption in several of them and the long-term stability of perovskites. We can fortunately rely on the huge research and development and industrial effort on perovskites for photovoltaic applications and we can expect progress on the large scale and cost-effective production of excellent quality and stable perovskites.

Different solutions are being investigated to mitigate the problem of self-absorption in perovskites. One solution consists of embedding perovskites in transparent organic materials, such as polyethylene or polystyrene [159], with different strategies to transfer the excitation from the nanocrystals to or from the organic host [160]. Using PhCs to control optical photons is also being pursued [161].

G. Dosimetry in Radiation Therapy

Photon, electron, and proton beams, embedded radioactive sources, and injected radioisotopes are used therapeutically in medical applications, predominantly in the treatment of cancer. These radiation dose distributions can be highly complex, and suitable RadIT tools, including scintillators, are required for characterizing beam and source shapes and spatial and temporal distributions of intensity.

Scintillator dosimeters are used for machine characterization, machine quality assurance (QA), and patient dose measurement in radiation therapy. Scintillator detectors have been developed for machine testing of X-ray radiosurgery devices [162] and to measure patient treatment plans for X-ray-based radiation therapy [163]. One common detector format is the miniature plastic scintillation dosimeter (PSD), where a small volume of the plastic scintillator is attached to a fiber-optic light guide leading to readout electronics. The intensity of the scintillator light output can be converted to an absolute radiation dose reading. Organic scintillators, including BC-400 [164], EJ-260 [165], BC-531 [166], and others are commonly used in radiation therapy. Organic scintillators have many good properties for radiation dosimetry, including water equivalence in the clinical photon and electron beam energy range with minimal beam perturbation and energy-independency above 125 keV, reproducibility, linearity, and dose rate independence [167], [168], [169]. PSDs usually provide similar dosimetry results to ionization chambers (the standard radiation detectors for most radiation therapy applications) in both photon and electron beams while being much smaller and much more flexible [168], [170]. Certainly, the temperature dependence of scintillator light output needs to be considered to get correct results [171], especially in cases of in vivo dosimetry where the scintillator will be operated at body temperature but may be calibrated at room temperature [172]. It is also important to correctly account for the Cerenkov light produced in the optical fiber [167], [173].

Inorganic scintillators, such as Scintacor GS1, ZnSe:O, and CsI:Tl, while lacking radiological water-equivalence, typically provide a higher light output and are denser, which can be advantageous in some applications [174]. However, the high cost or the difficulties to grow single crystal ingots limit the application of inorganic scintillators for some applications. One example is 3-D scintillation dosimetry, which has used organic liquid [175] and plastic [165] scintillators due to their low cost and large volumes in almost any shape or size.

Scintillators have been widely used in radiation therapy, especially in X-ray based photon therapy. The major clinical applications include: 1) small-field dosimetry and 2) in vivo dosimetry. With the increased use of stereotactic body radiation therapy (SBRT) and stereotactic radiation surgery (SRS) (for example, GammaKnife and CyberKnife) to treat small tumors, small field dosimetry has become more important in radiation therapy. Unfortunately, it is very challenging to get accurate results in small field dosimetry due to: 1) loss of charged particle equilibrium; 2) energy dependence; and 3) partial volume effects if the detector is too large (e.g., ion chambers). Scintillators are an ideal solution in these scenarios. Due to the radiological water-equivalence of plastic scintillator materials, charged particle equilibrium is maintained and the detectors' energy dependence mimics that of water. The high light output of many scintillators allows PSDs to be made very small, avoiding partial volume effects.

The unique dosimetric features of PSDs make them ideally suited to the challenging problem of measuring very small radiation fields. Given a field size smaller than 10 mm, the scintillator results were closer to the MC simulation results compared with diode, microdiamond, and microLion chambers [176], [177], which are commonly used. Some commercial products have become available in the market, including the Exradin W1 and W2 Scintillator detectors (Standard Imaging, Middleton, WI, USA), which have become popular for small-field dosimetry [169].

Another important application of scintillator dosimetry in radiation therapy is the measurement of patient dose during radiation therapy delivery. PSD's radiological water-equivalence allows them to be placed in the radiation field without perturbation, while their operation without a high bias voltage makes them safe for measurements on or even inside of patients. The flexibility of PSD's is well suited, for example, to rectal balloon-mounted detectors for prostate dose verification, such as the OARtrac Dose Monitoring System (RadiaDyne, Houston, TX, USA) and detection of radioactive source position in needles or catheters for high dose rate (HDR) brachytherapy [178].

Scintillator detectors have also found extensive use in proton beam therapy applications for beam performance quality assurance testing. Errors in the proton beam range might result in missing the target or overdosing on nearby critical tissues or organs, both leading to unfavorable patient outcomes. Therefore, it is critically important to check the proton beam range routinely. The American Association of Physicists in Medicine (AAPM) Task Group (TG) 224 [179] recommends a monthly consistency check of the proton beam range. However, the conventional method of using a multiple-layer ion chamber (MLIC) can be very time consuming and provides limited spatial resolution. Scintillator detectors have been developed specifically for efficiently measuring proton beam range, which provides fast, accurate, and high-resolution beam range measurements [180], [181]. Scintillator-based detectors are also used for other proton machine QA tests, including

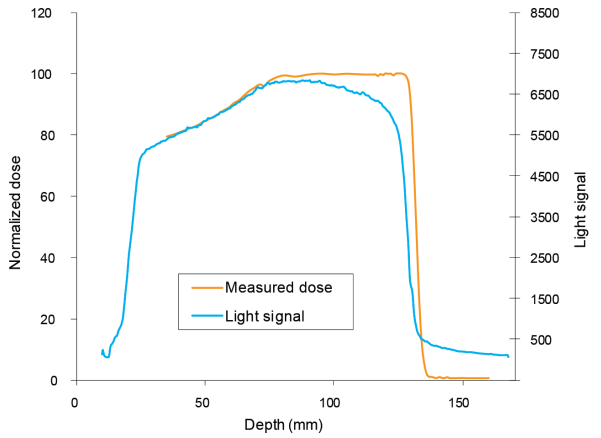

Fig. 15. Depth-dose curves of a proton spread-out Bragg peak (160-MeV maximum energy, maximum beam range 13 cm after passing through a 5-cm water-equivalent range shifter) measured with an ionization chamber (orange) and a liquid scintillator detector (blue). The scintillator signal is depressed near the end of the beam range due to ionization quenching.

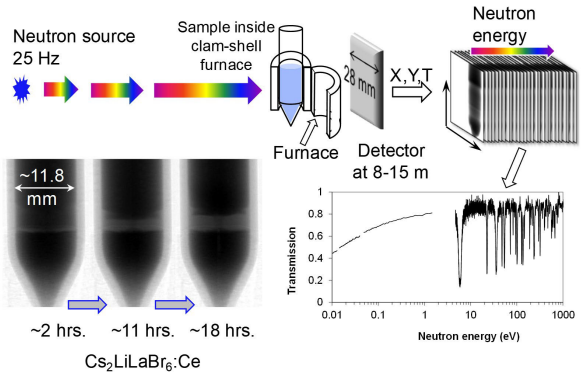

Fig. 16. Schematic of the energy-resolved neutron imaging experiment. A crystal growth furnace is placed directly in the neutron beam in front of a neutron counting detector. Thousands of images are acquired simultaneously, each corresponding to a specific neutron energy. Neutron transmission spectrum is, thus, measured for each pixel of the transmission dataset. Reproduced with permission from [190].

beam isocentricity [182], pencil beam profile and positioning testing [183], and daily comprehensive beam testing [184]. One limitation of scintillator detectors for proton therapy is the ionization quenching of most scintillator materials. As the protons' linear energy transfer (LET) increases toward the end of their range [185], the linear dose-to-light relationship breaks down, leading to an under-response of the scintillator, as shown in Fig. 15. This relationship is described by the well-known Birks relationship [186], which can be used to provide quenching correction factors, presuming the LET can be determined [166], [187].

In summary, radiation therapy is an important tool in the treatment of cancer, including brachytherapy, external beam radiation therapy, and particle therapy. Scintillator dosimetry plays an important role in radiation therapy; however, its potential has not been fully exploited. Additional research and development and collaboration, especially from outside the medical physics community, is needed to use scintillator dosimetry and RadIT more to improve the therapeutic efficacy of radiation therapy.

H. In Situ Neutron Imaging to Optimize Crystal Growth

The discovery of new scintillators or semiconductor materials typically starts with very small grains of synthesized samples. Once important properties have been characterized for these small samples, a proper crystal growth recipe has to be developed for producing large crystals to meet the requirements of specific applications, especially where large volumes are required by the relatively long attenuation length, e.g., as in γ-ray and fast neutron detection, see Section III-B and IV-D. The latter step often limits the transition of a promising material to industrial-scale manufacturing. These crystals need to be grown reproducibly, with high yield and affordable. Most of the time, multiple trial-and-error attempts are conducted and the grown materials are characterized ex situ by various nondestructive and destructive techniques. The number of such optimization runs is limited by the time required for each attempt. If various crystal growth parameters could be monitored during the growth in real time, the search for proper growth parameters would be much easier, faster, and cheaper. However, only a limited number of parameters can be measured in situ without disturbing the growth. Remote sensing of growth parameters is, most of the time, obscured by the equipment used for the crystal growth and by the opacity of the grown materials themselves to conventional probes, such as photons and electrons. It has been demonstrated recently that energy-resolved neutron imaging can monitor, in situ, various growth parameters, such as elemental distribution within the solid material and the melt, the location and shape of the liquid–solid interface, mosaicity of solidified material, segregation, and diffusion of dopant elements, and the presence of defects and others [188], [189], [190], [191], [192]. Although these demonstrations were only for the Bridgeman crystal growth process, this novel in situ diagnostic can be extended to other growth techniques due to neutrons' capability to penetrate many materials, including metals. Although the number of facilities where such neutron measurements can be conducted is very limited at the present time, the crystal growth optimization technique described here is useful for developing better crystal growth recipes, which then can be transferred to the industry.

The neutron imaging setup for monitoring in situ crystal growth in a furnace is shown in Fig. 16. A neutron counting detector with 512 $\times$ 512 pixels (55-μm pitch) was used [193]. The detector used neutron-sensitive microchannel plates to convert the incoming neutrons into a charge of $\sim 10^5$ electrons, and a pixelated timepix readout for high counting rate operation. The spallation neutron source delivered short pulses of neutrons at 20–60 Hz. The neutrons propagated over a 10–15-m path length toward the sample and the detector. The energy of each registered neutron is reconstructed from its time of flight. The short duration of the neutron pulses is, therefore, crucial for measuring the neutron transmission spectrum in each pixel of the imaging dataset. Some growth parameters (such as the location and the shape of the liquid–solid interface, qualitative uniformity of elemental composition, and location of defects) can be measured with regular neutron imaging, where a white transmission spectrum is measured for each pixel. A wider range of parameters can be investigated

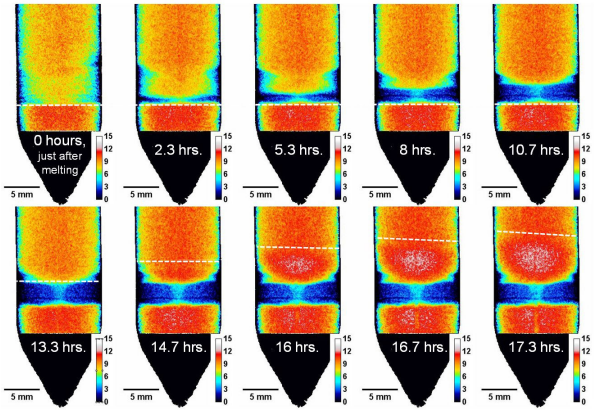

Fig. 17. Maps of Li concentration within the growth volume of $Cs_2LiLaBr_6$:Ce charge. Dashed lines represent the location of solid/liquid interface. During the first 11 h, the temperature profile and the ampoule location were kept steady. A Cs-rich/Li-deficient phase formed within the melt. The color bar represents the Li concentration in atom %. Reproduced with permission from [190].

with a pulsed neutron beam where transmission spectra that depend on the isotopic composition can be measured as a function of neutron time of flight for each pixel.

One strength of energy-resolved neutron imaging is to use neutron resonance absorption to separate neutron attenuations from different isotopes, and thus, to map the isotopic compositions for several elements [194], [195], [196], [197], [198]. An example of measured transmission spectrum for $Cs_2LiLaBr_6$:Ce can be found in [190].

It is well known that the shape, stability, and location of liquid/solid interface play an important role in the quality of material grown. A convex interface is often desirable. Observation of the interface is enabled by the presence of dopant segregation, which was used in several studies [189], [190], [192], [199], [200]. With neutron imaging, the shape and the location of the liquid–solid interface and the speed of ampoule translation could be optimized in real time by adjusting the temperature profile and the speed of translation. Moreover, the formation of two phases within the melt was observed during in situ growth of $Cs_2LiLaBr_6$:Ce crystal, as shown in Fig. 17. In the very first in situ growth of this crystal, it was found that Cs-rich/Li-deficient layer forms in the melt just above the solid phase. Good scintillator material was only grown after the Cs-rich layer is settled over about an 11-h period. Quantitative maps of Li concentration, shown in Fig. 17 for different times of crystal growth, demonstrate the formation of this Cs-rich layer at a steady temperature distribution. Once phase separation within the melt stabilized, the temperature profile was gradually changed, and a good crystal could be grown. Discovering the need for that stabilization blindly, as it was done by the industry before that experiment was conducted, was obviously a much longer process. This experiment showed that neutron imaging can substantially reduce the cost and time of the transition from the discovery of new candidate materials to the industrial growth of bulk crystals.

I. Space Applications

With the continued decline in rocket launch cost, a rapid increase in the number of robotic and human missions throughout the solar system, and commercialization of the low Earth orbit (LEO), scintillators and RadIT applications in space are a new frontier poised for significant growth.

Scintillators and imaging detectors have long been used in X-ray, γ-ray, and high-energy astronomy from space [201], [202], [203]. X-/γ-ray and neutron instruments are important for planetary missions to localize water, ice, and other resources [204]. Increasing human presence through, for example, permanent habitation in LEO, longer duration exploration missions, Mars colonization, space tourism, and in-space manufacturing, will need to qualify ground-based X-ray CT and other RadIT technologies for in-space human health and medicine [205]. LEO commercialization needs scintillators and RadIT to monitor the aging of space assets without the shielding by the Earth's atmosphere and magnetic fields, and assess the quality of the parts manufactured in space in situ.

Due to the significant background radiation, space applications need better scintillators than traditional space-qualified ones, such as NaI (Tl), CsI (Tl), and BGO. In addition to particle identification (background and noise rejection), radiation hardness, energy resolution [206], [207], LY, and others described in Section II-B, another unique requirement is the constraints in size, weight, and power (SWaP) for all space instruments and components. For X-ray, γ-ray spectroscopy and imaging, energetic trapped particles, cosmic rays, and neutrons coexist as the background noise in the harsh environment of space. Promising bright scintillators, such as L(Y)SO, $LaBr_3$, or $LaCl_3$, have intrinsic background that may not be suitable for low-noise operations due to in-space activation and the radioactive decays of ^{176}Lu (2.6% natural abundance and 3.8×10^{10} year half-life), ^{139}La (0.09% natural abundance and 1.0×10^{11} year half-life) [208]. Other scintillators being assessed for space imaging missions include $CeBr_3$ [203], CLLB:Ce [207], CLYC-7 [207], GAGG:Ce [209], [210], and SrI_2:Eu [207]. A new class of perovskite scintillators that can be synthesized in liquids and low temperatures has recently been considered for space applications. Lead-free halide perovskite Rb_2CuBr_2 (density 3.83 g/cm^3) [211], for example, was reported to have more than twice the LY of LYSO [11]. Other examples of water-grown or hydrothermal scintllators include $CsPbBr_3$ single crystal [212], $Cs_2NaTbCl_6$ [213], and $(ETP)_2MnBr_4$ [214]. Material instability, scintillator light self-absorption, toxicity, and relatively small sizes of the perovskite scintillators [215] necessitate further studies before they can be qualified for space use. For neutron RadIT in space, X-ray, γ-ray, cosmic ray, and energetic particle rejection is an important considerations. Solution-grown trans-stilbene single crystals [216] are being considered together with commercial plastic scintillators for neutron detection in space and planetary missions [217].

We mention two additional trends briefly as they are in a relatively early phase of development. First, heterogeneous and structured scintillators are being pursued for space applications, since a single type of scintillator or structure may not meet all the necessary performance requirements. A phoswich detector combining a $LaCl_3$ + LiI:(Eu,Sr) and pure $LaCl_3$ crystals for discriminating thermal neutron, fast neutrons, from γ-rays, is under study (Sonu, in Table III). Another example

is the quintuple discrimination of α-particles, βs, γs, thermal neutrons, and fast neutrons (Bertrand, in Table III). The composite organic scintillator detector is a three-layer phoswich. Second, 3-D IT in space is emerging despite the fact that they demand larger data capacities than spectroscopy and 2-D imaging. SWaP constraints have also been limiting the amount of data that can be gathered in robotic missions for a long time, but such limitations are being removed due to the advances in information technology for space missions. In addition to man-made structures in LEO, there is growing interest in using 3-D IT to collect more data from samples in situ, to map the Moon, Mars, and other planets in higher resolution. Computerized ionosphere tomography is an example to map very large natural structures in LEO [218].

J. Multimodal RadIT

Most current RadIT methods summarized in Section III can be characterized as a unimodal RadIT in the sense that a monochromatic/monoenergetic (narrow bandwidth in practice) X-ray/neutron, electron, or proton beam is used as the source of illumination, and a single parameter, such as scintillator light intensity, is recorded. A recent trend is multimodal RadIT (MM-RadIT), when more information [219], such as mass density and material identification simultaneously [220], can be extracted than by a traditional unimodal RadIT.

MM-RadIT comes in many varieties. A binary combination of the five methods in Section III leads to 20 different kinds. When two different energies for protons, electrons, and neutrons each are included as for X-rays, the number of varieties grows to 72. In practice, MM-RadIT has been reported in a much smaller number of varieties, in part limited by the available sources [221]. Two or more color X-ray CTs have already been used successfully in biology and medicine [222]. Examples of neutron and X-rays, neutrons and proton imaging can be found in [108]. From the signal collection perspective, light intensity/particle counts can also be used in conjunction with energy, momentum, polarization, and other light/particle properties for multimessenger RadIT. From the signal processing perspective, signals in real-physical space can be extended to the phase space for multidimensional RadIT, e.g., X-ray ptychography [87]. In the following, we give additional examples of detectors and data processing for MM-RadIT [22].

One of the key ingredients that enable dual-energy [222] and multicolor CT is energy-resolved X-ray photon counting detectors at a high flux ($\sim 10^9$ ph·mm^{-2}·s^{-1}). Two-layer scintillator detectors were described for dualenergy/multienergy CT, which consist of a thinner layer ($\sim$1 mm) of, e.g., YAG, ZnSe, or CsI, on the top, and a thicker layer ($\sim$2 mm) of Gd_2O_2S in the bottom [223], [224]. Novel ceramic scintillators were described with SiPM detectors [225]. CZT and CdTe can also resolve the energy of individual X-ray photons with good quantum efficiency [226]; however, due to material saturation (polarization at high X-ray fluxes, $<10^8$ Hz/mm^2), low mobilities of electrons and holes in CdTe or CZT and other effects, such detectors may not be able to handle the high photon fluxes in clinical CT [227].

ML-based methods for signal processing and image analysis are a promising direction and growing for both unimodal and MM RadIT [228], [229]. In one example, a deep convolution neural network (CNN) was used to discriminate signals induced by neutrons from γ-rays in organic scintillation detectors [228]. The pulse shape discrimination performance for the conventional charge comparison method was compared against the CNN discriminating algorithms for two different detectors to confirm the superior performance of the deep-learning model. In another example, CNN was able to generate higher fidelity images by leveraging the underlying physics of dual-energy CT [230]. It is equally important to include independent validations, such as through experiments, other models, or uncertainty quantification (UQ), of ML models.

IV. Recent Scintillators and Concepts

In addition to progress in new inorganic scintillators, Section IV-A, we shall highlight results and progress in structured scintillators presented during the SCINT22 conference, ranging from nanostructures, Section IV-B, micrometer-thick thin films, Section IV-C, to bulk composite structures, Section IV-D. As presented, each topic emphasizes a particular application: Section IV-A on new inorganic scintillators for fast timing, Section IV-B on nanostructures for light guiding and higher LY, Section IV-C on thin film for high X-ray imaging resolution, Section IV-D on bulk composites for fast neutrons. Many other new applications in RadIT may be found for each of the scintillators and novel structures. Section IV-E discusses the emerging opportunities associated with machine learning (ML) and data science.

A. Novel Ultrafast Inorganic Scintillators

Due to the gaps between desired scintillator performance and what is achievable with existing commercially available materials, continued exploration of novel scintillators is necessary. Consideration of materials with fast timing characteristics is especially important in applications, such as TOF-PET (discussed in Section III-F) or GHz hard X-ray imaging [46], [231]. BaF_2 has been strongly considered for this and other fast timing applications (such as TOF-PET via the heterostructure concept) but comes with several major drawbacks, including its dominant slow decay component ($\sim$630 ns), which leads to pulse pileup issues, and the spectral mismatch with common photodetectors due to its emission wavelengths lying in the VUV range. Additional discussions may be found in the recent reviews [3], [139], [232]. In this section, we highlight examples of new ultrafast (subnanosecond up to a few nanoseconds decay times) scintillators with the potential to overcome the limitations of current technology.

Of the various potential avenues for achieving faster timing performance, core-valence luminescence (CVL) is of particular interest due to the overall well-balanced set of properties that can be obtained—sub-nanosecond decay time, moderate density (3–6 g/cm^3), good chemical stability, and relatively bright emission, for example. Unlike the Cerenkov emission and hot-intraband luminescence, which produce very few photons per gamma interaction ($\sim$17 photons per 511-keV gamma for BGO [233]), CVL scintillators typically have LYs in the range of 1000–2000 ph/MeV (at 662 keV), making them more

practical for use in a wide range of applications. Likewise, the ability for these materials to be used in bulk form without significant effects from self-absorption provides an advantage over semiconductors. The generally higher density and Z_{eff} of fully inorganic CVL scintillators compared with halide perovskite nanocomposites and hybrid organic–inorganic crystals provide an advantage over these materials. With these considerations in mind, recent progress on the development of CVL scintillators will be presented next, and areas in which future efforts should focus will be identified.

Novel CVL scintillators that have been discovered in the last decade include Rb_2ZnCl_4 [234], [235], Cs_2BaCl_4 [236], Cs_3ZnCl_5 [237], and $BaGeF_6$ [238]. In addition to these novel materials, there has been renewed interest in the more traditional CVL scintillators $CsSrCl_3$, $CsMgCl_3$, and $CsCaCl_3$ due to the advances in photodetector technology and signal processing methods since they originally drew interest in the 1990s. The most promising of these seems to be $CsCaCl_3$ due to its high LY of 1371 ph/MeV and fast decay time of 2.47 ns. The CTR has recently been reported to be 148-ps FWHM for a $2 \times 2 \times 3$ mm^3 $CsCaCl_3$ pixel measured with a VUV SiPM (Hamamatsu, S13370-3075CN), which is superior to that of BaF_2 (CTR of 164-ps FWHM) measured with the same setup [239].

Cs_2BaCl_4 is one of the fastest and brightest (1.68-ns decay time and 1369-ph/MeV LY) materials recently studied in [239]. In a separate study, an even shorter decay constant of 1.2 ns and higher LY of 1700 ph/MeV (for the fast component) are reported [236]. Unfortunately, the instability of this compound at room temperature may hinder its usage, as Cs_2BaCl_4 reportedly decomposes upon cooling [239], [242]. This means growth from the melt will present substantial challenges.

Similar to the resurgence of $AMCl_3$-type compounds, Cs_2ZnCl_4 has resurfaced as a promising new ultrafast scintillator despite being discovered almost 20 years ago. Between 2003 (when it was initially discovered) and 2019, there were only three publications that reported scintillation properties of Cs_2ZnCl_4 [243], [244], [245]. In the past few years alone, that number has now doubled [237], [241], [246]. This is partly due to improvements that have been made to crystal growth techniques that have allowed for better quality and larger volume crystals to be fabricated. Fig. 18 shows some examples of different CVL crystals grown in recent years.

Several properties make Cs_2ZnCl_4 an attractive candidate for further investigation. It is nonhygroscopic, has a single-component decay time of around 1.7 ns, and has longer wavelength emission than BaF_2 [237], [241], [244], [245]. As a result of recent improvements to crystal quality, better performance has now been achieved with Cs_2ZnCl_4. Specifically, LY as good as 1980 ph/MeV (at 662 keV) has been measured for small crystals with approximate dimensions of $5 \times 5 \times 5$ mm^3 [241], surpassing that of the CVL component of BaF_2 (1400 ph/MeV). The CTR has so far been measured to be as good as 136 ps FWHM for two Ø7 × 3-mm-thick slabs of Cs_2ZnCl_4 measured in coincidence using SiPMs (Broadcom, AFBR-S4N44C013) [241]. This value is expected to improve

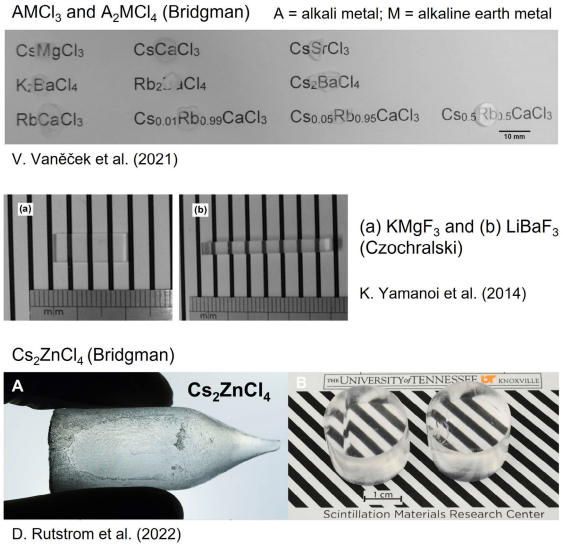

Fig. 18. Examples of some CVL crystals grown in the last decade. The growth methods are noted in parentheses next to each composition. (a) $KMgF_3$ and (b) $LiBaF_3$ (Czochralski). Reprinted from [239], [240], and [241], with permission from Elsevier.

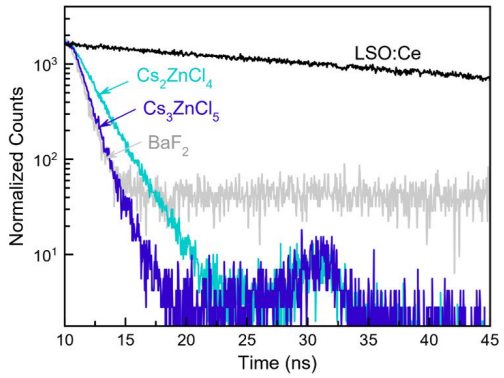

Fig. 19. Scintillation decay time profiles of Cs_2ZnCl_4 and Cs_3ZnCl_5 compared with BaF_2 and LSO:Ce. Crystals were measured using the Bollinger–Thomas single-photon counting method. The feature around 30 ns is an instrumental artifact. Adapted from [241].

with the optimization of the measurement setup. Another promising new Zn-based CVL scintillator is Cs_3ZnCl_5, which has a 0.82-ns decay time [241]. A comparison of the decay profiles of Cs_2ZnCl_4 and Cs_3ZnCl_5 with BaF_2 is shown in Fig. 19 to illustrate their ultrafast timing characteristics and lack of slow decay components.

Various strategies are currently being explored in an effort to improve the performance of radiation detectors for fast-timing applications. For scintillator-based detectors, the performance is ultimately limited by the scintillator's decay time; therefore, there is a strong push toward the discovery and development of ultrafast materials that may overcome the limitations of existing technology. Exploiting fast emission processes and the concept of metascintillators (or heterostructures) are two approaches in particular that have received much attention in the last few years. The compositional space in which CVL materials exist has not yet been exhausted, and continued efforts devoted to searching for and developing novel CVL

materials are necessary in order to find suitable alternatives to existing ultrafast inorganic scintillators, such as BaF_2. A deeper investigation into impurity-induced or impurity-enhanced CVL may also be a pathway for discovering new ultrafast scintillators and is a relatively unexplored area. If they are to be utilized in RadIT environments, the radiation hardness of newly developed CVL scintillators needs to be assessed, and future work should also prioritize denser materials.

B. Nanostructures

Structured scintillators are also called heterostructured scintillators or metascintillators. These scintillators combine materials with complementary properties to achieve functions better than any of the individual components, see Section III-F2 earlier and references therein for additional information on fast-timing applications. The application of structured scintillators is broader than fast timing. Phoswich scintillators have been described for particle identification in a number of works, as summarized in Table III. Innovations through structure engineering have also been recognized elsewhere [77].

In comparison with bulk scintillators, nanocomposite scintillators have features potentially including enhanced light output, reduced cost, and greater size scalability [247]. Optimization of monolithic nanocomposite and transparent ceramic scintillation detectors for PET was discussed in [248].

Patterning by plastic deformation or *nanoimprint* was developed in the 1990s [249]. It permits nanometer patterns in clean ambient air and without complex optics. Cerna et al. [250] tested nanoscale structured plastic scintillators for better light extraction. By using empirical methods for structuring commercial scintillating polymers surfaces, up to 50% more light was extracted by patterned surfaces. Additional results related to the Purcell effect, PhCs were reported, see Table III for additional examples.

C. Micrometer Thin Films

Two-dimensional X-ray imaging and 3-D microtomography with submicrometer resolutions can be achieved by using thin scintillators in synchrotron facilities when the X-ray flux can exceed 10^6 ph·s^{-1}·μm^{-2} [251], [252]. In a microscope setup that uses a thin scintillator screen to convert X-rays into visible light, the spatial resolution depends on the screen thickness, the depth of focus (or defect of focus), optical aberrations, and camera electronic noise. A spatial resolution of 0.8-μm FWHM (1000 line pairs/mm with 10% contrast) was reported [251]. Ce-doped crystalline YAG film of 5-μm thick was deposited on an undoped YAG substrate (170-μm thick). LSO:Ce less than 10 μm was used in another case. X-ray absorption is weak in these rather thin scintillators (about 1% at 30 keV and 0.25% at 50 keV per 1-μm-thick LSO). High material density is, thus, desired for high X-ray absorption efficiency, particularly at high X-ray energies.

One promising growth technique for such a range of thicknesses with high optical qualities is the liquid phase epitaxy (LPE), which allows single-crystal film deposited on a single-crystal substrate. Several materials, such as doped Lu_2SiO_5 (LSO), and many garnets doped with cerium, europium, or terbium, Lu_2O_3:Eu^{3+} have been developed as thin scintillating films [72], [253], [254]. Double layers (LSO:Tb^{3+} and LSO:Ce^{3+}) screens emitting at different wavelengths combined with double read-out systems spectrally filtered has been proposed to compensate the weak X-ray absorption [255]. At low X-ray energies, the absorption edges of the absorption films play a crucial role, and the composition may be adapted for specific energies as exemplified by Riva et al. [256].

The substrate is also of crucial importance and has several severe requirements. First, it has to be compatible with the epitaxial growth, i.e., showing the same crystalline structure and a weak lattice mismatch. Second, the X-ray absorption in the substrate is very large as compared with the scintillating film, the substrate has to be nonscintillating. Indeed, even a weak scintillation leads to an image out of the focal plane of the objective contributing to blurring the image. Finally, it has been recently shown using MC simulation and confirmed by experiments, that the secondary X-ray emission from the substrate may significantly affect the modular transfer function (MTF) [31], [36], [37] of the overall device and that effect strongly depends on the X-ray energy. This effect becomes very critical when ultimate spatial resolution is desired [257]. The figure of merit (FoM) presented combining the MTF at 500 lp/mm and the effective energy deposition in the active film (Fig. 20) highlights jumps due to the X-ray absorption thresholds as a function of the energy used to perform the X-ray imaging. These jumps are related to a combination of the X-ray absorptions of the film and the substrate, and the X-ray fluorescence of the substrate. It is shown, for example, that among the evaluated film/substrate combinations, it is preferable to use the GAP:Eu deposited on YAP in the 50–62-keV range and Lu_2O_3:Eu deposited on undoped Lu_2O_3 beyond 62 keV. This FoM does not take into account the optical qualities of the films, nor the scintillation efficiency. Because the performances are pushed to the limit, it suggests that the scintillating screens tend to become very specific to each energy range, even to small changes when approaching the absorption edge of their constituents.

D. Bulk Neutron-Sensitive Composite Scintillators

Scintillator detectors for pulsed fast neutron sources play a vital role in nuclear safeguards, material inspections, and fundamental science [258], [259]. While the combination of homogenous, monolithic scintillators (e.g., Cs_2LiYCl_6:Ce^{3+} and GS20) [260], [261] with moderator material (e.g., polyethylene) can meet some of the current requirements, difficulties arise from operating a large volume neutron detector in the harsh radiation environments with: 1) the ubiquitous gamma (γ) ray backgrounds and 2) the limitations imposed on the neutron count rate by the size and geometry of the detector material or readout electronics.

Detecting neutrons is unique due to the neutron's electric charge neutrality and isotope-dependent absorption cross section. Some neutron converter isotopes are ^{3}He, ^{6}Li, ^{10}B,

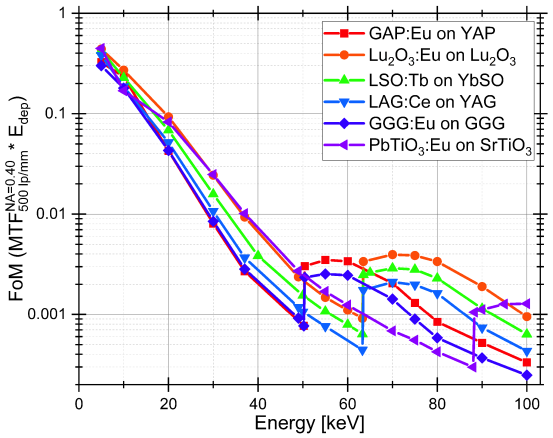

Fig. 20. FoM calculated from the contrast in the MTF blurred by optics (NA = 0.40) at 500 lp/mm and the energy deposited in SCF. Values are extracted from simulations at X-ray energies from 5 to 100 keV for 5-μm SCFs supported by 150-μm substrates. Reprint from [257] with permission.

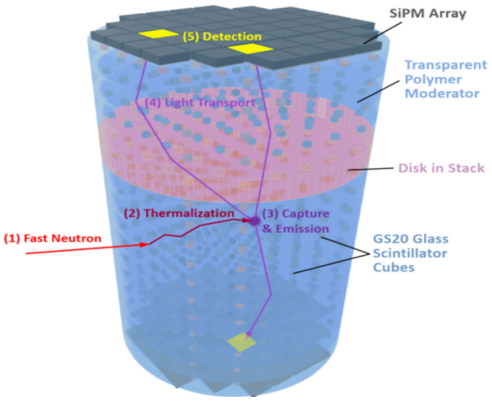

Fig. 21. Generalized fast neutron detector scheme using transparent composites. A fast neutron interacts primarily with organic constituents, slows down, and gets captured by the neutron-sensitive scintillating particle, e.g., GS20 scintillator cubes. The scintillating light is then detected by photodetectors, SiPMs, or photomultiplier tubes.

and ^{238}U [262], [263]. Time- and energy-resolved fast neutron detection requires efficient neutron detection in a relatively large volume (and, therefore, low cost) of neutron-sensitive materials [264]. Additional requirements or highly desirable properties include tolerance to radiation degradation for long periods of use, and particle or energy discrimination against the background, such as γ-rays. For neutron counting, short response time is often needed to improve temporal resolution, and event statistics, and to prevent event pileups. Generally, desirable detector attributes come with significant trade-offs due to the lack of an "ideal" scintillator for neutrons in practice.

Organic–inorganic composites represent a large group of diverse material combinations for fast neutron detection [265], [266], [267], [268], [269], [270], [271]. In an organic–inorganic composite, a fast neutron interacts primarily with the organic matrix, and energy then transfers to a scintillating material imbedded in the organic matrix. While neutron interaction rates with organic constituents can be relatively high compared with higher atomic number constituents, significant scintillation light scattering can occur due to the refractive index mismatch between the organic matrix and the scintillator material; ultimately, this optical property difference can reduce the mean free path of scintillation photons and contribute to optical losses [271], [272]. While the scintillation process is well-studied for homogenous scintillators, the optical composite parameter space can be vast. The main design criteria for organic–inorganic composite focus on scintillation light transport. The volume fraction of the individual constituents and the effective optical absorption coefficient of the resulting mixture are important factors. Fortunately, this unique multiparameter space can also enable flexibility in meeting targeted application specifications [265], [266], i.e., neutron interaction rate, temporal response, and light output to the photodetectors.

Recently, heterogeneous scintillating particle composite materials have demonstrated promising properties for compact fast neutron detection; specifically, these detectors can potentially address the needs for good detection efficiency, large active volumes, fast timing, and respectable radiation damage tolerances at a reasonable cost [272], [273]. Fig. 21 illustrates a fast neutron detection scheme using a scintillating particle detector with a nonscintillating moderator matrix. If a scintillating moderator matrix was used instead, additional scintillation light would be created during the moderation process. One main advantage of scintillating particle composite is that γ-ray suppression relies solely on the arrangement of small neutron-sensitive scintillating particles within the organic matrix. Many new possibilities exist with hybrid scintillator particle composites, e.g., scintillating particles with wavelength shifting coatings for improved light transport and performance stability, tunable dynamic range or segmented composite detector designs.

E. Data Science and ML for Scintillator Screening

Data science, ML, and AI have had a significant impact on physical sciences, including scintillator materials science over the past decade [274], [275], [276], [277], [278]. Data-enabled methods have been applied to expedite the development and optimization of luminescent materials. ML algorithms can efficiently encode chemical similarity and interpolate across high-dimensional feature spaces to screen potentially new scintillator compounds as well as to develop predictive models for their performance estimation.

A first-principle approach to the entire scintillator property portfolio prediction, as discussed in Section II-B, remains beyond the scope of the state-of-the-art computations. Recent studies have focused on alternative data-enabled routes for scintillator property predictions. A majority of the research in this direction has focused on predicting one or more scintillator performance metrics, such as light yield or response time, utilizing a prescribed set of features or descriptors that are largely selected based on domain knowledge. This surrogate model for efficient property predictions mainly implements the following key steps: 1) selection of easily accessible attributes or design variables (also referred to as features or descriptors) that are expected to be causally related to the target property

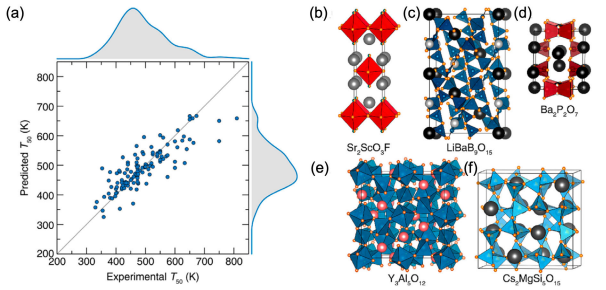

Fig. 22. (a) Parity plot cross validating ML predictions of thermal quenching temperatures with the corresponding experimental values for 134 compounds. Crystal structures of new host compounds predicted by the ML algorithm are: (b) Sc_2ScO_3F, (c) $LiBaB_9O_{15}$, (d) $Ba_2P_2O_7$, (e) $Y_3Al_5O_{12}$, and (f) $Cs_2MgSi_5O_{15}$. Sc, B, P, Al, and Si (Mg) occupy the center of the polyhedra. Sr, Li, Ba, and Cs are colored in different shades of gray. F is in green, Y is in pink, and O is in orange. Adapted from [281].

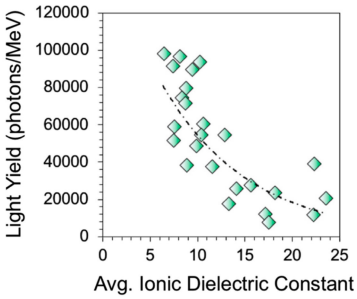

Fig. 23. Strong correlation between experimental light output of Ce- and Eu-doped scintillators and averaged ionic part of the dielectric constant of the host over a wide range of chemistries. Adapted from [282].

of interest; 2) integration of the identified variables in an ML model to establish a mapping between the materials and the target properties; and 3) assessment and analysis of the predictive power and generalizability of the developed models to identify design rules using unseen data. This framework has been applied to predict a range of properties that are either directly or indirectly connected to the performance of luminescent materials, including scintillators [279], [280], [281], [282], [283].

Zhuo et al. [280] employed a tree-based ensemble learning algorithm, along with elemental features (such as the average electronegativity, average polarizability), local configurational information, and the relative dielectric permittivity of the host medium, to train an ML model that could reliably predict 5d level centroid shift of Ce^{3+} substituted inorganic phosphors, a quantity that is critical in predicting the LY and thermal response of rare-earth substituted inorganic luminescent materials. In a different study, Zhuo et al. [281] developed an ML regression model using a set of 134 experimentally measured temperature-dependent Eu^{3+} emission spectra of phosphors to rapidly estimate the thermal quenching temperature—defined as the temperature when the emission intensity is half of the initial value—and subsequently used the model to screen more than 1000 oxide Eu^{3+} doped host compounds to select five new candidates, which were not included in the training dataset, with predicted thermal quenching temperatures $>$423 K (see Fig. 22). These compounds were eventually synthesized to validate this informatics approach. Closely following along similar lines of research, Park et al. [283] reported an integrated ML platform, consisting of 18 different learning algorithms, to evaluate and compare the performance of different models toward predicting the band gap, the excitation and emission wavelengths of Eu^{2+}-activated luminescent materials.

Going beyond the surrogate models for predictions of scintillation-related properties that are otherwise expensive to compute or time- and resource-intensive to measure directly, the data-enabled approach has also been applied to extract new insights and practically useful design parameters from scintillator materials databases. As a recent example, Pilania et al. [282] employed a curated dataset of scintillation LY and response time measurements for 25 Ce- or Eu-doped scintillator compounds to discover a strong correlation between the lattice contribution to the dielectric constant and the LY, regardless of the specific composition or crystal structure of the host material, as depicted in Fig. 23. This trend was then rationalized via the identification of a direct mechanistic connection between the light output and the efficiency of germinate recombination process through which hot charge carriers recombine to form excitons at an early stage of the energy absorption and thermalization process. At this stage, charge carriers multiply via impact ionization while settling down to the conduction and valence band edges by losing their energy to phonons. Throughout this process, the dielectric permittivity plays an important role in modifying the carrier Coulombic interactions via dielectric screening [282].

A major limitation of these surrogate models is that they cannot readily be applied to discover potentially new scintillators in large chemical spaces. Since these models are predominantly trained on scintillators and other closely related luminescent compounds, with either no or very few examples of nonscintillators, they generally fail to correctly distinguish scintillators from nonscintillators in large chemical spaces where a vast majority of compounds are, in fact, nonscintillators. There is a need for sufficiently accurate yet efficient predictive classification models to distinguish scintillators from nonscintillating compounds.

To address the classification problem for lanthanide (Ce)-doped inorganic scintillators, a recent study by Pilania et al. [284] focused on the positions of $4f$ and $5d_1$ activator levels relative to the host valence and conduction band edges as the main electronic structure indicator for a viable scintillator. If the activator levels are buried in the band edges, i.e., $4f$ in the valence band edge and/or $5d_1$ in the conduction band edge, respectively, the charge carriers generated by ionizing radiation cannot reach the activator sites to yield scintillation light via radiative recombination. On the other hand, if either the $4f$- or $5d_1$-level lands too far from the band edges, situated deep in the bandgap of the host, then again charge carriers will have to dissipate excess energy required to bridge the gap between the activator states and the band edges via a nonradiative process, such as energy transfer to phonons, before reaching the activator sites. This again is undesirable because it not only increases the response time but also decreases the overall efficiency of the scintillation

process. Ideally, it is preferrable when the $4f$ or $5d_1$ level is situated close to the band edges, but not too close to exciting the localized charge carriers back to the delocalized host bands by thermal vibrations. To make these more quantitative, the study utilized a well-known and widely used scintillator material Cs_2LiYCl_6:Ce (CLYC) as a reference. A classification metric was defined that compared the relative positions of the activator levels to the band edges in a new compound with those in the reference compound.

Using the above-mentioned domain-knowledge-informed criterion for scintillator/nonscintillator classification, two different regression models were trained and validated using a database of accurate experimental measurements of two key spectroscopic quantities, namely, the U and the D parameters [285], [286]. The U parameter is a quantitative measure of e–e repulsion in the $4f$ shell of lanthanides and is directly related to the electronic binding energy in the $4f$ shell. The D parameter, on the other hand, captures the relative shift of the lowest d level of a lanthanide ion in a given host environment with respect to that of the isolated ion in the vacuum, better known as the spectroscopic redshift. Knowledge of these two parameters, when combined with the accurate host bandgap computations using the Dorenbos chemical shift model [287], allows one to locate the relative position of the activator states with respect to the host band edges. This framework can be used to predict potentially novel scintillators during high-throughput screening. The efficacy of this approach toward practically identifying new compounds was further demonstrated using a case study on elpasolites or double perovskite halides of $A_2BB'X_6$ type. This class is known to harbor many known scintillator compounds and the physics-based classification approach was shown to correctly identify all the known scintillators within the target chemical space [284].

Despite the considerable progress in data-enabled scintillator (and related materials) design and development, many more exciting opportunities in active learning and adaptive design for scintillator discovery and optimization remain largely unexplored. Fig. 24 illustrates the essence of a closed-loop adaptive design approach [288], [289] for expedited scintillator development in a target chemical space. This iterative feedback loop starts with the available data on a set of key scintillator properties or performance metrics, which may be obtained either from accurate first-principles computations or direct measurements. Subsequently, existing materials knowledge in combination with advanced descriptor/feature selection tools can be employed to identify a set of physically meaningful and easily accessible descriptors for a targeted property. As a next step, an initial set of accumulated data is used to train a statistical inference model which estimates the property with associated uncertainties.

A key aspect of the design loop is the uncertainty associated with the properties predicted from inference, which is often accessed through bootstrapping or other model-specific routes, such as Gaussian process regression [290]. The uncertainties on the target properties play a key role in the adaptive experimental design which suggests the next material to be chosen for further calculation or experiments by balancing

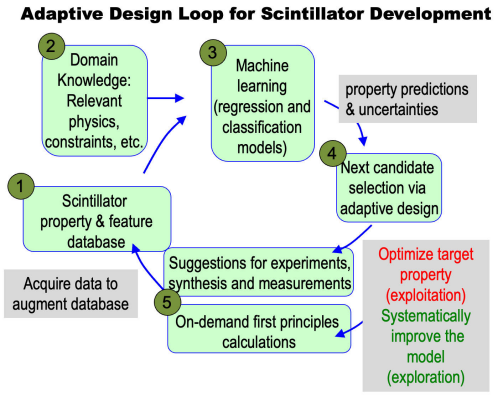

Fig. 24. Schematic illustration of the close-loop adaptive design and statistical inference approach to targeted scintillator discovery and development.

exploration and exploitation. That is, at any given stage several samples may be predicted to have given properties along with the associated uncertainties. The tradeoff is between exploiting the results by choosing to perform the next computation on the material predicted to have the optimal property or further improving the model by performing the calculation on a material where the predictions have the largest uncertainties. By choosing the latter, the uncertainty in the property is expected to (given the learning model) decrease, the model will improve (and its domain of applicability will expand) and this will influence the results of the next iteration in the loop (i.e., exploration) [290]. The new compounds proposed by the adaptive design strategy are then synthesized and characterized, and the new data are used to augment the training database. The loop repeats until one has identified a few materials and exploits the trained models that have the necessary performance and can serve as the starting point for further applied development or optimization. Note that a similar strategy can also be used during the optimization stages to further fine-tune newly identified scintillator chemistry for a given application.

In addition to active learning and adaptive design, numerous other emerging opportunities in the quickly growing field of materials informatics and ML are expected to significantly change the ways in which functional materials' discovery and development are going to be pursued. Going forward, increasingly efficient and improved ML methods integrated with advanced data infrastructure, automated, and autonomous robotics for high throughput experimentations, generative design of materials with targeted properties, and natural language processing for automated extraction of relevant information from the text and over the Web, are going to further push the boundaries of what is possible today with data-enabled routes for expedited development of novel luminescent materials.

V. Conclusion

Started by Röntgen and other pioneers at the dawn of the 20th century, the interdisciplinary field of RadIT science and technology is now more than 100 years old (young). Scintillators played pivotal roles since the very beginning when

TABLE III

SUMMARY OF SCINTILLATORS AND INTENDED APPLICATIONS BASED ON THE PRESENTATIONS DURING THE SCINT22 CONFERENCE. THE SCINTILLATOR METRICS INCLUDE LY, LINEARITY/NONLINEARITY OF THE LY AS A FUNCTION OF ENERGY DEPOSITION (NL), ENERGY RESOLUTION (σ_E), SINGLE-PHOTON SENSITIVITY (SP), SPATIAL RESOLUTION (δ), SPECTRUM TUNING CAPABILITIES (CL), LIGHT EMISSION ANISOTROPY (EA), HIGH DENSITY (ρ), HIGH *Effective* ATOMIC NUMBER (Z_{EFF}), EFFICIENCY OF ABSORPTION, ATTENUATION (EFF.), RADIATION HARDNESS (RH), DECAY TIME (τ_d), NEUTRON/γ-RAY DISCRIMINATION (N/γ), AND STABILITY TO ENVIRONMENT (SE), SUCH AS TEMPERATURE, HUMIDITY, ENVIRONMENTAL RADIATION, ADEQUACY FOR DOSE MEASUREMENT (DS), SIZE (SZ), AND COST

Composition	**Popular Name**	**Material Phase**	**Metric**	**Application**	**Institution** [First Author]
A_2XY_4 [av] *also* :Li doping		Perovskite crystal [av]	LY, τ_d		LRS-PORT [M. Sheikh]
BaF_2		crystal	σ_E, τ_d [a]	HEP HEP/cal., X-ray	CERN [b] [R. Cala'] Caltech [C. Hu] [b]
BaF_2:Y		crystal	τ_d	HEP HEP, X-ray	CERN [R. Cala']. Caltech [C. Hu]
(BaO:2SiO_2):Ce		glass	LY, cost	EIC	CUA/JLAB [T. Horn] BNL [C. Woody]
$Bi_4Ge_3O_{12}$	BGO	crystal crystal (segmented)	τ_d RH, SZ, SE [az], LY Z_{eff}, ρ, δ	PET dark matter γ-ray	i3M [D. Bonifacio] Cranfield U. [E. Rogers] USTC [C. Liu] LANL [N. Winch]
$Bi_4Ge_3O_{12}$/BaF_2	BGO/BaF2	meta-scintillator	τ_d	PET	i3M [D. Bonifacio]
$Bi_4Ge_3O_{12}$ + C_9H_{10} (Polyvinyltoluene)	BGO + EJ-232 (PVT)	hetero-structure [al]	τ_d	PET	CERN [F. Pagano]
C_7H_8 (Toluene)	[PPO] [l]	liquid	LY	Radio-chemistry	CEA/LNHB [b] [B. Sabot]
C_8H_8 (polystyrene)	BCF-10	plastic (fiber)	LY	muon	UNLV [J. Schoetker]
C_8H_8 (polystyrene)	BCF-20	plastic (fiber)	Z_{eff}, ρ, δ, LY	γ-ray	LANL [N. Winch]
C_8H_8 (polystyrene)	[PTP] [l] + [POPOP] [l]	plastic (fiber)	LY	LHC	UNL [ad] [B. Pinheiro-Pereira]
C_8H_8 (polystyrene)	EJ-276 [y]	plastic	LY LY, NL	proton C ion	UC Berkeley [T. Laplace]
C_8H_8 [ak] (polystyrene)	'nanoguide'	plastic fiber	LY, δ, EA	neutron	LANL [b] [D. Schaper]
C_8H_{10} (Xylene)	EJ-309	liquid	LY LY, NL	proton C ion	UC Berkeley [T. Laplace]
C_9H_{10} (Polyvinyltoluene)	BC-400 (PVT)	plastic	LY, τ_d, RH	heavy ion	GSI [M. Saifulin]
C_9H_{10} (Polyvinyltoluene)	EJ-200 (PVT)	plastic	LY, δ	neutron	LANL [D. Schaper]
C_9H_{10} (Polyvinyltoluene)	EJ-204 (PVT)	plastic	CL, LY [ae] LY LY, NL n/γ	γ-ray, X-ray proton C ion neutron (TCSPC)	UC Berkeley [J. Brown] UC Berkeley [T. Laplace] UC Berkeley [J. Sebastian]
C_9H_{10} (Polyvinyltoluene)	EJ-208 (PVT)	plastic	τ_d, LY	proton	LANL [M. Schanz]
C_9H_{10} (Polyvinyltoluene)	EJ-232Q (PVT)	plastic	n/γ	neutron (TCSPC)	UC Berkeley [b] [J. Sebastian]
C_9H_{10} (Polyvinyltoluene)	EJ-270 (^{6}Li) (PVT)	plastic	LY	neutron	STFC [G. Sykora] [b]
C_xH_y [ac]		polymer [ac] (film)	LY, τ_d, EA	α-particle	CNRS/U. Bordeaux [C. Cerna]
C_xH_y + C_uH_v [af]		plastic composite (three-layer)	n/γ/α/β [af]		CEA/U. Paris [G. Bertrand]
$CaMoO_4$	CMO	crystal	LY, SE	dark matter 0ν-DBD	IBS [I. Pandey] IBS [B. Mailyan]

TABLE III

(Continued.) SUMMARY OF SCINTILLATORS AND INTENDED APPLICATIONS BASED ON THE PRESENTATIONS DURING THE SCINT22 CONFERENCE. THE SCINTILLATOR METRICS INCLUDE LY, LINEARITY/NONLINEARITY OF THE LY AS A FUNCTION OF ENERGY DEPOSITION (NL), ENERGY RESOLUTION (σ_E), SINGLE-PHOTON SENSITIVITY (SP), SPATIAL RESOLUTION (δ), SPECTRUM TUNING CAPABILITIES (CL), LIGHT EMISSION ANISOTROPY (EA), HIGH DENSITY (ρ), HIGH *Effective* ATOMIC NUMBER (Z_{EFF}), EFFICIENCY OF ABSORPTION, ATTENUATION (EFF.), RADIATION HARDNESS (RH), DECAY TIME (τ_d), NEUTRON/γ-RAY DISCRIMINATION (N/γ), AND STABILITY TO ENVIRONMENT (SE), SUCH AS TEMPERATURE, HUMIDITY, ENVIRONMENTAL RADIATION, ADEQUACY FOR DOSE MEASUREMENT (DS), SIZE (SZ), AND COST

CdSe/CdS + Lu_2SiO_5:Ce	LSO	nano-platelets crystal	CL, LY, τ_d, SE	X-ray, γ-ray	CRNS/U. Lyon [Z. Meng]
$CdWO_4$		crystal	EA	dark matter	Tohoku U. [S. Kurosawa] [b]
			LY, τ_d	X-ray	UTK [K. Pestovich] [b]
			Z_{eff},ρ LY	γ-ray[e]	RMD [E. van Loef] [b]
$CeBr_3$		composite (fiber) [v]	Eff., δ		Tohoku U. [K. Kamada]
$CeBr_{3-x}I_x$		crystal (film)	LY, τ_d	X-ray	RMD [B. Singh]
$Cs_3Cu_2Cl_5$ [ar]		crystal	LY	X-, γ-ray	SICCAS [b] [Y. Wu]
$Cs_5Cu_3Cl_6I_2$ [ar]		crystal	LY, τ_d, $Z_{eff.}$, SE, σ_E	X-, γ-ray	SICCAS [b] [Y. Wu]
$CsCu_2I_3$ [ar]		crystal	LY, τ_d, $Z_{eff.}$, SE, σ_E	X-, γ-ray	SICCAS [b] [Y. Wu]
$Cs_3Cu_2I_5$ [ar]		crystal	LY	X-, γ-ray	SICCAS [b] [Y. Wu]
Cs_4EuX_6:Sm, X=Br, Cl		'sample'	LY, CL, τ_d	X-ray	Delft U. [C. van Aarle]
Cs_2HfI_6	CHI	crystal	DS	γ-ray	Tohoku U. [D. Matsukura] [b] [C. Fujiwara] [b]
CsI (pure)		crystal	σ_E, τ_d	electron	JINR [z] [N. Atanov]
CsI:Tl		composite (fiber) [v]	Eff., δ		Tohoku U. [K. Kamada]
		crystal	NL, σ_E	γ-ray	Teledyne FLIR [F. Liang]
			LY, τ_d	X-ray	UTK [b] [K. Pestovich]
			LY	proton	LANL [M. Schanz]
		'sample'	CL		Wake Forest U. [K. Ucer]
		crystal	n/γ/p/α SZ,τ_d	neutron	Kyungpook NU. [P. Vuong]
		crystal (segmented)	Z_{eff}, ρ, δ	γ-ray	LANL [N. Winch]
CsI:Eu		'sample'	CL		Wake Forest U. [K. Ucer]
CsI/^{6}LiBr:Tl		eutectic	LY	neutron	Tohoku U. [R. Yajima]
$Cs_2LiLaBr_6$	CLLB	crystal	LY	neutron	STFC [G. Sykora] [b]
$Cs_2LiLa(Br,Cl)_6$:Ce	CLLBC	crystal	SE [u], LY	neutron	RMD [N. Kaneshige]
			LY	γ-ray, neutron	Fisk U. [b] [R. Hawrami]
Cs_2LiYCl_6:Ce	CLYC	crystal	LY	γ-ray, neutron	Fisk U. [b] [R. Hawrami]
			n/γ	neutron	BARC/HBNI [b] [Sonu]
			LY	neutron	STFC [G. Sykora] [b]
			LY	neutron	Tohoku U. [b] [K. Kim] [R. Yajima]
$CsPbBr_3$		nano-crystal (NC) (Colloidal)	CL, LY	radio-isotope	CRNS/U. Lyon [M. Baravaglio]
		NC	RH	γ-ray	U. Milano-Bicocca [F. Cova]
		imbedded NC	τ_d, LY	X-ray, HEP	CTU [K. Děcká]
		imbedded NC [am]	τ_d	PET	CERN [F. Pagano]
		crystal			Delft U. [b] [J. van Blaaderen]
$CsPbBr_3$:F [aa]		nano-crystal	RH	γ-ray	U. Milano-Bicocca [F. Cova]
$CsPbBr_3$ + $(Gd,Ce)_3(Ga,Al)_5O_{12}$	GAGG:Ce	thin film crystal	τ_d, LY	X-ray, HEP	CTU [K. Děcká]

TABLE III

(Continued.) SUMMARY OF SCINTILLATORS AND INTENDED APPLICATIONS BASED ON THE PRESENTATIONS DURING THE SCINT22 CONFERENCE. THE SCINTILLATOR METRICS INCLUDE LY, LINEARITY/NONLINEARITY OF THE LY AS A FUNCTION OF ENERGY DEPOSITION (NL), ENERGY RESOLUTION (σ_E), SINGLE-PHOTON SENSITIVITY (SP), SPATIAL RESOLUTION (δ), SPECTRUM TUNING CAPABILITIES (CL), LIGHT EMISSION ANISOTROPY (EA), HIGH DENSITY (ρ), HIGH *Effective* ATOMIC NUMBER (Z_{EFF}), EFFICIENCY OF ABSORPTION, ATTENUATION (EFF.), RADIATION HARDNESS (RH), DECAY TIME (τ_d), NEUTRON/γ-RAY DISCRIMINATION (N/γ), AND STABILITY TO ENVIRONMENT (SE), SUCH AS TEMPERATURE, HUMIDITY, ENVIRONMENTAL RADIATION, ADEQUACY FOR DOSE MEASUREMENT (DS), SIZE (SZ), AND COST

		(substrate)			
Cs_4PbBr_6		nano- crystal [ao]	SE	PET, HEP X-ray	CTU [b] [V. Čuba]
Cs_2ZnCl_4		crystal	τ_d, LY LY, τ_d	X-ray HEP, X-ray, PET	Caltech [C. Hu] UTK [D. Rutstrom]
Cs_3ZnCl_5		crystal	LY, τ_d	HEP, X-ray, PET	UTK [D. Rutstrom]
Ga_2O_3		crystal	τ_d	X-ray	Caltech [C. Hu]
$Gd_3(Al,Ga)_5O_{12}$:Ce	GAGG	crystal	LY, NL RH Eff., τ_d Z_{eff},ρ, LY SZ, RH LY LY, RH LY, RH LY, SE, σ_E SE, Eff. SE [aaa]	X-, γ-ray cal. X-ray PCCT [g] HEP HEP proton proton, γ-ray X-ray, γ-ray γ-ray	LANL/UNM [T. Espinoza] INFN/U. Milano-Bicocca [M. Lucchini] STFC [S. Richards] U. Sussex [b] [N. Tuccori] FZU [b] [O. Zapalík] Crytur [S. Sýkorová] LANL [M. Schanz] U. Giessen [V. Dormenev] CERN [L. Martinazzoli] Korea U. [W. Lee] [A. Melis] [C. Park]
	GAGG+ (GaGG)				
also :Mg doping		crystal			
also :Mg doping		crystal			
		ceramic			
$Gd_3Al_2Ga_3O_{12}$ - X [p]	GaGG	crystal	LY, τ_d	γ-ray	U. Paris [D. Pailot]
$GdAlO_3$:Ce	GdAP	crystal	τ_d, ρ, LY	X-ray	FZU [M. Nikl] [b]
$(Gd,Ce,Mg)_3$- $(Al,Ga)_5O_{12}$ [q]	GFAG	crystal	LY, τ_d	γ-ray	U. Paris [D. Pailot]
$Gd_3Al_2Sc_3O_{12}$:Ce *also* :Pr doping	GSAG	crystal		HEP	FZU [O. Zapalík]
$(Gd,Y)_3Al_3Ga_2$- O_{12}:Ce	GYAGG	crystal	LY, τ_d		Vilnius U. [S.Nargelas]
$(Gd,Y)_3Ga_2Al_3$- O_{12}:Ce	GYGAG	crystal	NL, σ_E	γ-ray	Teledyne FLIR [F. Liang]
$Gd_3Ga_5O_{12}$:Ce [c]	GGAG	ceramic	LY, τ_d	X-ray	RMD [Y. Wang]
$Gd_2Hf_2O_7$:Nd	GHO	crystal	Z_{eff}, ρ, CL [x]	DS (remote)	Tohoku U. [S. Ishizawa]
$(Gd,Lu,Eu)_2O_3$	GLO	ceramic	Z_{eff}, ρ, δ, LY	γ-ray	LANL [N. Winch]
Gd_2O_2S	GOS or Gadox	ceramic	LY LY, τ_d	neutron X-ray	Kurchatov Inst. [I. Komendo] [b] RMD [B. Singh] [b]
Gd_2O_2S:Tb	P43	powder [o] film (screen)	RH, SP, τ_d LY, τ_d τ_d, δ	X-ray X-ray neutron	ESRF [K. Pauwels] IIT [A. Shultzman] [b] FRM II/TUM [A. Losko]
$Gd_3(Sc,Al)_5O_{12}$:Ce [c]	GSAG	crystal	LY, τ_d	X-ray	Charles U. [M. Kucera]
$(Gd, Lu)_3(Ga,Al)_5$- O_{12}:Ce		powder	LY, cost		UoD/UO [J. Indrei] [b]
$(GdX)_3(GaY)_5O_{12}$ [d]	GGAG	ceramic	LY, τ_d	X-ray	RMD [Y. Wang]
Gd_2SiO_5	GSO	crystal	SE, LY, CL, τ_d	0νDBD ($0\nu2\beta$)	USTC [Z. Jia]
H_2O + X H_2O + LS [hj]	WbLS [h] scintillator 'cocktail'	liquid	LY, cost τ_d, CL	$\bar{\nu}_e$ $\bar{\nu}_e$	UC Berkeley [b] [N. Tausik] [W. Wolszczak]
H_2O+ Au+X	LS [k] (Ultima gold)	liquid	LY [k]	Radio- chemistry	CEA/LNHB [b] [B. Sabot]
HfO_2		composite (nano)	Z_{eff},ρ	X-ray (medical)	FZU [I. Villa]
$LaBr_3$:Ce		crystal	LY, τ_d	X-ray	Delft U. [J. de Haas]
$LaCl_3$		crystal	n/γ n/γ/p/α SZ,τ_d	neutron neutron	BARC/HBNI [Sonu] Kyungpook NU. [P. Vuong]
$LaCl_3$:Ce		composite	Eff., δ		Tohoku U.

TABLE III

(Continued.) SUMMARY OF SCINTILLATORS AND INTENDED APPLICATIONS BASED ON THE PRESENTATIONS DURING THE SCINT22 CONFERENCE. THE SCINTILLATOR METRICS INCLUDE LY, LINEARITY/NONLINEARITY OF THE LY AS A FUNCTION OF ENERGY DEPOSITION (NL), ENERGY RESOLUTION (σ_E), SINGLE-PHOTON SENSITIVITY (SP), SPATIAL RESOLUTION (δ), SPECTRUM TUNING CAPABILITIES (CL), LIGHT EMISSION ANISOTROPY (EA), HIGH DENSITY (ρ), HIGH *Effective* ATOMIC NUMBER (Z_{EFF}), EFFICIENCY OF ABSORPTION, ATTENUATION (EFF.), RADIATION HARDNESS (RH), DECAY TIME (τ_d), NEUTRON/γ-RAY DISCRIMINATION (N/γ), AND STABILITY TO ENVIRONMENT (SE), SUCH AS TEMPERATURE, HUMIDITY, ENVIRONMENTAL RADIATION, ADEQUACY FOR DOSE MEASUREMENT (DS), SIZE (SZ), AND COST

		(fiber) [v]			[K. Kamada]
$LaCl_3$ + LiI [ab]		crystal	n/γ	neutron	BARC/HBNI [Sonu]
$La_2Hf_2O_7$:Yb *also* :Nd doping	LHO	crystal	Z_{eff}, ρ, CL [x]	DS (remote)	Tohoku U. [S. Ishizawa]
LaI:(Eu,Sr) [ab]		crystal	n/γ	neutron	BARC/HBNI [Sonu]
$(La,Gd)_2Si_2O_7$:Ce		crystal			ENSEMBLE3/ISM NAS Ukraine [O.Sidletskiy]
Li_3AlF_6/CaF_2		eutectic	LY	neutron	Tohoku U. [b] [R. Yajima]
$LiCaAlF_6$:X [i]	LiCAF	crystal	LY	neutron	STFC [G. Sykora] [b] Tohoku U. [K. Kim] [R. Yajima]
$Li_2Ca_{1-2x}SiO_4$:Pr_xNa_x [aab]			SE		FH Münster [F. Schröder]
$LiBr/CeBr_3$		eutectic	LY	neutron	Tohoku U. [b] [R. Yajima]
$LiBr/LaBr_3$		eutectic	LY	neutron	Tohoku U. [b] [R. Yajima]
$^6LiCl/LaCl_3$:Ce		eutectic	LY	neutron	Tohoku U. [K. Kim]
$LiCl/Li_2SrCl_4$		eutectic	LY	neutron	Tohoku U. [b] [R. Yajima]
$LiCl/BaCl_2$		eutectic	LY	neutron	Tohoku U. [b] [R. Yajima]
$LiF/BaCl_2$		eutectic	LY	neutron	Tohoku U. [b] [R. Yajima]
LiF/CaF_2		eutectic	LY	neutron	Tohoku U. [K. Kim] [b] Tohoku U. [R. Yajima]
$LiF/CaF_2/LiBaF_3$		eutectic	LY	neutron	Tohoku U. [b] [R. Yajima]
^6LiF/ $(Gd,Y)_3(Ga,Al)_5O_{12}$:Ce	GYAGG/ ^6LiF	composite powder (screen)	LY	neutron	Kurchatov Inst. [I. Komendo] [b]
$LiF/LiBaF_3$		eutectic	LY	neutron	Tohoku U. [b] [R. Yajima]
LiF/LaF_3		eutectic	LY	neutron	Tohoku U. [b] [R. Yajima]
$LiF/LiGdF_4$		eutectic	LY	neutron	Tohoku U. [b] [R. Yajima]
$LiF/LiLuF_4$		eutectic	LY	neutron	Tohoku U. [b] [R. Yajima]
$LiF/LiYF_4$		eutectic	LY	neutron	Tohoku U. [K. Kim] [b]
$^6LiF/ZnS$:Ag		powder (screen)	LY τ_d, δ	neutron	Kurchatov Inst. [I. Komendo] [b] FRM II/TUM [A. Losko] CSNS [B. Tang]
$Li_2Hf(Cl,Br,I)_6$		crystal	DS, CL	neutron	Tohoku U. [C. Fujiwara]
^6LiI:Eu		polycrystal	LY	neutron	STFC [G. Sykora] [b]
Li_2MoO_4	LMO	crystal	CL, LY α/β	double-β decay (0ν-DBD)	U. Milano-Bicocca [F. Cova] IBS [B. Mailyan]
Li_2O-CaO-SiO_2:Eu		polycrystal amorphous	LY	neutron	Kurchatov Inst. [I. Komendo]
$Li_2SrCl_4/LiSr_2Cl_5$		eutectic	LY	neutron	Tohoku U. [b] [R. Yajima]
$LiSrI_3$/LiI		eutectic	LY	neutron	Tohoku U. [K. Kim] [b]
Li_2WO_4		crystal	CL, LY α/β	dark matter (spin-depend.)	U. Milano-Bicocca [F. Cova]
Li_4ZrF_8		crystal	LY, CL, SE, τ_d	α, X-ray	Kyungpook NU. [D. Daniel]
$LuAlO_3$:Ce	LuAP	crystal	τ_d, ρ, LY Z_{eff},ρ,LY	X-ray PCCT [g]	FZU [M. Nikl] [b] U. Sussex [b] [N. Tuccori]
$Lu_3Al_5O_{12}$:Ce	LuAG	ceramic powder crystal	RH LY LY, RH	cal. proton, γ-ray	Caltech [C. Hu] UoD/UO [J. Indrei] [b] U. Giessen

TABLE III

(Continued.) SUMMARY OF SCINTILLATORS AND INTENDED APPLICATIONS BASED ON THE PRESENTATIONS DURING THE SCINT22 CONFERENCE. THE SCINTILLATOR METRICS INCLUDE LY, LINEARITY/NONLINEARITY OF THE LY AS A FUNCTION OF ENERGY DEPOSITION (NL), ENERGY RESOLUTION (σ_E), SINGLE-PHOTON SENSITIVITY (SP), SPATIAL RESOLUTION (δ), SPECTRUM TUNING CAPABILITIES (CL), LIGHT EMISSION ANISOTROPY (EA), HIGH DENSITY (ρ), HIGH *Effective* ATOMIC NUMBER (Z_{EFF}), EFFICIENCY OF ABSORPTION, ATTENUATION (EFF.), RADIATION HARDNESS (RH), DECAY TIME (τ_d), NEUTRON/γ-RAY DISCRIMINATION (N/γ), AND STABILITY TO ENVIRONMENT (SE), SUCH AS TEMPERATURE, HUMIDITY, ENVIRONMENTAL RADIATION, ADEQUACY FOR DOSE MEASUREMENT (DS), SIZE (SZ), AND COST

			RH	cal.	[V. Dormenev] INFN/U. Milano-Bicocca [M. Lucchini]
		crystal	Eff., LY	X-ray	STFC [S. Richards] ENSEMBLE3/ISM NAS Ukraine [O.Sidletskiy]
			SZ, RH LY	HEP PCCT [g]	Crytur [S. Sýkorová] U. Sussex [b] [N. Tuccori]
$Lu_3Al_5O_{12}$:Pr	LuAG	crystal	LY, RH	proton, γ-ray	U. Giessen [V. Dormenev]
			Z_{eff},ρ,LY	PCCT [g]	U. Sussex [b] [N. Tuccori]
(Lu,Ga)AlO_3:Ce [ai]	LuGAP	crystal [ai]	τ_d, ρ, LY	X-ray	FZU [M. Nikl]
Lu_2O_3:Nd		crystal	Z_{eff}, ρ, CL [x]	DS (remote)	Tohoku U. [S. Ishizawa]
Lu_2O_3:Yb		ceramic	τ_d, LY	X-ray	Caltech [C. Hu]
$(Lu,Hf)_4O_7$:Eu [ah]		thin film [ah]	$Z_{eff.}$, ρ, LY	X-ray	ESRF [L. Wollensen]
$LuPO_4$:Pr:Nd		nano- particle	CL	X-ray, cancer	FH Münster [J. Kappelhoff]
Lu_2SiO_5:Ce	LSO	crystal	τ_d, LY, RH	HEP/cal.	U. Giessen [V. Dormenev]
				proton	LANL [C. Morris]
			τ_d	PET	CERN [F. Pagano] [b]
$(Lu,Gd)_2SiO_5$:Ce	LGSO	crystal	τ_d	PET	CERN [F. Pagano] [b]
$Lu_xY_{1-x}AlO_3$:Ce	LuYAP	crystal	τ_d, ρ, LY	X-ray	FZU [M. Nikl] [b]
$Lu_xY_{1-x}Al_5O_{12}$:Ce [n]	LuYAG:Ce	crystal	SZ, RH	HEP	Crytur [S. Sýkorová]
$Lu_{2(1-x)}Y_{2x}SiO_5$:Ce	LYSO	crystal	τ_d	HEP/cal.	U. Notre Dame [T. Anderson]
			τ_d	PET	i3M [D. Bonifacio]
			τ_d	PET	CERN [F. Pagano] [b]
			τ_d	ToF	Caltech [C. Hu]
		crystal	RH	cal.	INFN/U. Milano-Bicocca [M. Lucchini]
			τ_d	HEP/cal., PET	Vilnius U. [G. Tamulaitis]
			LY	PCCT [g]	U. Sussex [b] [N. Tuccori]
		powder (screen)	LY	proton	LANL [C. Morris]
		crystal	LY	proton	LANL [M. Schanz]
		crystal	Eff., LY	X-ray	STFC [S. Richards]
(x=0.1-0.3) *also* :Ca/:Mg codoping		crystal	τ_d, LY, RH	HEP/cal.	U. Giessen [V. Dormenev]
NaI:Tl		composite (fiber) [v]	Eff., δ		Tohoku U. [K. Kamada]
Na_2MoO_4	NMO	crystal	Eff., σ_E	0ν-DBD	IBS [B. Mailyan]
$Na_2W_2O_7$	NaWO	crystal	LY, SE	dark matter	IBS [I. Pandey]
PbI_2		'sample'	LY, τ_d	X-ray	Delft U. [J. de Haas]
$PbWO_4$	PWO	crystal	EA	dark matter	Tohoku U. [S. Kurosawa]
			SE, RH	ECAL	U. Giessen [P. Orsich]
			SZ, RH	HEP	Crytur [S. Sýkorová]
	PWO-III		τ_d	HEP/cal., PET	Vilnius U. [G. Tamulaitis]
			τ_d, RH	EIC	BNL [C. Woody] CUA/JLAB [T.Horn]
$(PEA)_2PbBr_4$		crystal	SE, LY	X-ray	Delft U. [J. van Blaaderen]
			σ_E		
also :Li doping		thin film	τ_d, LY	HEP, PET	CERN [R. Cala'].
$RbCaBr_3$:Eu		crystal	LY, τ_d	X-ray	UTK [K. Pestovich]
Rb_4CaBr_6:Eu		crystal	LY, τ_d	X-ray	UTK [K. Pestovich]
Rb_2CuBr_3 [ap]		crystal	LY,τ_d, $Z_{eff.}$, SE,	X-, γ-ray	SICCAS [b] [Y. Wu]

TABLE III

(Continued.) SUMMARY OF SCINTILLATORS AND INTENDED APPLICATIONS BASED ON THE PRESENTATIONS DURING THE SCINT22 CONFERENCE. THE SCINTILLATOR METRICS INCLUDE LY, LINEARITY/NONLINEARITY OF THE LY AS A FUNCTION OF ENERGY DEPOSITION (NL), ENERGY RESOLUTION (σ_E), SINGLE-PHOTON SENSITIVITY (SP), SPATIAL RESOLUTION (δ), SPECTRUM TUNING CAPABILITIES (CL), LIGHT EMISSION ANISOTROPY (EA), HIGH DENSITY (ρ), HIGH *Effective* ATOMIC NUMBER (Z_{EFF}), EFFICIENCY OF ABSORPTION, ATTENUATION (EFF.), RADIATION HARDNESS (RH), DECAY TIME (τ_d), NEUTRON/γ-RAY DISCRIMINATION (N/γ), AND STABILITY TO ENVIRONMENT (SE), SUCH AS TEMPERATURE, HUMIDITY, ENVIRONMENTAL RADIATION, ADEQUACY FOR DOSE MEASUREMENT (DS), SIZE (SZ), AND COST

			σ_E		
Rb_2CuCl_3 [ar]		crystal	LY	X-, γ-ray	SICCAS [b] [Y. Wu]
$RE_3Al_5O_{12}$:Ce [ag]		ceramic	LY, τ_d	X-ray,γ-ray	UTK [K. Anderson]
51SiO_2-5MgO- 10Al_2O_3- 33Li_2O-0.7Ce_2O_3	GS20	glass small particles [an]	LY τ_d, LY, SP	neutron neutron	STFC [G. Sykora] [b] LANL [B. Wiggins].
SrI_2:Eu		composite (fiber) [v]	Eff., δ		Tohoku U. [K. Kamada]
(TBA)CuX_2 [aq]		crystal	LY	X-, γ-ray	SICCAS[b] [Y. Wu]
$Tb_3Al_5O_{12}$:Ce [w]	TAG:Ce	powder, *also* ceramic, crystal	LY, cost		UoD/UO [J. Indrei]
$Tb_3Al_5O_{12}$:Ce + $Gd_3(Al,Ga)_5O_{12}$:Ce + $Gd_3(Al,Ga)_5O_{12}$:Ce	TbAG:Ce GAAG:Ce GAAG:Ce	thin film thin film crystal (substrate)	DS	X-ray,γ-ray, α, β	UKW [V. Gorbenko]
$TlCaX_3$ [f]		crystal (perovskite)	Z_{eff}, ρ, LY	γ-ray[e]	RMD [E. van Loef]
Tl_2LaCl_5 *also* :Ce/Sr doping	TLC	crystal	LY, σ_E n/γ/p/α SZ, τ_d $Z_{eff.}$	γ-ray, X-ray neutron γ-ray	Kyungpook NU. [H. Kim] [P. Vuong] LBNL [F.Moretti] UC Berkeley [S. Srivastava]
Tl_2LiYCl_6:Ce	TLYC	crystal	LY	γ-ray, neutron	Fisk U. [R. Hawrami] UC Berkeley [S. Srivastava]
$TlMgCl_3$		crystal	Z_{eff}, ρ, LY	γ-ray[e]	RMD [E. van Loef] [b]
$YAlO_3$:Ce	YAP	crystal	τ_d, ρ, LY	X-ray	FZU [M. Nikl] [b]
$YAlO_3$:Yb	YAP	crystal	τ_d	X-ray	Caltech [C. Hu]
$Y_3Al_5O_{12}$:Ce	YAG:Ce	thin film powder crystal aerogel nano-particle	RH [t] LY LY, RH LY, NL τ_d, LY [k] SZ, RH σ_E, LY	X-ray proton, γ-ray X-, γ-ray X-ray HEP β, radio-chemistry	RMD [O. Maksimov] UoD/UO [J. Indrei] [b] U. Giessen [V. Dormenev] LANL/UNM [T. Espinoza] CEA/LNHB [B. Sabot] ENSEMBLE3/ISM NAS Ukraine [O.Sidletskiy] Crytur [S. Sýkorová] U. Lyon [P. Mai]
$Y_3Al_5O_{12}$:Ce + $Lu_3Al_5O_{12}$:Pr + $Lu_3Al_5O_{12}$:Sc	YAG:Ce LuAG:Pr LuAG:Sc	thin film thin film crystal (substrate)	DS	X-ray,γ-ray, α, β	UKW [V. Gorbenko] .
$Y_3Al_5O_{12}$:Pr + $Gd_3Ga_3Al_2O_{12}$:Ce	YAG:Pr GGAG:Ce	ceramic ceramic (layered composite)	τ_d, LY	PET	U. Milano-Bicocca [F. Cova]
$Y_3Al_5O_{12}$:Ce + $Tb_3Al_5O_{12}$:Ce + $Gd_3(Al,Ga)_5O_{12}$:Ce	YAG:Ce TbAG:Ce GAAG:Ce	thin film thin film crystal (substrate)	DS	X-ray,γ-ray, α, β	UKW [V. Gorbenko]
$(Y,Nd,Tb)_3Al_5O_{12}$ [s]		crystal	DS	γ-ray	Tohoku U. [D. Matsukura]
$Y_3Al_5O_{12}$:Ce+	YAG:Ce+	crystal + PhC [m]	LY	X-ray	MIT [C. Roques-Carmes]
$Y_3Al_5O_{12}$:Yb	YAG	crystal	τ_d	X-ray	Caltech [C. Hu]
$(Y_{1/4}Gd_{1/4}Lu_{1/4}X_{1/4})_3$- Al_5O_{12}:Ce [ag]		ceramic	LY, τ_d	X-ray,γ-ray	UTK [K. Anderson]
Y_2O_3 *also* :Ce/Eu doping		nanocrystal crystal	LY, cost		UoD/UO [J. Indrei] [b] ENSEMBLE3/ISM NAS Ukraine

TABLE III

(Continued.) SUMMARY OF SCINTILLATORS AND INTENDED APPLICATIONS BASED ON THE PRESENTATIONS DURING THE SCINT22 CONFERENCE. THE SCINTILLATOR METRICS INCLUDE LY, LINEARITY/NONLINEARITY OF THE LY AS A FUNCTION OF ENERGY DEPOSITION (NL), ENERGY RESOLUTION (σ_E), SINGLE-PHOTON SENSITIVITY (SP), SPATIAL RESOLUTION (δ), SPECTRUM TUNING CAPABILITIES (CL), LIGHT EMISSION ANISOTROPY (EA), HIGH DENSITY (ρ), HIGH *Effective* ATOMIC NUMBER (Z_{EFF}), EFFICIENCY OF ABSORPTION, ATTENUATION (EFF.), RADIATION HARDNESS (RH), DECAY TIME (τ_d), NEUTRON/γ-RAY DISCRIMINATION (N/γ), AND STABILITY TO ENVIRONMENT (SE), SUCH AS TEMPERATURE, HUMIDITY, ENVIRONMENTAL RADIATION, ADEQUACY FOR DOSE MEASUREMENT (DS), SIZE (SZ), AND COST

					[O. Sidletskiy]
$(Y,Sc)_2O_3$		crystal			ENSEMBLE3/ISM NAS Ukraine [O. Sidletskiy]
Y_2SiO_5:Ce	YSO	crystal	τ_d, LY, RH LY, NL	HEP/cal. X-, γ-ray	U. Giessen [V. Dormenev] LANL/UNM [T. Espinoza] ENSEMBLE3/ISM NAS Ukraine [O. Sidletskiy]
ZnO		nano- crystal [ao]	SE,τ_d	PET, HEP X-ray	CTU [b] [V. Čuba]
ZnO:Ga		crystal	τ_d	X-ray	Caltech [C. Hu]
ZnO:X [j]		ceramic	LY, τ_d, RH	heavy ion	GSI [M. Saifulin]
ZnO:Zn		polycrystal	LY	neutron	STFC [G. Sykora] [b]
ZnS		nanoparticles	τ_d	neutron	STFC [S. Mann]
ZnS:Ag		nanoparticles polycrystal	τ_d LY Eff., LY	neutron neutron X-ray	STFC [S. Mann] STFC [G. Sykora] STFC [S. Richards] [b]
$ZnWO_4$		crystal	EA	dark matter	Tohoku U. [S. Kurosawa]
$(Zn,Mg)WO_4$		crystal	EA	dark matter	Tohoku U. [S. Kurosawa]
(Unspecified)	MOF [r]	crystal	LY [r]	Radio- chemistry	CEA [S. Mauree]
(Unspecified)	MOF [r] (Hf-based)	nano- crystal *in* porous composite	LY [r]	Radio- chemistry	U. Milano-Bicocca [M. Orfano]
(Unspecified)	Garnet	nano- crystal [ao]	SE,τ_d	PET, HEP X-ray	CTU [V. Čuba]
(Unspecified)		glass (^{6}Li) doped	SP, τ_d	neutron	LANL [A. Stamatopoulos]
(Unspecified)	Metal oxide (doped)	nano- crystal [ao]	SE,τ_d	PET, HEP X-ray	CTU [V. Čuba]
(Unspecified)	Perovskite	nano- crystal [ao]	SE,τ_d	PET, HEP X-ray	CTU [V. Čuba]
(Unspecified)		photonic crystal [at]	LY, Eff.	 imaging	IIT [O. Segal] [A. Shultzman]
(Unspecified)		photonic crystal [au]	LY, Eff., τ_d	PET	LRS-PORT [D. Kowal]
(Unspecified)	MBS [aw]	plastic	cost, SZ	neutron	SNL [N. Myllenbeck]
(Unspecified)		plastic [ax]	cost, Shape		ORNL [M. Febbraro]
(Unspecified)	OGS [ay]		n/γ	neutron	LANL [J. Perello]

[a] τ_d stands for the scintillator decay time, which could limit detector time resolution, σ_t.
[b] SCINT22 presentation with reference to previous or other people's work.
[c] Gd can be replaced by Y, Lu; Ga can be replaced by Al or a mixture of Ga, Al.
[d] GdX = $Gd_{0.894}RE_{0.100}Ce_{0.006}$, RE = La, Nd, Sm, Gd, Tb, Dy, Ho, Er, Tm, Yb, Y and Lu; GaY = $Ga_{0.4}Al_{0.6}$.
[e] also include high-energy X-rays above 100 keV.
[f] X = Cl, Br, I.
[g] PCCT stands for photon counting computed tomography.
[h] WbLS stands for water-based liquid scintillator.
[i] X = Ce, Eu.
[j] X = Ga, In.
[k] Nonlinearity of LY specifically. LS stands for liquid scintillator.
[l] PPO, or 2,5-Diphenyloxazole is the fluor or luminophor chemical. PTP, POPOP are two other fluor chemicals
[m] PhC stands for photonic crystal nanostructures.
[n] x $\sim$ 0.75.
[o] powder film thickness between 25 to 50 μm.
[p] X = F, T, HR, which symbolizes different formulations and surface states provided by EPIC Crystals.
[q] Gd fraction is about 99%, Ce about 1%, Mg about 0.1%.
[r] MOF stands for metal organic frameworks. LY specifically target radioactive element induced photon counting rate.
[s] Y above 99.7%, Nd about 0.2%, Tb about 0.003%.
[t] RH specifically refers to thermal stability under intense XFEL flux.
[u] SE specifically refers to high temperature nuclear reactor environment.
[v] glass fiber structure (quartz or borosilicate) is used for optical guiding (cladding) of scintillator crystal emission.
[w] *also* with Eu or Gd doping.
[x] Scintillator emission spectrum towards red wavelengths to reduce Rayleigh scattering loss in fiber.
[y] Eljen Technology now recommends EJ-276D over EJ-276. A significant improvement over EJ-276

TABLE III

(Continued.) SUMMARY OF SCINTILLATORS AND INTENDED APPLICATIONS BASED ON THE PRESENTATIONS DURING THE SCINT22 CONFERENCE. THE SCINTILLATOR METRICS INCLUDE LY, LINEARITY/NONLINEARITY OF THE LY AS A FUNCTION OF ENERGY DEPOSITION (NL), ENERGY RESOLUTION (σ_E), SINGLE-PHOTON SENSITIVITY (SP), SPATIAL RESOLUTION (δ), SPECTRUM TUNING CAPABILITIES (CL), LIGHT EMISSION ANISOTROPY (EA), HIGH DENSITY (ρ), HIGH *Effective* ATOMIC NUMBER (Z_{EFF}), EFFICIENCY OF ABSORPTION, ATTENUATION (EFF.), RADIATION HARDNESS (RH), DECAY TIME (τ_d), NEUTRON/γ-RAY DISCRIMINATION (N/γ), AND STABILITY TO ENVIRONMENT (SE), SUCH AS TEMPERATURE, HUMIDITY, ENVIRONMENTAL RADIATION, ADEQUACY FOR DOSE MEASUREMENT (DS), SIZE (SZ), AND COST

in that the "D" version does not turn yellow with the passage of time.
[z] The first author in the Mu2e international collaboration.
[aa] fluorinated version of $CsPbBr_3$. Phoswich configuration.
[ab] LiI with Eu, Sr co-doping. Pure $LaCl_3$.
[ac] unspecified plastic scintillator with PMMA base. Polymer/plastic film made by nano-imprinting for Purcell effect.
[ad] The presenting author in the ATLAS international collaboration.
[ae] absolute light yield (ALY) that takes into account detector QE, system light collection efficiency, etc.
[af] Three layer plastic phoswich. Discrimination of thermal neutrons, fast neutrons, α, β, and γ-rays.
[ag] High-entropy rare earth garnets. RE = $Y_{1/4}Gd_{1/4}Lu_{1/4}X_{1/4}$. X = La, Pr, Nd, Sm, Eu, Tb, Ho, Er, or Yb.
[ah] thin film on commercial ZrO_3:Y substrates. Scintillator film thickness 5-10 μm typically,
[ai] Gd-to-Lu ratio varied from 0 to 1.5. The best LY = 21 kph/MeV had a ratio of 1.
[aj] LS based on a 9-methylcarbazole fluorescent die and linear-alkylbenzene primary fluor.
[ak] 30-40 % wt. difluorenylsilane in poly(styrene) was identified as optimum for scintillation performance and manufacturability.
$\sim$ 5 kg of materials thermally processed into "Nanoguide" fiber-optic bundles, using PMMA as a low refractive index component.
[al] heterostructure may also be called metascintillators or metapixel.
[am] NC imbedded in polystyrene (with different filling factors, up to 10%) and deposited as thin film on a dense scintillator (LYSO, BGO, and GAGG).
[an] glass scintillators imbedded in transparent acrylic matrix.
[ao] Cs_4PbBr_6 nanocrystals with surface stabilized by organic ligands. ZnO nanoparticles covered by silica layer.
[ap] Reported light yield 90 kph/MeV peaked at 385 nm. Rb element shows high natural radioactivity. see also note [ar].
[aq] TBA = tetrabutylammonium cation. X=Cl, Br.
[ar] Low dimensional perovskite-like metal halides such as ternary copper(I) halides were found to have extremely high photoluminescence quantum yields (PLQYs) $\sim$ 90 kph/MeV and large Stokes shift, in addition to photophysical properties and stability.
[as] PWO-II refers to the 2nd generation (current) single crystal PWO for calorimetry.
PWO-III refers to the 3rd generation of PWO for fast timing.
[at] a multi-layered photonic structure, or 1D photonic crystal, made from layers of scintillator and another dielectric.
[au] 2D photonic structures of polymer, plastic, and halide perovskite.
[av] 2D photonic structures of perovskites with LY $>$ 20 kph/MeV, τ_d = 1-15 ns. A = PEA, BA.
X = Pb, Sn, Mn, Cu. Y= Br, I.
[aw] melt-blended scintillators (MBS), produced by dissolving thermoplastic polymers with high performance fluorophores, such as fluorene. MBS's can be produced in one day, as monoliths or continuous filament, and have comparable scintillation performance to conventionally polymerized analogs.
[ax] alternates to polystyrene, PVT that are suitable for 3D printing (rapid cure time $<$ 30 s).
[ay] OGS stands for organic glass scintillator(s).
[az] Radiation environment of the DAMPE satellite with six years of in-orbit data.
[aaa] the temperature dependency on the light output of ceramic Ce:GAGG scintillator wrapped with titanium oxide (TiO2, 100 micron thick) paint reflector.
[aab] x=0.001, 0.002, 0.005, 0.01, 0.02, 0.05, 0.07, 0.1.

the human eyes were the best photodetectors and continue to be enabling for RadIT. In addition to absorption-based X-ray radiography, there are many other RadIT modalities, such as phase contrast X-ray imaging, coherent X-ray diffractive imaging, high-energy X-/γ-ray radiography at above 1 MeV, X-ray CT, proton IT, neutron IT, PET, high-energy electron radiography, muon tomography, and so on. The coexistence of many RadIT modalities opens doors to multimodal RadIT.

More than 160 kinds of scintillators and applications were presented during the SCINT22 conference, as summarized in Table III. Recent work included inorganic and organic scintillator composites or heterostructures, liquid-phase synthesis of perovskites and single-crystal micrometer-thick films, use of multiphysics models, and lately data science to guide scintillator development, structural innovations, such as PhCs, nanostructured scintillators enhanced by the Purcell effect, novel use of existing scintillators through heterostructural innovations (fibers), and multilayer configurations.

Scintillator metrics, such as LY and decay time, are discussed in light of RadIT metrics. RadIT, both photon- and particle-based, continues to aim for finer spatial and temporal resolution, the highest possible efficiency in conjunction with advances in high luminosity X-ray and particle sources, photodetectors, and efficient algorithms for data processing (mostly left out of this article). While X-ray and charged particle IT necessarily require faster, brighter scintillators, and the concerns with radiation damage are growing, neutron IT, on the other hand, is currently limited by the neutron source intensity, and, therefore, high-efficiency scintillators with good spatial, energy resolution (for neutron recoils) would be desired. The scintillator requirements in RadIT overlap significantly with other applications, such as in HEP. For example, the calorimeter applications at FCC at the European Organization for Nuclear Research (CERN), Geneva, Switzerland, or CEPC in China will not only need excellent energy resolution but also new scintillator functions, including fast and precision timing (picosecond, driven by high

luminosity above 10^{34} cm^{-2}/s and corresponding high data rate and large datasets), outstanding radiation tolerance and finer granularity or spatial resolution of the active elements. Dark matter search usually requires a large volume and surface area of scintillators, which overlaps with requirements of RadIT in higher detection efficiencies, large FoV, and up to 4π solid angle signal coverage.

Since there is no universal scintillator that can fit all needs, tradeoffs between, for example, cost and performance, spatial resolution and efficiency, LY and decay time, are often necessary. Optimizing a scintillator for a specific application appears to be the next best option. Scintillator optimization can become a part of the "global" optimization strategy in RadIT applications, which include cradle-to-grave analysis of an ionizing photon or particle. In addition to a growing number of successful empirical approaches, a new approach is an optimization through data science for maximal information yield. For many years, the discovery and design of new scintillator materials relied on laborious, time-consuming, trial-and-error approaches, yielding little physical insight sometimes, and leaving a vast space of potentially revolutionary materials to be explored. A closed-loop machine-learning-driven adaptive design framework based on data from the literature, in-house experiments, and first-principles (quantum mechanical) calculations have recently been demonstrated for fast screening of perovsikites, garnets, and elpasolites. It is possible to extend such a framework to, for example, high entropy scintillators, even though it is well-recognized that computation can become a bottleneck.

Plenty of new opportunities exist that make RadIT and scintillator development mutually beneficial and dependent. Examples include optimization of RadIT performance with reduced radiation dose, data-driven measurements, photon/particle counting and tracking methods supplementing time-integrated measurements, multimodal RadIT, and novel applications of RadIT for scintillator discovery.

Appendix
Scintillator List for SCINT22

Table III summarizes different scintillators presented during the SCINT22 conference and their applications.

Acknowledgment

Zhehui Wang would like to thank the members of the local organizing committee, the International Advisory Committee, the session chairs, the Los Alamos National Laboratory (LANL) Conference Team, Los Alamos, NM, USA, and many others (of course, all the presenters and sponsors, in person or online) for helping with the 16th International Conference on Scintillating Materials & Their Applications (SCINT22), Santa Fe, NM, USA, September 19–23, 2022; especially Etiennette Auffray at CERN, Geneva, Switzerland, Zane Bell at the IEEE TNS, Gregory Bizarri at Cranfield University, Cranfield, U.K., Edith Bourret and Weronika Wolszczak at the Lawrence Berkeley National Laboratory, Berkeley, CA, USA, Bruce Chai at Crystal Photonics, Inc., Sanford, FL, USA, Pieter Dorenbos at the Delft University of Technology, Delft, The Netherlands, Alex Gektin at the National Academy of Sciences of Ukraine, Kyiv, Ukraine, Sarah Haag, Alexei Klimenko, Ross Muenchausen, Wanyi Nie, Bob Reinovsky, Rich Sheffield, Sergei Tretiak, Blas Uberuaga, Sven Vogel, Dmitry Yarotski, and Alex Zubelewicz at LANL, Los Alamos, NM, USA, Luiz Jacobsohn at Clemson University, Clemson, SC, USA, Kai Kamada at Tohoku University, Sendai, Japan, Eva Mihóková and Irena Villa at the Institute of Physics, Czech Academy of Sciences, Prague, Czech Republic, Anna Vedda at the University of Milano-Bicocca, Milan, Italy, Craig Woody at the Brookhaven National Laboratory, Upton, NY, USA, and Liyuan Zhang and Ren-Yuan Zhu at the California Institute of Technology, Pasadena, CA, USA. Ghanshyam Pilania would like to thank discussions with Dr. K. J. McClellan, Dr. C. R. Stanek, and Dr. B. P. Uberuaga at LANL.

References

[1] W. C. Röntgen, "On a new kind of rays," *Nature*, vol. 53, pp. 274–276, Jan. 1896.

[2] V. B. Berestetskii, E. M. Lifshitz, and L. P. Pitaevskii, *Quantum Electrodynamics*. Jordan Hill, Oxford, U.K.: Elsevier, 1971.

[3] C. Dujardin et al., "Needs, trends, and advances in inorganic scintillators," *IEEE Trans. Nucl. Sci.*, vol. 65, no. 8, pp. 1977–1997, Aug. 2018, doi: 10.1109/TNS.2018.2840160.

[4] W. W. Moses, "Current trends in scintillator detectors and materials," *Nucl. Instrum. Methods Phys. Res. A, Accel. Spectrom. Detect. Assoc. Equip.*, vol. 487, nos. 1 and 2, pp. 123–128, Jul. 2002.

[5] M. J. Weber, "Inorganic scintillators: Today and tomorrow," *J. Lumin.*, vol. 100, nos. 1–4, pp. 35–45, Dec. 2002.

[6] M. Nikl and A. Yoshikawa, "Recent R&D trends in inorganic single-crystal scintillator materials for radiation detection," *Adv. Opt. Mater.*, vol. 3, no. 4, pp. 463–481, Apr. 2015, doi: 10.1002/adom.201400571.

[7] T. Yanagida, "Inorganic scintillating materials and scintillation detectors," *Proc. Jpn. Acad., Ser. B*, vol. 94, no. 2, pp. 75–97, 2018.

[8] C. Kim et al., "A review of inorganic scintillation crystals for extreme environments," *Crystals*, vol. 11, no. 6, p. 669, Jun. 2021, doi: 10.3390/cryst11060669.

[9] C. A. Hajivassiliou, "Distribution of plasma turbulence in our Galaxy derived from radio scintillation maps," *Nature*, vol. 355, no. 6357, pp. 232–234, Jan. 1992.

[10] Y. Zhou, J. Chen, O. M. Bakr, and O. F. Mohammed, "Metal halide perovskites for X-ray imaging scintillators and detectors," *ACS Energy Lett.*, vol. 6, no. 2, pp. 739–768, Feb. 2021.

[11] B. Yang et al., "Lead-free halide Rb_2CuBr_3 as sensitive X-ray scintillator," *Adv. Mater.*, vol. 31, no. 44, Nov. 2019, Art. no. 1904711.

[12] V. B. Mykhaylyk, H. Kraus, V. Kapustianyk, H. J. Kim, P. Mercere, M. Rudko, P. Da Silva, O. Antonyak, and M. Dendebera, "Bright and fast scintillations of an inorganic halide perovskite $CsPbBr_3$ crystal at cryogenic temperatures," *Sci. Rep.*, vol. 10, p. 8601, May 2020, doi: 10.1038/s41598-020-65672-z.

[13] A. Snigirev, I. Snigireva, V. Kohn, S. Kuznetsov, and I. Schelokov, "On the possibilities of X-ray phase contrast microimaging by coherent high-energy synchrotron radiation," *Rev. Sci. Instrum.*, vol. 66, no. 12, pp. 5486–5492, Dec. 1995.

[14] S. W. Wilkins, T. E. Gureyev, D. Gao, A. Pogany, and A. W. Stevenson, "Phase-contrast imaging using polychromatic hard X-rays," *Nature*, vol. 384, no. 6607, pp. 335–338, Nov. 1996.

[15] A. Momose, T. Takeda, Y. Itai, and K. Hirano, "Phase-contrast X-ray computed tomography for observing biological soft tissues," *Nature Med.*, vol. 2, no. 4, pp. 473–475, Apr. 1996.

[16] D. Chapman et al., "Diffraction enhanced X-ray imaging," *Phys. Med. Biol.*, vol. 42, no. 11, pp. 2015–2025, Nov. 1997, doi: 10.1088/0031-9155/42/11/001.

[17] B. B. He, U. Preckwinkel, and K. L. Smith, "Fundamentals of two-dimensional X-ray diffraction (XRD^2)," *Adv. X-Ray Anal.*, vol. 43, pp. 273–280, Jan. 2000.

[18] S. O. Hruszkewycz et al., "Quantitative nanoscale imaging of lattice distortions in epitaxial semiconductor heterostructures using nanofocused X-ray Bragg projection ptychography," *Nano Lett.*, vol. 12, no. 10, pp. 5148–5154, Oct. 2012.

[19] J. Miao, T. Ishikawa, I. K. Robinson, and M. M. Murnane, "Beyond crystallography: Diffractive imaging using coherent X-ray light sources," *Science*, vol. 348, no. 6234, pp. 530–535, May 2015.

[20] C. Ekdahl, "Modern electron accelerators for radiography," *IEEE Trans. Plasma Sci.*, vol. 30, no. 1, pp. 254–261, Feb. 2002.

[21] C. Pellegrini and J. Stöhr, "X-ray free electron lasers: Principles, properties and applications," *Nucl. Instrum. Methods Phys. Res. A, Accel. Spectrom. Detect. Assoc. Equip.*, vol. 500, nos. 1–3, pp. 33–40, Mar. 2003. [Online]. Available: https://www-ssrl.slac.stanford.edu/stohr/xfels.pdf

[22] Z. Wang, "Radiographic imaging and tomography," *Appl. Opt.*, vol. 61, no. 6, pp. RDS1–RDS4, 2022.

[23] (2009). *X-Ray Data Booklet*. [Online]. Available: https://xdb.lbl.gov/ and https://physics.nist.gov/PhysRefData/XrayMassCoef/chap2.html

[24] W. G. J. Langeveld, "Effective atomic number, mass attenuation coefficient parameterization, and implications for high-energy X-ray cargo inspection systems," *Phys. Proc.*, vol. 90, pp. 291–304, Dec. 2017.

[25] F. H. Attix, *Introduction to Radiological Physics and Radiation Dosimetry*. Hoboken, NJ, USA: Wiley, 2008.

[26] B. E. Warren, *X-Ray Diffraction*. Reading, MA, USA: Addison-Wesley, 1969.

[27] R. J. Leclair and P. C. Johns, "A semianalytic model to investigate the potential applications of X-ray scatter imaging," *Med. Phys.*, vol. 25, no. 6, pp. 1008–1020, Jun. 1998.

[28] G. Harding, J. Kosanetzky, and U. Neitzel, "X-ray diffraction computed tomography," *Med. Phys.*, vol. 14, no. 4, pp. 515–525, Jul. 1987, doi: 10.1118/1.596063.

[29] A. H. Lumpkin, A. B. Garson, and M. A. Anastasio, "First point-spread function and X-ray phase-contrast imaging results with an 88-mm diameter single crystal," *Rev. Sci. Instrum.*, vol. 89, no. 7, Jul. 2018, Art. no. 073704, doi: 10.1063/1.5027499.

[30] R. J. Adrian, "Dynamic ranges of velocity and spatial resolution of particle image velocimetry," *Meas. Sci. Technol.*, vol. 8, no. 12, pp. 1393–1398, Dec. 1997.

[31] J. C. Dainty and R. Shaw, *Image Science: Principles, Analysis and Evaluation of Photographic-Type Imaging Processes*. New York, NY, USA: Academic Press, 1974.

[32] T. Martin and A. Koch, "Recent developments in X-ray imaging with micrometer spatial resolution," *J. Synchrotron Radiat.*, vol. 13, no. 2, pp. 180–194, Mar. 2006.

[33] S. R. Meikle, P. Kench, M. Kassiou, and R. B. Banati, "Small animal SPECT and its place in the matrix of molecular imaging technologies," *Phys. Med. Biol.*, vol. 50, no. 22, pp. R45–R61, Nov. 2005.

[34] M. R. Howells et al., "An assessment of the resolution limitation due to radiation-damage in X-ray diffraction microscopy," *J. Electron Spectrosc. Rel. Phenomena*, vol. 170, nos. 1–3, pp. 4–12, Mar. 2009.

[35] H. Chen, M. M. Rogalski, and J. N. Anker, "Advances in functional X-ray imaging techniques and contrast agents," *Phys. Chem. Chem. Phys.*, vol. 14, no. 39, pp. 13469–13486, Oct. 2012, doi: 10.1039/c2cp41858d.

[36] S. A. Watson, J. M. Gonzales, C. Gossein, M. D. Hoverson, A. Tubb, and M. D. Ulibarri, "Use of dense, monolithic, scintillator membranes as a high resolution imaging detector for megavolt radiography at U1-A and DARHT," Los Alamos Nat. Lab., Los Alamos, NM, USA, Tech. Rep. LA-UR-99-6491, 1999.

[37] N. M. Winch, S. A. Watson, and J. F. Hunter, "Modeling blur in various detector geometries relevant to DARHT," *Proc. SPIE*, vol. 10132, Mar. 2017, Art. no. 101323U, doi: 10.1117/12.2249110.

[38] N. M. Winch, S. A. Watson, and J. F. Hunter, "Segmented scintillators for megavolt radiography," in *Proc. IEEE Nucl. Sci. Symp. Med. Imag. Conf. Proc. (NSS/MIC)*, Nov. 2018, pp. 1–4, doi: 10.1109/NSS-MIC.2018.8824434.

[39] Z. Wang et al., "Thin scintillators for ultrafast hard X-ray imaging," *Proc. SPIE*, vol. 9504, May 2015, Art. no. 95040N, doi: 10.1117/12.2178420.

[40] F. Yasar, M. Kilin, S. Dehdashti, Z. Yu, Z. Ma, and Z. Wang, "Spatially resolved X-ray detection with photonic crystal scintillators," *J. Appl. Phys.*, vol. 130, no. 4, Jul. 2021, Art. no. 043101.

[41] *CT for Cargo Inspection*. Accessed: Jun. 26, 2023. [Online]. Available: https://www.astrophysicsinc.com/

[42] L. W. Alvarez et al., "Search for hidden chambers in the pyramids," *Science*, vol. 167, no. 3919, pp. 832–839, Feb. 1970.

[43] J. Perry et al., "Imaging a nuclear reactor using cosmic ray muons," *J. Appl. Phys.*, vol. 113, May 2013, Art. no. 184909.

[44] Z. Wang et al., "Billion-pixel X-ray camera (BiPC-X)," *Rev. Sci. Instrum.*, vol. 92, no. 4, Apr. 2021, Art. no. 043708.

[45] Z. Wang, C. L. Morris, J. S. Kapustinsky, K. Kwiatkowski, and S.-N. Luo, "Towards hard X-ray imaging at GHz frame rate," *Rev. Sci. Instrum.*, vol. 83, no. 10, Oct. 2012, Art. no. 10E510.

[46] Z. Wang et al., "Gigahertz (GHz) hard X-ray imaging using fast scintillators," *Proc. SPIE*, vol. 8852, Sep. 2013, Art. no. 88521A, doi: 10.1117/12.2022294.

[47] A. H. Zewail and J. M. Thomas, *4D Electron Microscopy*. London, U.K.: Imperial College Press, 2010.

[48] C. Campbell, X. Tang, Y. Sechrest, K. Fezzaa, Z. Wang, and D. Staack, "Ultrafast X-ray imaging of pulsed plasmas in water," *Phys. Rev. Res.*, vol. 3, no. 2, Jun. 2021, Art. no. L022021.

[49] A. Rose, *Vision: Human and Electronic*. Cham, Switzerland: Springer, 2012.

[50] A. E. Burgess, "The Rose model, revisited," *J. Opt. Soc. Amer. A, Opt. Image Sci.*, vol. 16, no. 3, pp. 633–646, Mar. 1999.

[51] A. Rose, "A unified approach to the performance of photographic film, television pickup tubes, and the human eye," *J. Soc. Motion Picture Eng.*, vol. 47, no. 4, pp. 273–294, Oct. 1946.

[52] K. M. Hanson, "A simplified method of estimating noise power spectra," *Proc. SPIE*, vol. 3336, pp. 243–250, Jul. 1998.

[53] J. J. Ma, S. Masoodian, D. A. Starkey, and E. R. Fossum, "Photon-number-resolving megapixel image sensor at room temperature without avalanche gain," *Optica*, vol. 4, no. 12, pp. 1474–1481, 2017.

[54] K. O. Plaud-Ramos et al., "A study of CR-39 plastic charged-particle detector replacement by consumer imaging sensors," *Rev. Sci. Instrum.*, vol. 87, no. 11, Nov. 2016, Art. no. 11E706.

[55] K. Kuk, C. Cude-Woods, and C. R. Chavez, "Projection imaging with ultracold neutrons," *Nucl. Instrum. Methods Phys. Res. A, Accel. Spectrom. Detect. Assoc. Equip.*, vol. 1003, Jul. 2021, Art. no. 165306.

[56] *Geant4 Website*. Accessed: Mar. 3, 2023. [Online]. Available: https://geant4.web.cern.ch/

[57] Geant4 Requires the Light Emitting Properties of a Scintillator to be Known and Provided to the Simulation by the User or Application Developer. In the Most Recent Versions, Standard Examples of Optical Properties are Provided in the Geant4 Data Library, but These do not Remove the Need to Explicitly State Which Optical Properties Including Scintillation Behaviour Apply to Which Material. (Credit: An Anonymous Reviewer), 2023.

[58] *MCNP Website*. Accessed: Jun. 26, 2023. [Online]. Available: https://mcnp.lanl.gov/

[59] A. Knapitsch and P. Lecoq, "Review on photonic crystal coatings for scintillators," *Int. J. Modern Phys. A*, vol. 29, no. 30, Dec. 2014, Art. no. 1430070.

[60] Y. Kurman, A. Shultzman, O. Segal, A. Pick, and I. Kaminer, "Photonic-crystal scintillators: Molding the flow of light to enhance X-ray and γ-ray detection," *Phys. Rev. Lett.*, vol. 125, no. 4, Jul. 2020, Art. no. 040801.

[61] C. Roques-Carmes et al., "A framework for scintillation in nanophotonics," *Science*, vol. 375, no. 6583, Feb. 2022, Art. no. eabm9293.

[62] M. Kronberger, E. Auffray, and P. Lecoq, "Probing the concepts of photonic crystals on scintillating materials," *IEEE Trans. Nucl. Sci.*, vol. 55, no. 3, pp. 1102–1106, Jun. 2008.

[63] E. M. Purcell, "Spontaneous emission probabilities at radio-frequencies," *Phys. Rev.*, vol. 69, p. 681, Jun. 1946.

[64] C. Silvestre, "Light management in scintillating materials," Ph.D. thesis, Dept. Eng. Sci., Université de Technologie de Troyes, Troyes, France, 2019.

[65] Z. He, W. Li, G. F. Knoll, D. K. Wehe, J. Berry, and C. M. Stahle, "3-D position sensitive CdZnTe gamma-ray spectrometers," *Nucl. Instrum. Methods Phys. Res. A, Accel. Spectrom. Detect. Assoc. Equip.*, vol. 422, nos. 1–3, pp. 173–178, Feb. 1999.

[66] D. Budnitsky et al., "Chromium-compensated GaAs detector material and sensors," *J. Instrum.*, vol. 9, no. 7, Jul. 2014, Art. no. C07011.

[67] A. Dragone et al., "Feasibility study of a '4H' X-ray camera based on GaAs:Cr sensor," *J. Instrum.*, vol. 11, Nov. 2016, Art. no. C11042.

[68] K. S. Shanks et al., "The MM-PAD-2.1: A wide-dynamic-range detector for high-energy X-ray imaging," in *Proc. IEEE Nucl. Sci. Symp. Med. Imag. Conf. (NSS/MIC)*, Oct./Nov. 2020, pp. 1–2, doi: 10.1109/NSS/MIC42677.2020.9507923.

[69] C. Hu et al., "Hadron-induced radiation damage in fast heavy inorganic scintillators," *Instruments*, vol. 6, no. 4, p. 57, Oct. 2022.

[70] Q. Lyu, R. Neph, and K. Sheng, "Tomographic detection of photon pairs produced from high-energy X-rays for the monitoring of radiotherapy dosing," *Nature Biomed. Eng.*, vol. 7, no. 3, pp. 323–334, Oct. 2022, doi: 10.1038/s41551-022-00953-8.

[71] M. E. Rutherford, D. J. Chapman, T. G. White, M. Drakopoulos, A. Rack, and D. E. Eakins, "Evaluating scintillator performance in time-resolved X-ray studies at synchrotron light sources," *J. Synchrotron Rad.*, vol. 23, pp. 685–693, Feb. 2016.

[72] T. Martin et al., "LSO-based single crystal film scintillator for synchrotron-based hard X-ray micro-imaging," *IEEE Trans. Nucl. Sci.*, vol. 56, no. 3, pp. 1412–1418, Jun. 2009.

[73] X. Wu, Z. Guo, and S. Zhu, "Ultrathin, transparent, and high density perovskite scintillator film for high resolution X-ray microscopic imaging," *Adv. Sci.*, vol. 9, Jun. 2022, Art. no. 2200831.

[74] Y. Hormozan, I. Sychugov, and J. Linnros, "High resolution X-ray imaging using a structured scintillator," *Med. Phys.*, vol. 43, no. 2, pp. 696–701, Feb. 2016.

[75] V. V. Nagarkar, T. K. Gupta, S. R. Miller, Y. Klugerman, M. R. Squillante, and G. Entine, "Structured CsI(Tl) scintillators for X-ray imaging applications," *IEEE Trans. Nucl. Sci.*, vol. 45, no. 3, pp. 492–496, Jun. 1998.

[76] W. Ye, G. Bizarri, M. D. Birowosuto, and L. J. Wong, "Enhancing large-area scintillator detection with photonic crystal cavities," *ACS Photon.*, vol. 9, no. 12, pp. 3917–3925, Dec. 2022.

[77] Z. Lin, S. Lv, Z. Yang, J. Qiu, and S. Zhou, "Structured scintillators for efficient radiation detection," *Adv. Sci.*, vol. 9, no. 2, Jan. 2022, Art. no. 2102439, doi: 10.1002/advs.202102439.

[78] H. F. Poulsen, *Three-Dimensional X-Ray Diffraction Microscopy: Mapping Polycrystals and Their Dynamics*, vol. 205. Cham, Switzerland: Springer, 2004.

[79] R. Pokharel, "Overview of high-energy X-ray diffraction microscopy (HEDM) for mesoscale material characterization in three-dimensions," in *Materials Discovery and Design*. Cham, Switzerland: Springer, 2018, pp. 167–201.

[80] R. Pokharel et al., "In-situ observation of bulk 3D grain evolution during plastic deformation in polycrystalline Cu," *Int. J. Plasticity*, vol. 67, pp. 217–234, Apr. 2015.

[81] J. V. Bernier, R. M. Suter, A. D. Rollett, and J. D. Almer, "High-energy X-ray diffraction microscopy in materials science," *Annu. Rev. Mater. Res.*, vol. 50, pp. 395–436, 2020.

[82] H. Toda, "Applied imaging methods," in *X-Ray CT: Hardware and Software Techniques*. Singapore: Springer, 2021, pp. 267–332.

[83] H. F. Poulsen et al., "4D characterization of metals by 3DXRD," in *Proc. 31st Risø Int. Symp. Mater. Sci.*, vol. 31, 2010, pp. 101–119.

[84] R. Pokharel et al., "Non-destructive characterization of UO_{2+x} nuclear fuels," *Microsc. Today*, vol. 25, no. 6, pp. 42–47, Nov. 2017.

[85] P. Dorenbos, "Fundamental limitations in the performance of Ce^{3+}, Pr^{3+}, and Eu^{3+}-activated scintillators," *IEEE Trans. Nucl. Sci.*, vol. 57, no. 3, pp. 1162–1167, Jun. 2010.

[86] M. Kutsal, H. F. Poulsen, G. Winther, H. O. Sørensen, and C. Detlefs, "High-resolution 3D X-ray diffraction microscopy: 3D mapping of deformed metal microstructures," *J. Appl. Crystallogr.*, vol. 55, no. 5, pp. 1125–1138, Oct. 2022.

[87] F. Pfeiffer, "X-ray ptychography," *Nature Photon.*, vol. 12, pp. 9–17, Jan. 2018.

[88] S. Maddali, J.-S. Park, and H. Sharma, "High-energy coherent X-ray diffraction microscopy of polycrystal grains: Steps toward a multiscale approach," *Phys. Rev. Appl.*, vol. 14, Aug. 2020, Art. no. 024085.

[89] T. Zhou, H. Wang, and T. Connolley, "Development of an X-ray imaging system to prevent scintillator degradation for white synchrotron radiation," *J. Synchrotron Radiat.*, vol. 25, pp. 801–807, May 2018.

[90] I. V. Khodyuk and P. Dorenbos, "Nonproportional response of $LaBr_3$:Ce and $LaCl_3$:Ce scintillators to synchrotron X-ray irradiation," *J. Phys., Condens. Matter*, vol. 22, Nov. 2010, Art. no. 485402.

[91] S. A. Watson, "The DARHT camera," *Los Alamos Sci.*, vol. 28, pp. 92–95, Nov. 2003.

[92] O. H. Nestor and C. Y. Huang, "Bismuth germanate: A high-Z gamma-ray and charged particle detector," *IEEE Trans. Nucl. Sci.*, vol. NS-22, no. 1, pp. 68–71, Feb. 1975, doi: 10.1109/TNS.1975.4327617.

[93] C. L. Melcher and J. S. Schweitzer, "Cerium-doped lutetium oxyorthosilicate: A fast, efficient new scintillator," *IEEE Trans. Nucl. Sci.*, vol. 39, no. 4, pp. 502–505, Aug. 1992.

[94] P. J. Blower, "A nuclear chocolate box: The periodic table of nuclear medicine," *Dalton Trans.*, vol. 44, no. 11, pp. 4819–4844, Mar. 2015, doi: 10.1039/c4dt02846e.

[95] Saint Gobain. *LYSO Scintillation Crystal*. Accessed: Oct. 25, 2022. [Online]. Available: https://www.crystals.saint-gobain.com/radiation-detection-scintillators/crystal-scintillators

[96] N. J. Cherepy et al., "Performance of europium-doped strontium iodide, transparent ceramics and bismuth-loaded polymer scintillators," *Proc. SPIE*, vol. 8142, Sep. 2011, Art. no. 81420W, doi: 10.1117/12.896656.

[97] S. A. Vasile et al., "Cost-effective segmented scintillating converters for hard X-rays," *Proc. SPIE*, vol. 2859, Jul. 1996, Art. no. 245127, doi: 10.1117/12.245127.

[98] S. A. Watson et al., "Design, fabrication and testing of a large anti-scatter grid for megavolt γ-ray imaging," in *Proc. IEEE Nucl. Sci. Symp. Conf. Rec.*, Oct. 2005, pp. 717–721.

[99] N. J. Cherepy et al., "Transparent ceramic scintillators for gamma spectroscopy and MeV imaging," *Proc. SPIE*, vol. 9593, Sep. 2015, Art. no. 95930P, doi: 10.1117/12.2189156.

[100] Z. Seeley, N. Cherepy, and S. Payne, "Two-step sintering of $Gd_{0.3}Lu_{1.6}Eu_{0.1}O_3$ transparent ceramic scintillator," *Opt. Mater. Exp.*, vol. 3, pp. 908–912, Jul. 2013.

[101] N. J. Cherepy, "Lens-coupled MeV X-radiography and CT with transparent ceramic GLO scintillators," *Proc. SPIE*, vol. 11838, Sep. 2021, Art. no. 118380P.

[102] G. Barnea et al., "Use of storage phosphor imaging plates in portal imaging and high-energy radiography: The intensifying effect of metallic screens on the sensitivity," *Med. Phys.*, vol. 18, no. 3, pp. 432–438, May 1991.

[103] D. A. Jaffray, J. J. Battista, A. Fenster, and P. Munro, "X-ray scatter in megavoltage transmission radiography: Physical characteristics and influence on image quality," *Med. Phys.*, vol. 21, no. 1, pp. 45–60, Jan. 1994.

[104] C. Kausch, B. Schreiber, F. Kreuder, R. Schmidt, and O. Dössel, "Monte Carlo simulations of the imaging performance of metal plate/phosphor screens used in radiotherapy," *Med. Phys.*, vol. 26, no. 10, pp. 2113–2124, Oct. 1999.

[105] P. Munro and D. C. Bouius, "X-ray quantum limited portal imaging using amorphous silicon flat-panel arrays," *Med. Phys.*, vol. 25, no. 5, pp. 689–702, May 1998.

[106] M. J. George, K. H. Mueller, and R. H. O'Connor, "Monte-Carlo calculations of high-energy photon energy deposited in a film pack," Los Alamos Nat. Lab., Los Alamos, NM, USA, Tech. Rep. LA-UR-93-2836, 1993.

[107] E. H. Lehmann and D. Ridikas, "Status of neutron imaging—Activities in a worldwide context," *Phys. Proc.*, vol. 69, pp. 10–17, Dec. 2015.

[108] R. Nelson et al., "Neutron imaging at LANSCE—From cold to ultrafast," *J. Imag.*, vol. 4, no. 2, p. 45, Feb. 2018.

[109] I. A. Zaliznyak and S. H. Lee, "Magnetic neutron scattering," Brookhaven Nat. Lab., Upton, NY, USA, Tech. Rep. BNL-73134-2004-BC, 2004.

[110] A. M. Koehler, "Proton radiography," *Science*, vol. 160, no. 3825, pp. 303–304, Apr. 1968.

[111] K. Hanson and U. Schneider, "History of proton radiography and tomography," *Zeitschrift Med. Phys.*, vol. 32, no. 1, pp. 2–4, Feb. 2022.

[112] M. Martišíková, T. Gehrke, S. Berke, G. Aricò, and O. Jäkel, "Helium ion beam imaging for image guided ion radiotherapy," *Radiat. Oncol.*, vol. 13, p. 109, Jun. 2018.

[113] F. G. Sommer et al., "Heavy-ion radiography: Density resolution and specimen radiography," *Investigative Radiol.*, vol. 13, no. 2, pp. 163–170, Mar. 1978.

[114] K. Parodi, "Heavy ion radiography and tomography," *Phys. Medica*, vol. 30, pp. 539–543, Mar. 2014.

[115] J. A. Cookson, "Radiography with protons," *Die Naturwissenschaften*, vol. 61, no. 5, pp. 184–191, May 1974.

[116] G. Poludniowski, N. M. Allinson, and P. M. Evans, "Proton radiography and tomography with application to proton therapy," *Brit. J. Radiol.*, vol. 88, no. 1053, Sep. 2015, Art. no. 20150134.

[117] C. L. Morris et al., "Charged particle radiography," *Rep. Prog. Phys.*, vol. 76, no. 4, Mar. 2013, Art. no. 046301.

[118] N. King et al., "An 800-MeV proton radiography facility for dynamic experiments," *Nucl. Instrum. Methods Phys. Res. A, Accel. Spectrom. Detect. Assoc. Equip.*, vol. 424, no. 1, pp. 84–91, Nov. 1999.

[119] D. Varentsov et al., "Commissioning of the PRIOR proton microscope," *Rev. Sci. Instrum.*, vol. 87, no. 2, Feb. 2016, Art. no. 023303.

[120] C. Morris et al., "Flash radiography with 24 GeV/c protons," *J. Appl. Phys.*, vol. 109, no. 10, May 2011, Art. no. 104905.

[121] C. T. Mottershead and J. D. Zumbro, "Magnetic optics for proton radiography," in *Proc. Part. Accel. Conf.*, May 1997, pp. 1397–1399.

[122] F. E. Merrill et al., "Magnifying lens for 800 MeV proton radiography," *Rev. Sci. Instrum.*, vol. 82, no. 10, Oct. 2011, Art. no. 103709.

[123] K. M. Hanson et al., "Proton computed tomography of human specimens," *Phys. Med. Biol.*, vol. 27, no. 1, pp. 25–36, Jan. 1982.

[124] D. Lo Presti et al., "Design and characterisation of a real time proton and carbon ion radiography system based on scintillating optical fibres," *Phys. Medica*, vol. 32, no. 9, pp. 1124–1134, Sep. 2016.

[125] J. A. Briz et al., "Proton radiographs using position-sensitive silicon detectors and high-resolution scintillators," *IEEE Trans. Nucl. Sci.*, vol. 69, no. 4, pp. 696–702, Apr. 2022.

[126] H. Tang, B. K. Russell, A. Maksimchuk, P. T. Campbell, M. J.-E. Manuel, and L. Willingale, "Scintillator detector characterization for laser-driven proton beam imaging," *Rev. Sci. Instrum.*, vol. 91, no. 12, Dec. 2020, Art. no. 123304.

[127] C. L. Morris et al., "New developments in proton radiography at the Los Alamos Neutron Science Center (LANSCE)," *Exp. Mech.*, vol. 56, no. 1, pp. 111–120, Jan. 2016.

[128] M. S. Freeman et al., "Inverse-collimated proton radiography for imaging thin materials," *Rev. Sci. Instrum.*, vol. 88, no. 1, Jan. 2017, Art. no. 013709.

[129] M. S. Freeman et al., "Dark field proton radiography," *Appl. Phys. Lett.*, vol. 117, no. 14, Oct. 2020, Art. no. 144103.

[130] W. A. Worstell et al., "First results developing time-of-flight proton radiography for proton therapy applications," *Proc. SPIE*, vol. 10948, Mar. 2019, Art. no. 109480G.

[131] J. Addido, "A novel technique to irradiate surgical scars using dynamic electron arc radiotherapy," M.S. thesis, Dept. Med. Phys. Program, Duke Kunshan Univ. Duke Univ., Durham, NC, USA, 2017.

[132] F. Merrill et al., "Electron radiography," *Nucl. Instrum. Methods Phys. Res. B, Beam Interact. Mater. At.*, vol. 261, pp. 382–386, Aug. 2007.

[133] F. Merrill et al., "Demonstration of transmission high energy electron microscopy," *Appl. Phys. Lett.*, vol. 112, no. 14, 2018, Art. no. 144103.

[134] J. L. Shaw, "Microcoulomb ($0.7 \pm \frac{0.4}{0.2}$ μC) laser plasma accelerator on OMEGA EP," *Sci. Rep.*, vol. 11, p. 7498, Apr. 2021.

[135] C. M. Scoby, R. K. Li, E. Threlkeld, H. To, and P. Musumeci, "Single-shot 35 fs temporal resolution electron shadowgraphy," *Appl. Phys. Lett.*, vol. 102, no. 2, Jan. 2013, Art. no. 023506.

[136] G. Bruhaug et al., "Single-shot electron radiography using a laser-plasma accelerator," 2022, *arXiv:2209.14944*.

[137] C. W. Barnes, "Technology risk mitigation research and development for the matter-radiation interactions in extremes (MaRIE) project," *AIP Conf. Proc.*, vol. 1979, no. 1, 2018, Art. no. 160003.

[138] C. W. E. van Eijk, "Radiation detector developments in medical applications: Inorganic scintillators in positron emission tomography," *Radiat. Protection Dosimetry*, vol. 129, nos. 1–3, pp. 13–21, 2008, doi: 10.1093/rpd/ncn043.

[139] P. Lecoq, C. Morel, and J. Prior, "Roadmap toward the 10 ps time-of-flight PET challenge," *Phys. Med. Biol.*, vol. 65, no. 21, Oct. 2020, Art. no. 21RM01, doi: 10.1088/1361-6560/ab9500. [Online]. Available: https://the10pschallenge.org

[140] M. E. Casey and D. R. Osborne, "Siemens biograh vision," in *Advances in PET*, J. Zhang and M. Knopp, Eds. Cham, Switzerland: Springer, 2020.

[141] M. Nikl et al., "Modification of $PbWO_4$ scintillator characteristics by doping," *J. Cryst. Growth*, vol. 229, nos. 1–4, pp. 312–315, Jul. 2001.

[142] M. A. Spurrier et al., "Effects of Ca^{2+} co-doping on the scintillation properties of LSO:Ce," *IEEE Trans. Nucl. Sci.*, vol. 55, no. 3, pp. 1178–1182, Jul. 2008.

[143] M. Nikl et al., "Defect engineering in Ce-doped aluminum garnet single crystal scintillators," *Crystal Growth Des.*, vol. 14, no. 9, pp. 4827–4833, Sep. 2014.

[144] S. Gundacker, E. Auffray, K. Pauwels, and P. Lecoq, "Measurement of intrinsic rise times for various L(Y)SO and LuAG scintillators with a general study of prompt photons to achieve 10 ps in TOF-PET," *Phys. Med. Biol.*, vol. 61, no. 7, pp. 2802–2837, Apr. 2016.

[145] N. Kratochwil, S. Gundacker, P. Lecoq, and E. Auffray, "Pushing Cherenkov PET with BGO via coincidence time resolution classification and correction," *Phys. Med. Biol.*, vol. 65, no. 11, Jun. 2020, Art. no. 115004.

[146] P. Lecoq, "Metamaterials for novel X- or γ-ray detector designs," in *Proc. IEEE Nucl. Sci. Symp. Conf. Rec.*, Oct. 2008, pp. 680–684.

[147] R. M. Turtos, S. Gundacker, E. Auffray, and P. Lecoq, "Towards a metamaterial approach for fast timing in PET: Experimental proof-of-concept," *Phys. Med. Biol.*, vol. 64, no. 18, Sep. 2019, Art. no. 185018, doi: 10.1088/1361-6560/ab18b3.

[148] G. Konstantinou et al., "A proof-of-concept of cross-luminescent metascintillators: Testing results on a BGO:BaF_2 metapixel," *Phys. Med. Biol.* vol. 68, Jan. 2023, Art. no. 025018.

[149] F. Pagano, N. Kratochwil, M. Salomoni, M. Pizzichemi, M. Paganoni, and E. Auffray, "Advances in heterostructured scintillators: Toward a new generation of detectors for TOF-PET," *Phys. Med. Biol.*, vol. 67, no. 13, Jul. 2022, Art. no. 135010, doi: 10.1088/1361-6560/ac72ee.

[150] P. Lecoq et al., "Metascintillators: New results for TOF-PET applications," *IEEE Trans. Radiat. Plasma Med. Sci.*, vol. 6, no. 5, pp. 510–516, May 2022.

[151] G. Konstantinou et al., "Metascintillator pulse shape analysis for optimizing energy and timing measurements," in *Proc. TRPMS*, Oct. 2022, pp. 1–8.

[152] G. Konstantinou et al., "Metascintillator pulse feature and shape analysis to detect photoelectric interactions and energy sharing," in *Proc. IEEE Nuclear Sci. Symp. Med. Imag. Conf. (NSS/MIC)*, Sep. 2021, pp. 1–4.

[153] R. M. Turtos et al., "Timing performance of ZnO:Ga nanopowder composite scintillators," *Phys. Status Solidi (RRL) Rapid Res. Lett.*, vol. 10, no. 11, pp. 843–847, Nov. 2016, doi: 10.1002/pssr.201600288..

[154] R. M. Turtos et al., "Ultrafast emission from colloidal nanocrystals under pulsed X-ray excitation," *J. Instrum.*, vol. 11, Oct. 2016, Art. no. P10015, doi: 10.1088/1748-0221/11/10/P10015.

[155] A. Polovitsyn et al., "Synthesis of air-stable CdSe/ZnS core-shell nanoplatelets with tunable emission wavelength," *Chem. Mater.*, vol. 29, no. 13, pp. 5671–5680, Jun. 2017.

[156] H. Burešová et al., "Preparation and luminescence properties of ZnO:Ga—Polystyrene composite scintillator," *Opt. Exp.*, vol. 24, no. 14, Jul. 2016, Art. no. 15289.

[157] K. Decka et al., "Scintillation response enhancement in nanocrystalline lead halide perovskite thin films on scintillating wafers," *Nanomaterials*, vol. 12, no. 1, p. 14, 2022.

[158] T. Hubácek et al., "Advancement toward ultra-thick and bright InGaN/GaN structures with a high number of QWs," *CrystEngComm*, vol. 21, no. 2, pp. 356–362, 2019.

[159] K. Decká et al., "Timing performance of lead halide perovskite nanoscintillators embedded in a polystyrene matrix," *J. Mater. Chem. C*, vol. 10, Sep. 2022, Art. no. 12836, doi: 10.1039/D2TC02060B.

[160] J. Perego et al., "Highly luminescent scintillating hetero-ligand MOF nanocrystals with engineered Stokes shift for photonic applications," *Nature Commun.*, vol. 13, no. 1, p. 3504, Jun. 2022.

[161] M. Salomoni, R. Pots, E. Auffray, and P. Lecoq, "Enhancing light extraction of inorganic scintillators using photonic crystals," *Crystals*, vol. 8, no. 2, p. 78, Feb. 2018, doi: 10.3390/cryst8020078.

[162] L. Wang, B. Nelson, and Y. M Yang, "WE-DE-BRA-11: A study of motion tracking accuracy of robotic radiosurgery using a novel CCD camera based end-to-end test system," *Med. Phys.*, vol. 43, p. 3814, Jun. 2016.

[163] J. D. Snyder, R. J. Sullivan, X. Wu, E. L. Covington, and R. A. Popple, "Use of a plastic scintillator detector for patient-specific quality assurance of VMAT SRS," *J. Appl. Clin. Med. Phys.*, vol. 20, no. 9, pp. 143–148, Sep. 2019.

[164] A. S. Beddar, "Water equivalent plastic scintillation detectors in radiation therapy," *Radiat Prot Dosimetry*, vol. 120, nos. 1–4, pp. 1–6, 2006.

[165] C. D. Darne, D. G. Robertson, F. Alsanea, C.-A. Collins-Fekete, and S. Beddar, "A novel proton-integrating radiography system design using a monolithic scintillator detector: Experimental studies," *Nucl. Instrum. Methods Phys. Res. A, Accel. Spectrom. Detect. Assoc. Equip.*, vol. 1027, Mar. 2022, Art. no. 166077.

[166] D. Robertson, D. Mirkovic, N. Sahoo, and S. Beddar, "Quenching correction for volumetric scintillation dosimetry of proton beams," *Phys. Med. Biol.*, vol. 58, no. 2, pp. 261–273, 2013.

[167] A. S. Beddar, T. R. Mackie, and F. H. Attix, "Water-equivalent plastic scintillation detectors for high-energy beam dosimetry: I. Physical characteristics and theoretical considerations," *Phys. Med. Biol.*, vol. 37, no. 10, pp. 1883–1900, Oct. 1992.

[168] A. S. Beddar, T. R. Mackie, and F. H. Attix, "Water-equivalent plastic scintillation detectors for high-energy beam dosimetry: II. Properties and measurements," *Phys. Med. Biol.*, vol. 37, no. 10, pp. 1901–1913, Oct. 1992.

[169] A. R. Beierholm, C. F. Behrens, and C. E. Andersen, "Dosimetric characterization of the Exradin W1 plastic scintillator detector through comparison with an in-house developed scintillator system," *Radiat. Meas.*, vol. 69, pp. 50–56, Oct. 2014.

[170] F. Lacroix et al., "Extraction of depth-dependent perturbation factors for parallel-plate chambers in electron beams using a plastic scintillation detector: Extraction of perturbation factors for parallel-plate chambers," *Med. Phys.*, vol. 37, no. 8, pp. 4331–4342, Jul. 2010.

[171] C. C. Cowles et al., "Temperature-dependent properties of BC-412 polyvinyl toluene scintillator," *IEEE Trans. Nucl. Sci.*, vol. 69, no. 4, pp. 942–951, Apr. 2022.

[172] L. Wootton and S. Beddar, "Temperature dependence of BCF plastic scintillation detectors," *Phys. Med. Biol.*, vol. 58, no. 9, pp. 2955–2967, 2013.

[173] J. M. Fontbonne et al., "Scintillating fiber dosimeter for radiation therapy accelerator," *IEEE Trans. Nucl. Sci.*, vol. 49, no. 5, pp. 2223–2227, Oct. 2002.

[174] G. Kertzscher and S. Beddar, "Inorganic scintillation detectors for (192)Ir brachytherapy," *Phys. Med. Biol.*, vol. 64, no. 22, 2019, Art. no. 225018.

[175] D. Robertson, C. Hui, L. Archambault, R. Mohan, and S. Beddar, "Optical artefact characterization and correction in volumetric scintillation dosimetry," *Phys. Med. Biol.*, vol. 59, no. 1, pp. 23–42, Jan. 2014.

[176] T. S. A. Underwood, B. C. Rowland, R. Ferrand, and L. Vieillevigne, "Application of the Exradin W1 scintillator to determine Ediode 60017 and microDiamond 60019 correction factors for relative dosimetry within small MV and FFF fields," *Phys. Med. Biol.*, vol. 60, no. 17, pp. 6669–6683, Sep. 2015.

[177] J. Morin et al., "A comparative study of small field total scatter factors and dose profiles using plastic scintillation detectors and other stereotactic dosimeters: The case of the CyberKnife: CyberKnife measurements with multiple detectors," *Med. Phys.*, vol. 40, no. 1, Jan. 2013, Art. no. 011719.

[178] F. Therriault-Proulx, S. Beddar, and L. Beaulieu, "On the use of a single-fiber multipoint plastic scintillation detector for 192 Ir high-dose-rate brachytherapy: Single-fiber multipoint PSD for HDR brachytherapy," *Med. Phys.*, vol. 40, no. 6-Part1, May 2013, Art. no. 062101.

[179] B. Arjomandy et al., "AAPM task group 224: Comprehensive proton therapy machine quality assurance," *Med. Phys.*, vol. 46, no. 8, pp. e678–e705, 2019.

[180] J. Shen et al., "A novel and fast method for proton range verification using a step wedge and 2D scintillator," *Med. Phys.*, vol. 44, no. 9, pp. 4409–4414, Sep. 2017.

[181] W. Deng et al., "Technical note: Using dual step wedge and 2D scintillator to achieve highly precise and robust proton range quality assurance," *Med. Phys.*, vol. 45, no. 7, pp. 2947–2951, 2018.

[182] W. Cai, H. Oesten, B. Clasie, B. Winey, and K.-W. Jee, "Semi-automated IGRT QA using a cone-shaped scintillator screen detector for proton pencil beam scanning treatments," *Phys. Med. Biol.*, vol. 64, no. 8, Apr. 2019, Art. no. 085004.

[183] S. Russo et al., "Characterization of a commercial scintillation detector for 2-D dosimetry in scanned proton and carbon ion beams," *Phys. Medica*, vol. 34, pp. 48–54, Feb. 2017.

[184] L. Placidi, M. Togno, D. C. Weber, A. J. Lomax, and J. Hrbacek, "Range resolution and reproducibility of a dedicated phantom for proton PBS daily quality assurance," *Zeitschrift Für Medizinische Physik*, vol. 28, no. 4, pp. 310–317, Dec. 2018.

[185] W. Deng, Y. Yang, and C. Liu, "A critical review of let-based intensity-modulated proton therapy plan evaluation and optimization for head and neck cancer management," *Int. J. Part. Therapy*, vol. 8, no. 1, pp. 36–49, 2021.

[186] J. B. Birks, "Scintillation efficiency of anthracene crystals," *Proc. Phys. Soc. Sect. A*, vol. 63, no. 11, pp. 1294–1295, 1950.

[187] L. L. W. Wang, L. A. Perles, L. Archambault, N. Sahoo, D. Mirkovic, and S. Beddar, "Determination of the quenching correction factors for plastic scintillation detectors in therapeutic high-energy proton beams," *Phys. Med. Biol.*, vol. 57, no. 23, pp. 7767–7781, Dec. 2012.

[188] A. S. Tremsin et al., "In situ diagnostics of the crystal-growth process through neutron imaging: Application to scintillators," *J. Appl. Crystallogr.*, vol. 49, no. 3, pp. 743–755, Jun. 2016.

[189] A. S. Tremsin et al., "Real-time crystal growth visualization and quantification by energy-resolved neutron imaging," *Sci. Rep.*, vol. 7, no. 1, Apr. 2017.

[190] A. S. Tremsin et al., "In-situ observation of phase separation during growth of $Cs_2LiLaBr_6$:Ce crystals using energy-resolved neutron imaging," *Crystal Growth Des.*, vol. 17, no. 12, pp. 6372–6381, Dec. 2017.

[191] D. R. Onken et al., "Crystal structure evolution of BaBrCl and BaBrCl:5%Eu up to 1073 K by neutron diffraction," *J. Appl. Crystallogr.*, vol. 51, no. 2, pp. 498–504, Apr. 2018.

[192] A. S. Tremsin et al., "*In-situ* observation and analysis of solid-state diffusion and liquid migration in a crystal growth system: A segregation-driven diffusion couple," *Acta Mater.*, vol. 186, pp. 434–442, Mar. 2020.

[193] A. S. Tremsin and J. V. Vallerga, "Unique capabilities and applications of microchannel plate (MCP) detectors with Medipix/Timepix readout," *Radiat. Meas.*, vol. 130, Jan. 2020, Art. no. 106228.

[194] T. Kai et al., "Visibility estimation for neutron resonance absorption radiography using a pulsed neutron source," *Phys. Procedia*, vol. 43, pp. 111–120, 2013.

[195] A. S. Tremsin et al., "Neutron resonance transmission spectroscopy with high spatial and energy resolution at the J-PARC pulsed neutron source," *Nucl. Instrum. Methods Phys. Res. A, Accel. Spectrom. Detect. Assoc. Equip.*, vol. 746, pp. 47–58, May 2014.

[196] A. S. Tremsin, J. Rakovan, T. Shinohara, W. Kockelmann, A. S. Losko, and S. C. Vogel, "Non-destructive study of bulk crystallinity and elemental composition of natural gold single crystal samples by energy-resolved neutron imaging," *Sci. Rep.*, vol. 7, no. 1, Jan. 2017, Art. no. 40759.

[197] A. S. Tremsin et al., "Non-contact measurement of partial gas pressure and distribution of elemental composition using energy-resolved neutron imaging," *AIP Adv.*, vol. 7, no. 1, Jan. 2017, Art. no. 015315.

[198] A. S. Losko and S. C. Vogel, "3D isotope density measurements by energy-resolved neutron imaging," *Sci. Rep.*, vol. 12, no. 1, p. 6648, Apr. 2022.

[199] C. Zhang et al., "Analysis of chemical stress and the propensity for cracking during the vertical Bridgman growth of BaBrCl:Eu," *J. Cryst. Growth*, vol. 546, Sep. 2020, Art. no. 125794.

[200] J. J. Derby et al., "Computational modeling and neutron imaging to understand interface shape and solute segregation during the vertical gradient freeze growth of BaBrCl:Eu," *J. Cryst. Growth*, vol. 536, Apr. 2020, Art. no. 125572.

[201] *Significant Achievements in Space Science 1965*, document NASA Report SP-136, 1967.

[202] W. B. Atwood et al., "The large area telescope on the fermi gamma-ray space telescope mission," *Astrophys. J.*, vol. 697, no. 2, pp. 1071–1102, Jun. 2009.

[203] M. L. McConnell, P. F. Bloser, J. Legere, and J. M. Ryan, "Applications for new scintillator technologies in gamma ray astronomy, *J. Phys., Conf. Ser.*, vol. 763, Oct. 2016, Art. no. 012008.

[204] T. H. Prettyman et al., "Dawn's Gamma ray and neutron detector," *Space Sci. Rev.*, vol. 163, nos. 1–4, pp. 371–459, Dec. 2011.

[205] R. Hart and M. R. Campbell, "Digital radiography in space," *Aviation Space Environ. Med.*, vol. 73, no. 6, pp. 601–606, Jul. 2002.

[206] A. Owens, "Scintillators on interplanetary space missions," *IEEE Trans. Nucl. Sci.*, vol. 55, no. 3, pp. 1430–1436, Jun. 2008.

[207] L. J. Mitchell, R. Perea, B. F. Phlips, R. S. Woolf, A. L. Hutcheson, and M. V. Johnson-Rambert, "Proton-induced activation of new scintillator materials: SrI, GAGG, CLLB, CLLBC, TLYC, CLYC-7," *IEEE Trans. Nucl. Sci.*, vol. 69, no. 6, pp. 1322–1330, Jun. 2022.

[208] F. G. A. Quarati, I. V. Khodyuk, C. W. E. van Eijk, P. Quarati, and P. Dorenbos, "Study of 138La radioactive decays using $LaBr_3$ scintillators," *Nucl. Instrum. Methods Phys. Res. A, Accel. Spectrom. Detect. Assoc. Equip.*, vol. 683, pp. 46–52, Aug. 2012.

[209] M. Yoneyama et al., "Evaluation of GAGG:Ce scintillators for future space applications," *J. Instrum.*, vol. 13, no. 2, Feb. 2018, Art. no. P02023.

[210] M. Ghelman, N. Kopeika, S. Rotman, T. Edvabsky, E. Vax, and A. Osovizky, "Design of 4p high-efficiency directional radiation detector based on Compton scattering," *IEEE Trans. Nucl. Sci.*, vol. 69, no. 4, pp. 832–839, Apr. 2022.

[211] Note: Rb has two natural isotopes, ^{85}Rb (72.2%) and ^{87}Rb (27.8%). ^{87}Rb can β^- decay to ^{87}Sr with a half life of 4.97×10^{10} years. The weak radioactivity of ^{87}Rb is sufficient to fog photographic films (no longer commonly used due to electronic digital technologies) in 30–60 days.

[212] J. Peng et al., "Crystallization of $CsPbBr_3$ single crystals in water for X-ray detection," *Nature Commun.*, vol. 12, no. 1, Mar. 2021.

[213] Z. Wang et al., "Cerium doping double perovskite scintillator for sensitive X-ray detection and imaging," *Chem. A Eur. J.*, vol. 27, no. 35, pp. 9071–9076, Jun. 2021.

[214] B. Li, Y. Xu, X. Zhang, K. Han, J. Jin, and Z. Xia, "Zero-dimensional luminescent metal halide hybrids enabling bulk transparent medium as large-area X-ray scintillators," *Adv. Opt. Mater.*, vol. 10, no. 10, May 2022, Art. no. 2102793.

[215] F. Zhou, Z. Li, W. Lan, Q. Wang, L. Ding, and Z. Jin, "Halide perovskite, a potential scintillator for X-ray detection," *Small Methods*, vol. 4, no. 10, Oct. 2020, Art. no. 2000506.

[216] N. Zaitseva et al., "Scintillation properties of solution-grown trans-stilbene single crystals," *Nucl. Instrum. Methods Phys. Res. A, Accel. Spectrom. Detect. Assoc. Equip.*, vol. 789, pp. 8–15, Jul. 2015.

[217] M. I. Pinilla-Orjuela, K. E. Mesick, P. F. Bloser, and J. R. Tutt, "Performance evaluation of pulse shape discrimination capable organic scintillators for space applications," 2021, *arXiv:2111.08845*.

[218] A. J. Tucker, "Computerized ionospheric tomography," *Johns Hopkins APL Tech. Dig.*, vol. 19, no. 1, pp. 66–71, 1998.

[219] *Multimodal RadIT Has Significant Potential for Greater Than Sum of Parts Imaging, With Neutron X-Ray Imaging Improving Separation of Some Materials When Mixing Modalities. Versatile Scintillators That Allow for Multi Species Imaging is of Great Value in This Regard, as Reusing the Detection Setup for Different Modalities Reduces the Overhead on Combining the Modalities (Credit, an Anonymous Reviewer)*, 2023.

[220] D. P. Cormode et al., "Multicolor spectral photon-counting computed tomography: In vivo dual contrast imaging with a high count rate scanner," *Sci. Rep.*, vol. 7, no. 1, pp. 1–11, Jul. 2017, Art. no. 4784.

[221] *Accelerator-Based Pulsed Neutron Generation, and More Recently Laser-Driven Fusion Ignition Plasmas, With Fast Scintillators Sensitive to Neutrons and X-Rays, Allow Single-Axis Bimodal Imaging Via Time-of-Flight Separation of Neutrons and the X-Rays Produced by Bremsstrahlung and Nuclear Reaction Products (Credit, an Anonymous Reviewer)*, 2023.

[222] C. H. McCollough, S. Leng, L. Yu, and J. G. Fletcher, "Dual- and multi-energy CT: Principles, technical approaches, and clinical applications," *Radiology*, vol. 276, no. 3, pp. 637–653, Sep. 2015.

[223] T. R. C. Johnson, "Dual-energy CT: General principles," *Amer. J. Roentgenol.*, vol. 199, no. 5, pp. S3–S8, Nov. 2012.

[224] S. Faby et al., "Performance of today's dual energy CT and future multi energy CT in virtual non-contrast imaging and in iodine quantification: A simulation study," *Med. Phys.*, vol. 42, no. 7, pp. 4349–4366, Jul. 2015.

[225] H. Kiji et al., "Spectral photon-counting CT system based on Si-PM coupled with novel ceramic scintillators," in *Radiation Detection Systems*, J. S. Iwanczyk and K. Iniewski, Eds. Boca Raton, FL, USA: CRC Press, 2022, pp. 91–109.

[226] J. S. Iwanczyk et al., "Photon counting energy dispersive detector arrays for X-ray imaging," *IEEE Trans. Nucl. Sci.*, vol. 56, no. 3, pp. 535–542, Jun. 2009.

[227] S. Kappler et al., "Quantum-counting CT in the regime of count-rate analysis: Introduction of the pile-up trigger method," *Proc. SPIE*, vol. 7961, Mar. 2011, Art. no. 79610T.

[228] S. Yoon, "Fast neutron-gamma discrimination in organic scintillators via convolution neural network," *J. Korean Phys. Soc.*, vol. 80, no. 5, pp. 427–433, 2022.

[229] E. Doucet, "Machine learning n/γ discrimination in CLYC scintillators," *Nucl. Instrum. Methods Phys. Res. A, Accel. Spectrom. Detect. Assoc. Equip.*, vol. 954, Feb. 2020, Art. no. 161201.

[230] M. G. Poirot et al., "Physics-informed deep learning for dual-energy computed tomography image processing," *Sci. Rep.*, vol. 9, no. 1, Nov. 2019, Art. no. 17709.

[231] C. Hu et al., "BaF2:Y and ZnO:Ga crystal scintillators for GHz hard X-ray imaging," *Nucl. Instrum. Methods Phys. Res. A, Accel. Spectrom. Detect. Assoc. Equip.*, vol. 950, Jan. 2020, Art. no. 162767, doi: 10.1016/j.nima.2019.162767.

[232] V. Vaněček, K. Děcká, E. Mihóková, V. Čuba, R. Král, and M. Nikl, "Advanced halide scintillators: From the bulk to nano," *Adv. Photon. Res.*, vol. 3, no. 8, Apr. 2022, Art. no. 2200011, doi: 10.1002/adpr.202200011.

[233] S. Gundacker et al., "Experimental time resolution limits of modern SiPMs and TOF-PET detectors exploring different scintillators and Cherenkov emission," *Phys. Med. Biol.*, vol. 65, no. 2, Jan. 2020, Art. no. 025001, doi: 10.1088/1361-6560/ab63b4.

[234] A. Ohnishi, M. Saito, M. Kitaura, M. Itoh, and M. Sasaki, "Auger-free luminescence due to interatomic p–d transition and self-trapped exciton luminescence in Rb_2ZnCl_4 crystals," *J. Lumin.*, vol. 132, no. 10, pp. 2639–2642, Oct. 2012, doi: 10.1016/j.jlumin.2012.05.009.

[235] M. Kitaura, S. Watanabe, K. Ogasarawa, A. Ohnishi, and M. Sasaki, "Comparative study of Auger-free luminescence of RB_2ZnCl_4 crystals between experiment and calculation," *Phys. Status Solidi C*, vol. 10, nos. 7 and 8, pp. 993–996, May 2013, doi: 10.1002/pssc.201200825.

[236] K. Takahashi, M. Arai, M. Koshimizu, Y. Fujimoto, T. Yanagida, and K. Asai, "Luminescence characteristics of Cs_2BaCl_4," *Jpn. J. Appl. Phys.*, vol. 59, no. 3, Feb. 2020, Art. no. 032003, doi: 10.35848/1347-4065/ab762b.

[237] K. Takahashi, M. Arai, M. Koshimizu, Y. Fujimoto, T. Yanagida, and K. Asai, "Luminescence and scintillation properties of Cs_2ZnCl_4 and Cs_3ZnCl_5," *Jpn. J. Appl. Phys.*, vol. 59, no. 7, Jun. 2020, Art. no. 072002, doi: 10.35848/1347-4065/ab9655.

[238] J. Saaring et al., "Time-resolved luminescence spectroscopy of ultrafast emissions in $BaGeF_6$," *J. Lumin.*, vol. 244, Apr. 2022, Art. no. 118729, doi: https://doi.org/10.1016/j.jlumin.2022.118729.

[239] V. Vaněček et al., "(INVITED) Ultraviolet cross-luminescence in ternary chlorides of alkali and alkaline-earth metals," *Opt. Mater., X*, vol. 12, Dec. 2021, Art. no. 100103, doi: 10.1016/j.omx.2021.100103.

[240] K. Yamanoi et al., "Perovskite fluoride crystals as light emitting materials in vacuum ultraviolet region," *Opt. Mater.*, vol. 36, no. 4, pp. 769–772, Feb. 2014, doi: 10.1016/j.optmat.2013.11.023.

[241] D. Rutstrom et al., "Improved light yield and growth of large-volume ultrafast single crystal scintillators Cs_2ZnCl_4 and Cs_3ZnCl_5," *Opt. Mater.*, vol. 133, Nov. 2022, Art. no. 112912, doi: 10.1016/j.optmat.2022.112912.

[242] H. J. Seifert and G. Thiel, "Thermal analysis for generating phase diagrams of systems alkali metal chloride/divalent metal chloride," *Thermochimica Acta*, vol. 100, no. 1, pp. 81–107, May 1986, doi: 10.1016/0040-6031(86)87052-6.

[243] A. Ohnishi, M. Kitaura, T. Otomo, and M. Sasaki, "Reflection spectrum and auger-free luminescence in molecular ionic crystals of Cs_2ZnCl_4," *J. Phys. Soc. Jpn.*, vol. 72, no. 9, pp. 2400–2401, Sep. 2003, doi: 10.1143/JPSJ.72.2400.

[244] N. Yahaba et al., "X-ray detection capability of a Cs_2ZnCl_4 single-crystal scintillator," *Appl. Phys. Exp.*, vol. 7, no. 6, May 2014, Art. no. 062602, doi: 10.7567/apex.7.062602.

[245] A. Ohnishi, M. Kitaura, M. Itoh, and M. Sasaki, "Electronic structure and auger-free luminescence in Cs_2ZnCl_4 crystals," *J. Phys. Soc. Jpn.*, vol. 81, no. 11, Nov. 2012, Art. no. 114704, doi: 10.1143/JPSJ.81.114704.

[246] B. Wang, M. Zhu, X. Jia, Y. Zhang, J. Li, and J. Wang, "Bridgman growth and intrinsic luminescence of pure Cs_2ZnCl_4 single crystal," *J. Electron. Mater.*, vol. 51, no. 11, pp. 6512–6517, Sep. 2022, doi: 10.1007/s11664-022-09890-3.

[247] E. A. McKigney et al., "Nanocomposite scintillators for radiation detection and nuclear spectroscopy," *Nucl. Instrum. Methods Phys. Res. A, Accel. Spectrom. Detect. Assoc. Equip.*, vol. 579, no. 1, pp. 15–18, Aug. 2007.

[248] K. J. Wilson, R. Alabd, M. Abolhasan, M. Safavi-Naeini, and D. R. Franklin, "Optimisation of monolithic nanocomposite and transparent ceramic scintillation detectors for positron emission tomography," *Sci. Rep.*, vol. 10, no. 1, pp. 1–15, Jan. 2020.

[249] S. Y. Chou, P. R. Krauss, and P. J. Renstrom, "Nanoimprint lithography," *J. Vac. Sci. Technol. B, Microelectron.*, vol. 14, no. 6, pp. 4129–4133, 1996, doi: 10.1116/1.588605.

[250] C. Cerna et al., "Nanoscale structurized plastic scintillators," presented at the 16th Int. Conf. Scintillating Mater. Their Appl. (SCINT), Santa Fe, NM, USA, Sep. 2022.

[251] A. Koch, C. Raven, P. Spanne, and A. Snigirev, "X-ray imaging with submicrometer resolution employing transparent luminescent screens," *J. Opt. Soc. Amer. A, Opt. Image Sci.*, vol. 15, no. 7, pp. 1940–1951, 1998.

[252] A. Takeuchi, K. Uesugi, H. Takano, and Y. Suzuki, "Submicrometer-resolution three-dimensional imaging with hard X-ray imaging microtomography," *Rev. Sci. Instrum.*, vol. 73, no. 12, pp. 4246–4249, Dec. 2002.

[253] Y. Zorenko, "Single crystalline film characteristics based on the orthosilicate, perovskite and garnet compounds," *IEEE Trans. Nucl. Sci.*, vol. 59, no. 5, pp. 2260–2268, Oct. 2012.

[254] F. Riva, T. Martin, P. A. Douissard, and C. Dujardin, "Single crystal lutetium oxide thin film scintillators for X-ray imaging," *J. Instrum.*, vol. 11, no. 10, Oct. 2016, Art. no. C10010.

[255] P.-A. Douissard, "A novel epitaxially grown LSO-based thin-film scintillator for micro-imaging using hard synchrotron radiation," *J. Synchrtron Rad.*, vol. 17, pp. 571–583, Jul. 2010.

[256] F. Riva, "Epitaxial growth of gadolinium and lutetium-based aluminum pervoskite thin films for X-ray micro-imaging applications," *CystEngComm*, vol. 18, pp. 608–615, Jan. 2016.

[257] L. Wollensen et al., "Scintillating thin film design for ultimate high resolution X-ray imaging," *J. Mater. Chem. C*, vol. 10, pp. 9257–9265, May 2022.

[258] A. Favalli, H.-C. Mehner, J.-M. Crochemore, and B. Pedersen, "Pulsed neutron facility for research in illicit trafficking and nuclear safeguards," *IEEE Trans. Nucl. Sci.*, vol. 56, no. 3, pp. 1292–1296, Jun. 2009.

[259] P. Baeten, M. Bruggeman, and R. Carchon, "An investigation of the neutron die-away time in passive neutron waste assay systems," BLG, Belgium, pp. 1–27, Feb. 1997.

[260] F. Ferrulli, M. Labalme, and M. Silari, "Investigation of CLYC-6 for thermal neutron detection and CLYC-7 for fast neutron spectrometry," *Nucl. Instrum. Methods Phys. Res. A, Accel. Spectrom. Detect. Assoc. Equip.*, vol. 1029, Apr. 2022, Art. no. 166460.

[261] *GS20 Glass Datasheet, Scintacor*. [Accessed: Dec. 4, 2022. Online]. Available: https://scintacor.com/products/6-lithium-glass/

[262] G. F. Knoll, *Radiation Detection and Measurement*. Ann Arbor, MI, USA: Wiley, 2010.

[263] J. Chadwick, "Possible existence of a neutron," *Nature*, vol. 129, p. 312, Feb. 1932.

[264] Z. Wang and C. L. Morris, "Tracking fast neutrons," *Nucl. Instrum. Methods Phys. Res. A, Accel. Spectrom. Detect. Assoc. Equip.*, vol. 726, pp. 145–154, Oct. 2013.

[265] M. Mayer, J. Nattress, C. Trivelpiece, and I. Jovanovic, "Geometric optimization of a neutron detector based on a lithium glass-polymer composite," *Nucl. Instrum. Methods Phys. Res. A, Accel. Spectrom. Detect. Assoc. Equip.*, vol. 784, pp. 168–171, Jun. 2015.

[266] B. W. Wiggins, A. Favalli, M. L. Iliev, K. D. Ianakiev, and M. P. Hehlen, "Computational investigation of arranged scintillating particle composites for fast neutron detection," *Nucl. Instrum. Methods Phys. Res. A, Accel. Spectrom. Detect. Assoc. Equip.*, vol. 915, pp. 17–23, Jan. 2019.

[267] K. Kazkaz, N. S. Bowden, and M. Pedretti, "Comparison of lithium gadolinium borate crystal grains in scintillating and nonscintillating plastic matrices," *IEEE Trans. Nucl. Sci.*, vol. 60, no. 2, pp. 1416–1426, Apr. 2013.

[268] M. Mayer et al., "Development and characterization of a neutron detector based on a lithium glass-polymer composite," *Nucl. Instrum. Methods Phys. Res. A, Accel. Spectrom. Detect. Assoc. Equip.*, vol. 785, pp. 117–122, Jun. 2015.

[269] G. C. Rich, K. Kazkaz, H. P. Martinez, and T. Gushue, "Fabrication and characterization of a lithium glass-based composite neutron detector," *Nucl. Instrum. Methods Phys. Res. A, Accel. Spectrom. Detect. Assoc. Equip.*, vol. 794, pp. 15–24, Sep. 2015.

[270] K. D. Ianakiev et al., "Neutron detector based on particles of 6Li glass scintillator dispersed in organic light guide matrix," *Nucl. Instrum. Methods Phys. Res. A, Accel. Spectrom. Detect. Assoc. Equip.*, vol. 784, pp. 189–193, Jun. 2015.

[271] M. P. Hehlen, B. W. Wiggins, A. Favalli, M. Iliev, and K. D. Ianakiev, "Light propagation in a neutron detector based on 6Li glass scintillator particles in an organic matrix," *J. Appl. Phys.*, vol. 124, no. 12, Sep. 2018, Art. no. 124502.

[272] C. Richards, B. Wiggins, M. Iliev, A. Favalli, and T. McLean, "Performance assessment of a compact neutron detector module based on scintillating composites," *Proc. SPIE*, vol. 12241, Oct. 2022, Art. no. 122410.

[273] B. W. Wiggins, C. G. Richards, R. O. Nelson, M. Iliev, and M. P. Hehlen, "Investigations of radiation damaged arranged scintillating particle composites," *J. Appl. Phys.*, vol. 130, no. 19, Nov. 2021, Art. no. 193102.

[274] R. Ramprasad, R. Batra, G. Pilania, A. Mannodi-Kanakkithodi, and C. Kim, "Machine learning in materials informatics: Recent applications and prospects," *NPJ Comput. Mater.*, vol. 3, no. 1, pp. 1–13, Dec. 2017.

[275] D. Morgan and R. Jacobs, "Opportunities and challenges for machine learning in materials science," *Annu. Rev. Mater. Res.*, vol. 50, no. 1, pp. 71–103, Jul. 2020.

[276] G. Pilania, "Machine learning in materials science: From explainable predictions to autonomous design," *Comput. Mater. Sci.*, vol. 193, Jun. 2021, Art. no. 110360.

[277] D. Morgan, "Machine learning in nuclear materials research," *Curr. Opin. Solid State Mater. Sci.*, vol. 26, Apr. 2022, Art. no. 100975.

[278] A. Agrawal and A. Choudhary, "Deep materials informatics: Applications of deep learning in materials science," *MRS Commun.*, vol. 9, no. 3, pp. 779–792, Sep. 2019.

[279] Y. Zhuo, A. Mansouri Tehrani, A. O. Oliynyk, A. C. Duke, and J. Brgoch, "Identifying an efficient, thermally robust inorganic phosphor host via machine learning," *Nature Commun.*, vol. 9, no. 1, p. 4377, Oct. 2018.

[280] Y. Zhuo, S. Hariyani, S. You, P. Dorenbos, and J. Brgoch, "Machine learning 5D-level centroid shift of Ce^{3+} inorganic phosphors," *J. Appl. Phys.*, vol. 128, no. 1, Jul. 2020, Art. no. 013104.

[281] Y. Zhuo, S. Hariyani, E. Armijo, Z. Abolade Lawson, and J. Brgoch, "Evaluating thermal quenching temperature in Eu^{3+}-substituted oxide phosphors via machine learning," *ACS Appl. Mater. Interface*, vol. 12, no. 5, pp. 5244–5250, Feb. 2020.

[282] G. Pilania, X.-Y. Liu, and Z. Wang, "Data-enabled structure–property mappings for lanthanide-activated inorganic scintillators," *J. Mater. Sci.*, vol. 54, no. 11, pp. 8361–8380, Jun. 2019.

[283] C. Park, "A data-driven approach to predicting band gap, excitation, and emission energies for Eu^{2+}-activated phosphors," *Inorg. Chem. Frontiers*, vol. 8, no. 21, pp. 4610–4624, 2021.

[284] G. Pilania, K. J. McClellan, C. R. Stanek, and B. P. Uberuaga, "Physics-informed machine learning for inorganic scintillator discovery," *J. Chem. Phys.*, vol. 148, no. 24, Jun. 2018, Art. no. 241729.

[285] P. Dorenbos, "Ce^{3+} 5D-centroid shift and vacuum referred 4f-electron binding energies of all lanthanide impurities in 150 different compounds," *J. Lumin.*, vol. 135, pp. 93–104, Mar. 2013.

[286] P. Dorenbos, "The 5D level positions of the trivalent lanthanides in inorganic compounds," *J. Lumin.*, vol. 91, pp. 155–176, Nov. 2000.

[287] P. Dorenbos, "Modeling the chemical shift of lanthanide 4f electron binding energies," *Phys. Rev. B, Condens. Matter*, vol. 85, no. 16, Apr. 2012, Art. no. 165107.

[288] W. B. Powell and I. O. Ryzhov, *Optimal Learning*. Hoboken, NJ, USA: Wiley, 2012.

[289] T. Lookman et al., *Information Science for Materials Discovery and Design*. Cham, Switzerland: Springer, 2016, pp. 3–12.

[290] J. Friedman, T. Hastie, and R. Tibshirani, *The Elements of Statistical Learning* (Springer Series in Statistics). Berlin, Germany: Springer, 2001.